



OTTO VON GUERICKE  
UNIVERSITÄT  
MAGDEBURG

FAKULTÄT FÜR  
ELEKTROTECHNIK UND  
INFORMATIONSTECHNIK

# Investigation of artifacts and mechanical properties of non-metallic MRI biopsy needles in interventional procedures: Phantom and Simulation studies

## Dissertation

zur Erlangung des akademischen Grades

## Doktoringenieurin (Dr.-Ing.)

von Marwah AL-Maatoq, M.Sc.

geb. am 14.07.1985 in Baghdad, Iraq

genehmigt durch die Fakultät für Elektrotechnik und Informationstechnik  
der Otto-von-Guericke-Universität Magdeburg

Gutachter: Prof. Dr. Christoph Hoeschen (Otto-von-Guericke-Universität Magdeburg)  
Prof. Dr. Michael Friebe (AGH University of Science and Technology)  
Prof. Dr. Heike Walles (Otto-von-Guericke-Universität Magdeburg)

Promotionskolloquium am 18.12.2023

## Abstract

Magnetic resonance imaging (MRI) is a medical imaging modality for detecting diseases and pathological changes in tissue. It is also a promising method for guiding invasive interventional devices such as endovascular catheters, guide wires, biopsy needles, and stent applications. However, recent advances in clinical research indicate that the visualization of MRI-compatible devices under magnetic fields is challenging because of susceptibility artifacts generated in the MR image during scanning as signal voids or distortions in the MRI images. These artifacts arise due to variations in the magnetic susceptibility of different tissues or materials within the body. Despite recent advances in clinical research, devices made from Nickel-Titanium alloys continue to produce significant susceptibility artifacts during imaging due to their interactions with the magnetic field. Therefore, there is an ongoing need to develop and optimize interventional devices showing fewer artifacts and thus resulting in improved visualization capabilities and better image quality. The quality of MRI images relies on the proper selection of materials for interventional devices in order to minimize artifacts and allow for precise positioning of the target during surgery, particularly in the case of biopsy needles. Therefore the main hypothesis of this thesis is that the use of non-metallic materials in the design of biopsy needles can reduce these artifacts. Thus, in this work, I propose a coaxial needle design from a multi-layer concept using a new combination of non-metallic materials to optimize their visualization in MRI. The design has a fiber-enforced inner core and an outer hollow sheet. For the proposed biopsy needles, the artifacts were evaluated and quantified in an MRI scanner using two types of custom-made phantoms, gelatin, and a tissue-engineered version. Then the artifacts were quantitatively evaluated using two approaches, a manual, and a machine learning-based workflow. The proposed design biopsy needle has allowed reducing the amount of artifacts in the MRI scan compared to the conventional biopsy needle. Subsequently, examine the mechanical characterization of the biopsy needles by experimental and simulation analysis to enhance their performance. The obtained results show that a new combination of non-metallic materials used to fabricate the biopsy needles provides a comparable outer sheet dimension in an MR image compared to a standard needle. Meanwhile, the mechanical findings were optimized and met the standard dimensions with the required performance. Conclusively, the proposed methodology based on non-metallic materials has shown to be a promising approach for biopsy needle design.

## Zusammenfassung

Magnetresonanztomographie (MRT) ist ein medizinisches Bildgebungsverfahren zur Diagnose von Krankheiten und Veränderungen im Gewebe. Sie stellt eine vielversprechende Methode zur Führung minimalinvasiver interventioneller Geräte wie endovaskuläre Katheter, Führungsdrähte, Biopsienadeln und Stents dar. Allerdings deuten jüngste Fortschritte in der klinischen Forschung darauf hin, dass die Visualisierung von MRT-kompatiblen Geräten unter Magnetfeldern herausfordernd ist, aufgrund von Suszeptibilitätsartefakten, die im MRT-Bild während Aufnahme als Signalverluste oder Verzerrungen auftreten. Diese Artefakte entstehen aufgrund von Variationen in der magnetischen Empfindlichkeit verschiedener Gewebe oder Materialien im Körper. Trotz neuer Entwicklungen in der klinischen Forschung erzeugen Geräte aus Nickel-Titan-Legierungen während der Bildgebung weiterhin signifikante Suszeptibilitätsartefakte aufgrund ihrer Wechselwirkungen mit Magnetfeld. Daher besteht weiterhin Bedarf an der Entwicklung und Optimierung interventioneller Geräte, die weniger Artefakte aufweisen und somit zu verbesserten Visualisierung und einer besseren Bildqualität führen. Die Qualität von MRT-Bildern hängt dabei von der richtigen Materialauswahl für interventionelle Geräte ab, um Artefakte zu minimieren und präzise Positionierung des Ziels während Operation zu ermöglichen, insbesondere im Fall von Biopsienadeln. Daher lautet die Hauptthese dieser Promotionsarbeit, dass der Einsatz von nichtmetallischen Materialien im Design von Biopsienadeln diese Artefakte reduzieren kann. In dieser Arbeit schlage ich daher ein koaxiales Nadel-Design aus einem Mehrschichtkonzept vor, bei dem neue Kombination von nichtmetallischen Materialien verwendet werden, um deren Visualisierung im MRT zu optimieren. Das Design besteht aus einem faserunterstützten Innenkern und einer äußeren Hohlplatte. Mit den angefertigten nicht-metallischen Biopsienadeln wurden im Anschluss die Suszeptibilitätsartefakte im MRT-Scanner mit zwei maßangefertigten Phantomen, einem Gelatine-Modell und einem zellulären Brustkrebsmodell, bewertet und quantifiziert. Dann wurden Artefakte quantitativ mit zwei Ansätzen bewertet, einem manuellen Quantifizierungsschritt und einem auf maschinellem Lernen basierenden Workflow. Das vorgeschlagene nicht-metallische Design der Biopsienadel hat dazu beigetragen, die Menge der Artefakte in MRT-Aufnahme im Vergleich zur konventionellen Biopsienadel deutlich zu reduzieren. Anschließend wurde eine mechanische Charakterisierung der Biopsienadeln durch experimentelle und simulationsbasierte Analysen zur Verbesserung ihrer Leistung durchgeführt. Die erzielten Ergebnisse zeigen, dass neuartige Kombination von nicht-metallischen Materialien bei der Herstellung von Biopsienadeln, zu vergleichbaren Größen der äußeren Hohlplatte im MRT-Bild im Vergleich zur Standardnadel führen. Zusammenfassend hat das vorgeschlagene Design basierend auf nichtmetallischen Materialien sich als vielversprechender Ansatz für die Optimierung von Biopsienadeln erwiesen.

## **Declaration by the candidate**

I hereby declare that this thesis is my own work and effort and that it has not been submitted anywhere for any award. Where other sources of information have been used, they have been marked.

The work has not been presented in the same or a similar form to any other testing authority and has not been made public.

I hereby also entitle a right of use (free of charge, not limited locally and for an indefinite period of time) that my thesis can be duplicated, saved and archived by the Otto von Guericke University of Magdeburg (OvGU) or any commissioned third party (e. g. *iParadigms Europe Limited*, provider of the plagiarism-detection service “Turnitin”) exclusively in order to check it for plagiarism and to optimize the appraisal of results.

Marwah Al-Maatoq  
Magdeburg, January 10, 2024

# Contents

<b>1</b>	<b>Introduction</b>	<b>12</b>
1.1	Motivation . . . . .	14
1.2	Research questions, hypothesis, and goals . . . . .	15
1.3	Proposal and workflow . . . . .	16
1.4	Summary of thesis objectives . . . . .	17
1.5	Contribution . . . . .	17
1.6	List of publications . . . . .	18
<b>2</b>	<b>Theoretical framework and state of the art</b>	<b>22</b>
2.1	Fundamental principles in imaging of biopsy needles . . . . .	22
2.1.1	Magnetic resonance imaging . . . . .	22
2.1.1.1	MRI signals and radio-frequency coils . . . . .	24
2.1.1.2	Static magnetic field . . . . .	25
2.1.1.3	Slice selection and spatial encoding . . . . .	27
2.1.1.4	Spin echo sequence . . . . .	28
2.1.1.5	Gradient echo sequence . . . . .	29
2.1.1.6	Larmor equation . . . . .	30
2.1.1.7	MRI test parameters . . . . .	31
2.1.2	Magnetic susceptibility artifacts in biopsy needles . . . . .	32
2.2	Current challenges in MR-guided biopsy interventions . . . . .	34
2.2.1	Criteria for selecting compatible materials for biopsy needles . . . . .	43
2.2.2	Computational methods for artifacts detection . . . . .	44
2.2.3	Mechanical characterization used in interventions MRI biopsy needle	45
2.2.3.1	Stress-strain analysis . . . . .	45
2.2.3.2	Finite element analysis (FEA) . . . . .	47
<b>3</b>	<b>Materials and Methods</b>	<b>49</b>
3.1	Materials selection protocol . . . . .	49
3.2	Fabrication strategy for the proposed non-metallic biopsy needles . . . . .	50
3.2.1	Multi-layer concept for polymeric biopsy needles . . . . .	50
3.2.2	Flexible polymeric biopsy needle . . . . .	50
3.2.3	Inner core: structuring . . . . .	51
3.2.4	Outer hollow sheet . . . . .	52
3.2.5	Biopsy needle tips . . . . .	53

3.3	Preparation of phantoms . . . . .	54
3.3.1	Gelatin phantom . . . . .	54
3.3.2	Tissue-engineered phantom . . . . .	55
3.4	Image acquisition from gelatin and tissue-engineered phantoms . . . . .	56
3.4.1	MRI scanner . . . . .	56
3.4.2	MRI scan parameters . . . . .	57
3.5	Approaches for evaluating the susceptibility artifacts for MRI . . . . .	62
3.5.1	Manual quantification . . . . .	62
3.5.2	Machine learning K-means quantification . . . . .	63
3.6	Mechanical testing for non-metallic biopsy needles . . . . .	63
3.6.1	Experimental setup: Zwick Roell machine . . . . .	64
3.6.2	Modeling setup: Finite element analysis modeling . . . . .	65
3.6.3	Uncertainty analysis in FEA: Critical analysis . . . . .	79
<b>4</b>	<b>Results and discussion</b>	<b>81</b>
4.1	Qualitative analysis for MRI artifacts . . . . .	81
4.1.1	Analysis of image artifacts based on MRI scans performed on a gelatin phantom . . . . .	81
4.1.1.1	MRI results for the core needles . . . . .	81
4.1.1.2	MRI results for the biopsy needles . . . . .	83
4.1.1.3	MRI results of rotated biopsy needles in a gelatin phantom . . . . .	83
4.1.2	Analysis of image artifacts based on MRI scans of needles in tissue- engineered phantom . . . . .	84
4.2	Quantitative analysis for MRI artifacts . . . . .	87
4.2.1	Assessing artifacts from core biopsy needles . . . . .	88
4.2.2	Assessing artifacts from the biopsy needles . . . . .	89
4.2.3	Assessing artifacts of rotated biopsy needles in gelatin phantom . . . . .	90
4.2.4	Assessing artifacts of biopsy needles in a tissue-engineered phantom . . . . .	92
4.2.5	Assessing artifacts of biopsy needles using machine learning . . . . .	93
4.2.5.1	Artifacts quantification: Needles width . . . . .	94
4.2.5.2	Artifacts quantification: Needles length . . . . .	95
4.2.5.3	Cluster validation: Silhouette score . . . . .	97
4.3	Assessing mechanical properties of non-metallic biopsy needles . . . . .	98
4.3.1	Results from the experimental setup using Zwick Roell machine . . . . .	99
4.3.2	Results from the modeling using FEA . . . . .	100
4.3.3	Uncertainty analysis in FEA: Critical analysis . . . . .	109
<b>5</b>	<b>Conclusions and future work</b>	<b>112</b>
5.1	Conclusions . . . . .	112
5.2	Future work . . . . .	114

<b>Bibliography</b>	<b>117</b>
<b>A Appendix</b>	<b>134</b>
A.1 Testing the flexibility of polymeric needles in angular setup . . . . .	134
A.2 MRI scanning of 2 biopsy needles in 4 rotation angle . . . . .	134
A.3 Measuring the dimensions for the experimental setup of the Zwick Roell machine . . . . .	135
<b>B Simulation FEA</b>	<b>136</b>
B.1 Design II: materials assignment for PBNs . . . . .	136
B.2 Setting the analysis parameters for Design I and Design II . . . . .	137
B.3 Static structural analysis in FEA for Design II . . . . .	138
B.4 Bending status in FEA for the non-metallic and standard needles . . . . .	139
B.5 Applying the meshing step for the Design II . . . . .	140
B.6 Stress and safety factor for standard and best-proposed biopsy needle with 2 mm . . . . .	141
B.7 Simulation test results in Design II for the stress and safety factor for the needles at 2 mm pusher displacement for maximum mechanical properties .	142

## List of Acronyms

ASTM	American Society for Testing and Materials
AWG	American wire gauge
BN	Biopsy needle
CT	Computed Tomography
CAD	Computer aided design
CoCr	Cobalt Chrome alloy
cor	Coronal
DBS	density-based clustering algorithm
2D	Two-dimensional
3D	Three-dimensional
FEA/FEM	Finite element analysis/Finite element method
FG	Fiber glass
FB	Fiber bundle
FEP	Fluorinated ethylene propylene
FoS	Factor of safety
FLASH	Fast Low-Angle Shot
G	Gauge
GR	Glass rod
GPa	Giga Pascal
g/cc	Gram per cubic centimeter
GE	Gradient echo
HASTE	Half-Fourier single-shot turbo spin-echo



HDA	Hierarchical Divisive algorithm
ISO	International Organization for Standardization
LW	Light wall
MRI	Magnetic Resonance Imaging
MPa	Mega Pascal
N	Newton
NiTi	Nitinol alloy
OD	Outer diameter
PTFE	Polytetrafluoroethylene
PEEK	Polyther ether ketone
PBN	Proposed biopsy needle
PI	Polyimide
P.D	Pusher displacement
PIC	Proposed inner core
RFA	Radiofrequency ablation
RF	Radiofrequency
sag	Sagittal
SBN	Standard biopsy needle
SIC	Standard inner core
SS	Structural steel
SE	Spin echo
TW	Thin wall
tra	Transverse
TE	Echo time
TR	Repetition time

T1-weighted Relaxation time

T2-weighted Relaxation time

US            Ultrasound

Vs            Versus

ZrO<sub>2</sub>        Ceramic zirconia

## List of Figures

1.1	Schematic diagram for the proposed work . . . . .	20
1.2	Uncertainty analysis employed to the proposed work . . . . .	21
2.1	MRI magnet coils used during MRI scan . . . . .	23
2.2	The magnetic field direction . . . . .	24
2.3	MRI planes . . . . .	25
2.4	The behavior of protons in the MRI environment . . . . .	26
2.5	Slice selection and spatial encoding . . . . .	27
2.6	Slice selection and spatial encoding . . . . .	30
2.7	Comparison of susceptibility needle artifacts . . . . .	36
2.8	Preliminary test for artifacts reduction in RFA needle . . . . .	37
2.9	Examples of MRI needles artifacts during insertion . . . . .	38
2.10	Preliminary test for measuring width artifacts in SOMATEX needles . . . . .	38
2.11	This study presents an example of a needle artifact in an MR image that results in positional errors (taken from [66]). . . . .	39
2.12	Examples of artifacts from titanium and ceramic needles . . . . .	40
2.13	Different angulation against the main magnetic field . . . . .	41
2.14	Some of commercial MRI needles . . . . .	42
2.15	Current clinical problem for the conventional needles . . . . .	43
2.16	Stress strain curve . . . . .	46
2.17	Bending test curve . . . . .	47
3.1	First prototype for proposed biopsy needle . . . . .	51
3.2	The proposed multi-layer concept for the core needle . . . . .	52
3.3	Seven proposed biopsy needles . . . . .	53
3.4	Microscopic images for the needle tips . . . . .	54
3.5	Workflow explaining the steps used for the fabrication of the 3D tissue-engineered phantom and MRI scan . . . . .	55
3.6	Schematic illustration for preparation of the tissue-engineered 3D tumor model (taken from [154]). . . . .	56
3.7	Photograph of the 3T MRI Siemens (Skyra), in Research Campus STIMULATE, Otto-von-Guericke-Universität Magdeburg (OVGU), Germany. . . . .	57
3.8	Three core needles in MRI gelatin phantom . . . . .	58
3.9	Seven proposed non-metallic needles in gelatin phantom . . . . .	59

3.10 Seven non-metallic PBNs with NiTi needle inside the MRI scanner. . . . .	59
3.11 3D tissue-engineered phantom with PBNs and SBN inside the MRI machine.	61
3.12 Schematic diagram presenting the MRI scanning steps for the three biopsy needles (1, NiTi, and 3) . . . . .	61
3.13 A graphical flow chart presenting the two approaches used to quantify the artifacts in the MR images of PBNs. . . . .	62
3.14 Graphical representation of a manual quantification method used to measure biopsy needle shaft and diameter. . . . .	63
3.15 MRI image used to apply K-means algorithm to the biopsy needles . . . . .	64
3.16 Detailed workflow for the proposed unsupervised machine learning concept	64
3.17 Zwick/Roell machine setup . . . . .	65
3.18 Workflow process for the FEA containing pre-processing, solver, and post- processing. . . . .	67
3.19 Workflow for the proposed methodology used in FEA to optimize the biopsy needle design . . . . .	68
3.20 AutoCAD design structure for NiTi and PICs made from FG: (a) complete inner core structure, (b) cross-section for the inner core, and (c) inner core tip. . . . .	70
3.21 A 3D AutoCAD configuration used for 2-point mechanical bending setup parts a) fixation, b) pusher. . . . .	71
3.22 3D modeling design of the mechanical bending setup used in FEA . . . . .	72
3.23 Meshing generation status for the bending setup and core needle. . . . .	74
3.24 Static structural analysis performed using FEA . . . . .	76
3.25 3D AutoCAD models for the proposed and standard biopsy needles design in FEA . . . . .	77
4.1 MRI scan results for the three cores needles 1, NiTi, and 3 inside gelatin phantom presented GE (left image) and SE (right image) sequences. . . . .	82
4.2 MR images for the 8 needles inside the phantom . . . . .	83
4.3 MRI scans of NiTi and needle number 1 in a gelatin phantom were obtained using GE and SE sequences at a) 0°, b) 90°, c) 180°, and d) 270° rotation angles to differentiate artifacts between the two sequences. . . . .	84
4.4 Qualitative comparison results . . . . .	87
4.5 A comparison for individual 2D MRI scan between GE and SE sequence for (1, NiTi, and 3) biopsy needle in tissue-engineered phantom. . . . .	87
4.6 Comparison of MRI scans in 2D and 3D mode using GE sequence . . . . .	88
4.7 Comparison of MRI scans between 2D and 3D mode in cross-section per- spective for the three biopsy needles, 1, NiTi, and 3 in tissue-engineered phantom . . . . .	89

4.8	Artifacts evaluation for the 3 cores . . . . .	90
4.9	Artifacts evaluation for the seven prospered needles with NiTi needle in two MRI sequences . . . . .	91
4.10	Results of artifacts evaluation for the widths and lengths of the three needles (1, NiTi, 3) in the gelatin phantom . . . . .	93
4.11	Artifacts assessment based on the MRI mode for the needles (1, NiTi, and 3) in tissue-engineered phantom . . . . .	94
4.12	Clustered images for the 8 needles from MR images, non-metallic needles labeled as L1, L2, L3, L5, L6, L7, L8 while the NiTi needle labeled as L4 using cluster range from K3 to K7. . . . .	95
4.13	Results of comparison the width of the artifact in (mm) between manual quantification and K-means quantification . . . . .	96
4.14	Results of comparison of the length of the artifact in (mm) between manual quantification and K-means cluster quantification . . . . .	97
4.15	Boxplot showing the Silhouette coefficient according to K-means clusters . . . . .	98
4.16	2-point bending test results from the Zwick Roell machine . . . . .	99
4.17	Simulation plot results for the force reaction vs. pusher displacement in Design I . . . . .	102
4.18	Simulation plot results for force reaction vs. pusher displacement at 2 mm for Design II . . . . .	107
4.19	The best-proposed biopsy needle design in FEA . . . . .	110
A.1	Evaluate the flexibility of multi-layer polymeric biopsy needles and compare them with a standard needle in three angular setups (30°, 60°, 90°). . . . .	134
A.2	MRI scan for rotational biopsy needles setup: a) fix two needles in gelatin phantom, b) apply two angle indicators for each needle, c) NiTi needle and non-metallic needle numbered as 1 inside the MRI scan. . . . .	134
A.3	Experimental setup parts for the 2-point bending test for the Zwick Roell machine. . . . .	135
B.1	Default analysis settings parameters for FEA simulation. . . . .	137
B.2	Static structural analysis in FEA for Design II . . . . .	138
B.3	Mechanical bending setups in FEA for the standard biopsy needle and proposed needles. . . . .	139
B.4	Meshing for the standard biopsy needle and proposed needles. . . . .	140

## List of Tables

2.1	Comprehensive comparison table of commercially available MRI-compatible biopsy needles. It includes information on manufacturing sources, composition, gauge (G) sizes, application areas, and MRI visibility properties. . . .	42
3.1	Raw materials used to fabricate the proposed biopsy needles . . . . .	50
3.2	Specifications of the outer sheets used for biopsy needles . . . . .	53
3.3	MRI imaging protocol . . . . .	57
3.4	Bending test parameters used for the Zwick Roell machine. . . . .	65
3.5	Dimensions used in FEA simulation for the standard inner core and proposed inner cores. . . . .	71
3.6	Mechanical properties of the materials used in the FEA simulation in Design I [162–166,176–181]. . . . .	72
3.7	Number of nodes and elements for NiTi core and PICs used in the ANSYS simulation for the bending setup. . . . .	74
3.8	Number of nodes and elements for SBN and PBNs in mechanical setup. . .	74
3.9	Material mechanical properties used in FEA simulation to perform the Design II . . . . .	78
3.10	Dimensions used in FEA for the Design II stage for the standard biopsy needle (SBN). . . . .	79
3.11	Dimensions of the non-metallic PBNs in FEA. . . . .	80
4.1	Quantifying the width and length of the artifact for the needle (NiTi + 1) at four rotational angles when the MRI sequence is in GE. . . . .	91
4.2	Artifacts quantification for NiTi and 1 including the width and length for each needle in mm when the MRI sequence is SE. . . . .	92
4.3	The stress and safety factor for inner core needles at a minimum range of mechanical properties . . . . .	103
4.4	The stress and safety factor for inner core needles at a maximum range of mechanical properties . . . . .	104
4.5	Breaking point simulation test in Design I for the SIC and PIC at 10 mm pusher displacement, when mechanical properties are at a minimum, rang.	105
4.6	Breaking point simulation test for the SIC and best PIC at 10 mm pusher displacement for maximum values of material properties in Design I. . . . .	106

4.7	Simulation results for the breaking points of standard and proposed biopsy needles at a minimum range of mechanical properties . . . . .	108
4.8	Simulation breaking point test for the needles at 10 mm pusher displacement for maximum mechanical properties in Design II. . . . .	109
4.9	Effect of mesh element size variation on force reaction error at a pusher displacement of 2 mm for SBN and best PBN 1 with minimum Young's modulus, Bulk modulus, and Shear modulus values. . . . .	111
4.10	Effect of mesh element size variation on force reaction error at a pusher displacement of 2 mm for SBN and best PBN 1 with maximum Young's modulus, Bulk modulus, and Shear modulus values. . . . .	111
B.1	Materials assignment in the mechanical setup for proposed biopsy needles .	136
B.2	Stress and safety factor for standard and best-proposed biopsy needle with 2 mm pusher displacement at minimum material properties values in Design II. . . . .	141
B.3	Simulation test results in Design II for the stress and safety factor for the needles at 2 mm pusher displacement for maximum mechanical properties.	142

# 1 Introduction

Magnetic resonance imaging (MRI) is a non-invasive medical imaging modality widely used in medical diagnostics. The use of MRI imaging offers several advantages compared to other image modalities such as computed tomography (CT) and ultrasound (US)-guidance [1,2]. MRI provides high-resolution anatomical images with superior soft-tissue contrast and offers functional information with multi-planar imaging. Due to its high sensitivity and specificity, MRI is particularly useful in detecting malignant tumors, diagnosing cardiac and neurological conditions, and studying brain function. In addition to its diagnostic capabilities, MRI is increasingly used for image-guided minimally invasive interventions, allowing for the precise monitoring and control of percutaneous or vascular procedures and surgeries. One exemplary application of MRI-guided interventions is the use of percutaneous biopsy needles for diagnostics, ablation procedures, and pain therapy. The use of MRI for guiding minimally invasive surgeries presents several advantages, including excellent visualization of anatomical structures, pathological and functional information for tissues, and the absence of harmful and ionizing radiation for the patient or the medical staff [3,4]. These benefits can ultimately lead to improved treatment outcomes [5–7]. MRI is a valuable tool in image-guided biopsies, where it is often combined with needle biopsy procedures to diagnose various medical conditions. By providing high-resolution images of the target tissue, MRI enables physicians to quickly and accurately access abnormal areas that may not be visible through the skin during the procedure. Moreover, the use of MRI guidance allows for real-time visualization of the needle placement, enhancing accuracy and reducing the risk of complications. Furthermore, MRI-guided biopsies offer the advantage of providing feedback on the visualization of the used interventional needles, allowing for improved accuracy and efficacy. In some cases, such as spinal access, MRI is the preferred guidance modality due to its ability to provide clear and detailed images of the target area [8]. Moreover, tracking and localization strategies for interventional procedures in near-real-time have been enabled by open or closed-bore configuration MR systems [9–12]. The current commercial availability of open MR systems has become the preferred type for MRI-guided procedures because it provides direct access to the patient. However, MRI is a challenging environment for performing surgeries due to the magnetic fields. The requirements for surgical instruments used in the MR scanner include several safety aspects. The surgical instruments used in MRI-guided interventions have to be MRI-compatible in order not to cause any mechanical forces resulting from the magnetic attraction. Hence, most of the standard surgical instruments cannot be used in the MRI



environment. In addition to these safety aspects, the interventional instruments need to be accurately localized within the MR image. Depending on the instrument's material composition and the presence of magnetic materials, severe artifacts can occur because of a distortion of the MRI's magnetic fields.

Needles have broad applications in minimally invasive procedures, such as injection, regional anesthesia, pain management, brachytherapy, blood sampling, and biopsy sampling [13,14]. The biopsy is a widely adopted method for acquiring tissue samples and involves the use of minimally invasive biopsy needles, wherein a hollow needle is inserted into a targeted area of the body to extract a sample [15]. Subsequently, the acquired tissue sample is sent to a laboratory for detailed analysis, which enables medical professionals to differentiate between cancerous and non-cancerous cells. Typically, a biopsy needle comprises an inner core and two concentric hollow sheets, an inner and an outer one [16,17]. Each biopsy needle was designed according to the needle gauge system, often called Gauge (G), which is an internationally-used scale for sizing needles [18]. They are in the range from 7-34 Gauge [19] each Gauge has its dimension and is used for a specific application. For example, gauges 14,16,18, and 20 are used for soft tissue biopsy. While spinal applications gauges of 21 and 22 are used [3,17,20,21]. As a basic requirement, needles that are used in MRI must be non-magnetic to avoid magnetic attraction [21]. Additionally, the visibility in the MR image is of high importance.

However, it is equally important to ensure the visibility of the needle in the MR image. To address this issue, research efforts have been dedicated to developing strategies for enhancing the visualization of MR-guided needles relative to surrounding tissues [22–24]. These strategies aim to improve the safety and success rates of the procedure by providing clear and precise guidance for needle placement while minimizing the risk of damage to surrounding tissues.

Accurate visualization of needles in the MRI environment is crucial and is directly related to the principal phenomenon known as susceptibility artifacts. These artifacts are caused by the field inhomogeneities induced by the presence of the needle, resulting in distortion or signal loss in the MR image [5]. Therefore, it is essential to minimize these artifacts through the use of specialized materials that reduce magnetic field distortions and improve the visualization of the needle during MRI-guided procedures. Continued research and development in this area will lead to improved accuracy and safety in MRI-guided interventions. These susceptibility artifacts effects depend on many factors mainly on materials used for the biopsy. A thorough understanding of the factors that impact the appearance of needles in MR images is essential to accurately evaluate the positioning accuracy achievable under MRI guidance. In order to gain insight into these factors, numerous research groups have conducted experimental studies on the appearance of needles in MR images. These studies aim to develop a comprehensive understanding of the interactions between the needle and the MR environment and to identify strategies for

improving the accuracy and safety of MRI-guided procedures. By applying these findings, clinicians and researchers can work towards optimizing the performance of MRI-guided interventions [25–28]. When developing an interventional biopsy needle that can be safely and accurately used in the MRI environment, the main concern is achieving good visibility in the MR image with minimal artifacts. Specifically, the size of the biopsy visible in the MR image should be as close as possible to the actual size of the needle. Additionally, it is important to ensure that the mechanical performance of the MRI-compatible needle is preserved compared to standard needles. Achieving both good visibility in the MR image and maintaining the mechanical performance of the needle is critical for successful MRI-guided biopsies. For example, current interventional needles made from stainless steel provide the required mechanical properties, but they are known to produce large artifacts in MR images because of their material composition [29]. On the other hand, ceramic needles produce less or no artifacts [30, 31]. However, needles made from ceramics potentially risk brittle, limiting their usage in medical applications. Therefore, based on that further research is needed to improve the design and manufacture of MRI-compatible interventional needles that meet the criteria, in order to optimize the accuracy and safety of MRI-guided biopsies.

## 1.1 Motivation

Despite the remarkable advances in MRI technology, the development of MRI-compatible biopsy needles for interventional procedures remains a crucial need in modern medicine. The precise guidance of medical interventions towards specific targets using real-time MRI imaging guidance requires the use of materials that are compatible with the MRI environment. The current challenges in material compatibility pose a significant obstacle to the use of MRI in interventional settings, as compatible materials can cause susceptibility artifacts that can severely degrade the quality of MR images. It is imperative to address these issues to enable effective MRI-guided interventions. The susceptibility artifacts can lead to visualization issues, such as large artifacts that can obscure anatomical structures or small artifacts that may go unnoticed on MR images, thereby affecting the performance of guiding modalities in various minimally invasive intervention applications such as liver, spinal, brain, breast biopsies, and others. Therefore, it is essential to develop appropriate MRI-compatible materials that can enable precise and accurate visualization and guidance of medical interventions.

Hence, a high-quality interventional biopsy needle designed for usage in the MRI environment requires good visibility in the MR image but should only produce minimal artifacts. Specifically, the needle size that is visible in MR images should be consistent with its actual size to ensure accurate guidance, while minimizing any artifacts that could adversely affect the quality of the MR image. At the same time, maintain their mechanical performance

characteristics, including physical properties and functionality such as stiffness, strength, and tissue penetration capabilities. Specifically, it is crucial that these properties are preserved and comparable to those of standard needles, even when using MRI-compatible materials and following clinical guidelines for MRI interventional procedures.

The core idea of this work is to present the current state of the art in MRI interventional biopsy needles and what is still missing for medical needs to achieve. This shall be achieved by selecting suitable MRI-compatible materials with an appropriate proposed new methodology for fabricating following clinical guidelines for MRI interventional procedures.

## 1.2 Research questions, hypothesis, and goals

On the one hand, based on the motivation leads us to consider whether the potential of the newly proposed concept will provide the solution for susceptibility artifacts in the MR images. Furthermore, adhering to the specific technical requirements of MRI imaging makes the proposed biopsy design particularly relevant and beneficial for clinical practitioners, as it may help to improve the accuracy and efficacy of MRI-guided biopsies. On the other hand, although many approaches in this regard have been proposed, the results are insufficient to be applied in clinical practices so far [25, 29]. The observed behavior can be attributed to the limited accuracy and sensitivity of current methods used to assess needle artifacts in the MR images generated by the current approaches, as will be discussed in detail in Chapter 2. Analysis of the published literature related to needle artifacts reveals that despite significant research efforts, accurate and reliable identification of these artifacts remains a challenging issue in MRI-guided biopsy procedures.

Consequently, it raises the question of whether the research in biopsy needles based on MRI guidance modality, as performed nowadays, considers all the standard requirements for the MRI environment. Previous clinical research has explored and investigated the use of different approaches for reduced needle susceptibility artifacts caused by needles in MR images. For example, recent advanced studies [32–35]. However, despite these efforts, there is still a lack of consensus and standardization regarding the most effective strategies for reducing biopsy needle artifacts in MRI imaging. Putting all together, the main research questions that naturally arise are the following:

1. Could the proposed non-metallic biopsy needle materials be able to reduce the artifacts during MRI interventions?
2. Could the proposed design concept for the non-metallic biopsy needle fulfill the functionality criteria?
3. Could machine learning be a suitable approach for detecting needle artifacts?

4. Are the artifacts for the non-metallic biopsy needles different when a tissue-engineered phantom is applied during an MRI scan?
5. How does the use of Finite Element Analysis (FEA) enable the optimization of mechanical performance and facilitate the adjustment of final needle design specifications?

From the research questions raised above, I derive the main research hypothesis: Application of non-metallic materials can reduce the artifacts from biopsy needles during MRI interventions

### 1.3 Proposal and workflow

The core idea of this thesis is to develop and implement new methodologies and techniques to investigate the artifact and mechanical properties of non-metallic biopsy needles used in minimally invasive MRI-guided surgery. The proposed research aims to compare the performance of biopsy needles composed of new materials with conventional materials used in MRI interventions. The proposal considers experimenting with both new and already proposed compatible materials in the literature. It is well known that the physical or mechanical properties of the needle depend on both the material and the applied fabrication technique [36]. Therefore, the working methodology involves the fabrication of seven prototypes using configurations with multiple materials, using a fabrication technique called the multi-layer concept. The developed and built prototypes will be tested and evaluated concerning the following design criteria:

- Visibility of proposed biopsy needles in MR images using two different sequences T1-weighted and T2-weighted.
- Detection approach for needle artifacts utilizing manual and machine learning approaches.
- Examining mechanical properties using experimental setup and simulation such as stiffness, bending strength, and breaking point.
- Analyzing the behavior of the proposed non-metallic needles when it impeded in tissue-engineered phantom.

The final goal is to obtain an optimal non-metallic biopsy needle based on the required mechanical properties depending on its spinal cord applications and the absence of MR image artifacts disturbing the interventional procedure. This shall be achieved by selecting appropriate MRI-compatible materials combined with an innovative proposed design. Accordingly, the experimental workflow for this work is schematically illustrated in Fig. 1.1.

Furthermore, the proposed work underwent uncertainty quantification at each stage, as indicated by the test type employed and illustrated in Fig. 1.2.

A glass or metal tip is incorporated at the distal end, with a thin outer plastic sheet covering the entire needle. To evaluate the proposed needle design, I built and investigate seven needle prototypes and then compared them with a standard MRI interventional needle used as a reference. "The mechanical characteristics of all the needles were assessed in two stages using the Zwick Roell machine after undergoing MRI scanning. The obtained data was then used to optimize their performance through FEA techniques.

## 1.4 Summary of thesis objectives

This work introduces the design of non-metallic that incorporates a multi-layer concept. The needles are fabricated using a cost-effective, MR-compatible material. The needles are designed with a thin wall structure to minimize artifacts and enhance stability performance during MR-guided interventions. The main objectives of this study are to develop and evaluate the performance of these needles in the context of MR interventions, with a particular focus on reducing artifacts and improving stability. The general objectives of this work can be summarized as follows:

- Develop and optimize the visualization of interventional biopsy needles for use in MRI-guided procedures.

The specific objectives are defined as follows:

- Define the requirements for the MRI interventional clinical procedure according to the medical needs.
- Apply a new combination of MRI-compatible biomaterials for the proposed biopsy needles to mitigate MR image artifacts, considering the required mechanical properties for the biopsy design.
- Enhance the mechanical performance through experimental and simulation setups.
- Implement a machine learning approach for needle artifacts in MRI.

## 1.5 Contribution

This study was designed to systematically investigate artifacts caused by interventional needles recommended for use in MRI, with a focus on MRI sequences, needle design materials, and mechanical properties [37]. In this work, I propose a design for an MRI-compatible needle that utilizes a multi-layer concept. The proposed needle design incorporates a fiber bundle-enforced core as the inner layer, which is then surrounded by plastic tubes forming

the outer layer. A glass or metal tip is incorporated at the distal end, with a thin outer plastic sheet covering the entire needle. To evaluate the proposed needle design, I built and investigate seven needle prototypes and then compared them with a standard MRI interventional needle used as a reference. "The mechanical characteristics of all the needles were assessed in two stages using the Zwick Roell machine after undergoing MRI scanning. The obtained data was then used to optimize their performance through FEA techniques.

## 1.6 List of publications

Part of the content presented in this thesis work has already been published in peer-reviewed scientific journals and presented at international conferences. The list of publications is provided below:

### Journal publications

- **AL-Maatoq, M.**, Fuentealba, P., Fachet, M., Glüge, R., Ali, S. H., & Hoeschen, C. Carbon Nanotube-Based Reinforced Polymers for Medical Applications: Improving Impact Strength of Polymer-Polymer Composites. *Journal of Nanomaterials*, 2022.
- **AL-Maatoq, M.**, Fachet, M., Walles, H., & Hoeschen, C. Susceptibility artifacts evaluation for non-metallic biopsy needles in a biological-engineered 3D tumor model. *Current Directions in Biomedical Engineering*, 8(2), 289-292, 2022.
- **AL-Maatoq, M.**, Fachet, M., Rao, R., & Hoeschen, C. Artifacts' Detection for MRI Non-Metallic Needles: Comparative Analysis for Artifact Evaluation Using K-Means and Manual Quantification. *Magnetochemistry*, 9(3), 79, 2023.
- Kumar, K., Fachet, M., **AL-Maatoq, M.**, Chakraborty, A., Khismatrao, R., Oka, Sh., Stauffer, Th., Grüner, F., Michel, Th., Walles, H., & Hoeschen, C. Characterization of a polychromatic microfocus X-ray fluorescence imaging setup with metallic contrast agents in a microphysiological tumor model. *Frontiers in Physics*, 11, 263, 2023.

### Conference publications

- **AL-Maatoq, M.**, Krug, J. W., & Friebe, M. H. The tip is the key-rfa needle modification using peek for reduced susceptibility artifact in mri, 27th Annual SMIT Conference, 2015.
- **AL-Maatoq, M.**, Boese A. & Friebe, M. Concept of a multilayer biopsy needle for magnetic resonance imaging interventions. BMT Conference: 51st annual conference of the German Society for Biomedical EngineeringAt: DresdenVolume: 2017.

- **AL-Maatoq, M.**, Chen, C., Boese A.& Friebe, M. Flexible Polymeric Puncture Needle for a Nonlinear Intervention Path. CARS Conference: Computer Assisted Radiology and Surgery, 2018.
- **AL-Maatoq, M.**, Boese, A., Henke, H. W.,& Friebe, M. Primary design concept for non-metallic MRI compatible needle for Spinal applications pain therapy needles. Conference: 41st Annual International Conference of the IEEE Engineering in Medicine & Biology Society (EMBC), July 23-27, 2019.
- **AL-Maatoq, M.**, Doshi A., Boese, A., Kalmar M.,& Friebe M., Revolving biopsy gun for soft tissues single access the multi-sample collection. BMT Conference: 53rd Annual Conference of the German Society for Biomedical Engineering (DGBMT within VDE), 2019.
- **AL-Maatoq, M.**, Doshi, A., Kalmar, M., Boese, A., & Friebe, M. Innovative revolving biopsy device design supported by additive manufacturing. Transactions on Additive Manufacturing Meets Medicine, 1(1) 2019.
- **AL-Maatoq, M.**, Boese, A.,& Friebe, M. Artefact-reduced MRI imaging by using fibre-bundle core-based needles. IEEE Engineering in Medicine & Biology International Student Conference (EMBS ISC). In BOOK OF PROCEEDINGS (p.35), 2019.

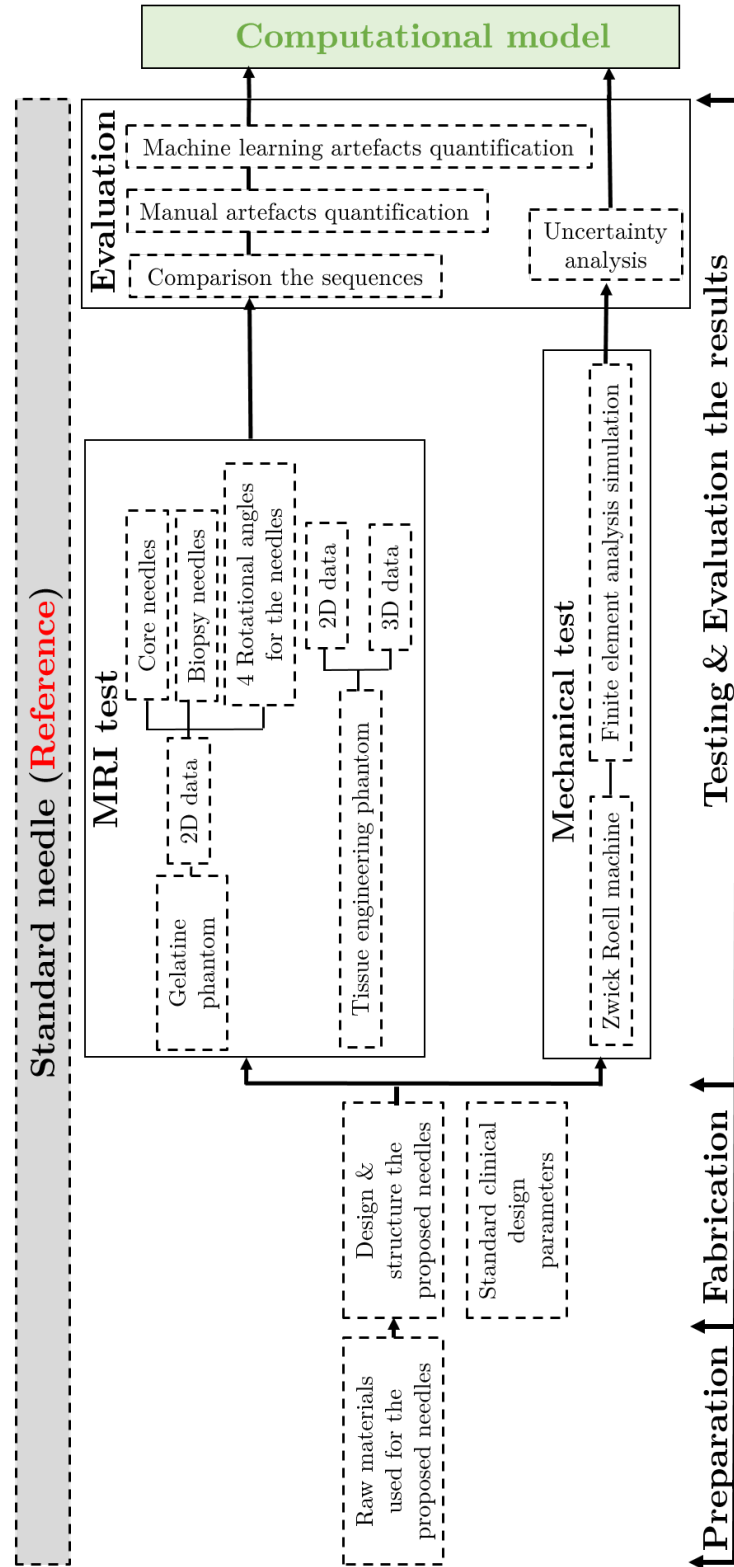


Figure 1.1: A schematic illustration of the fabrication process used for the development of the proposed non-metallic biopsy needles. The process involves selecting the raw materials, followed by several stages of manufacturing, then evaluating the performance by applying several tests. The performance assessment involves a comparison between the proposed biopsy needles and a standard needle, allowing for the identification of any deviations or improvements in the proposed design.



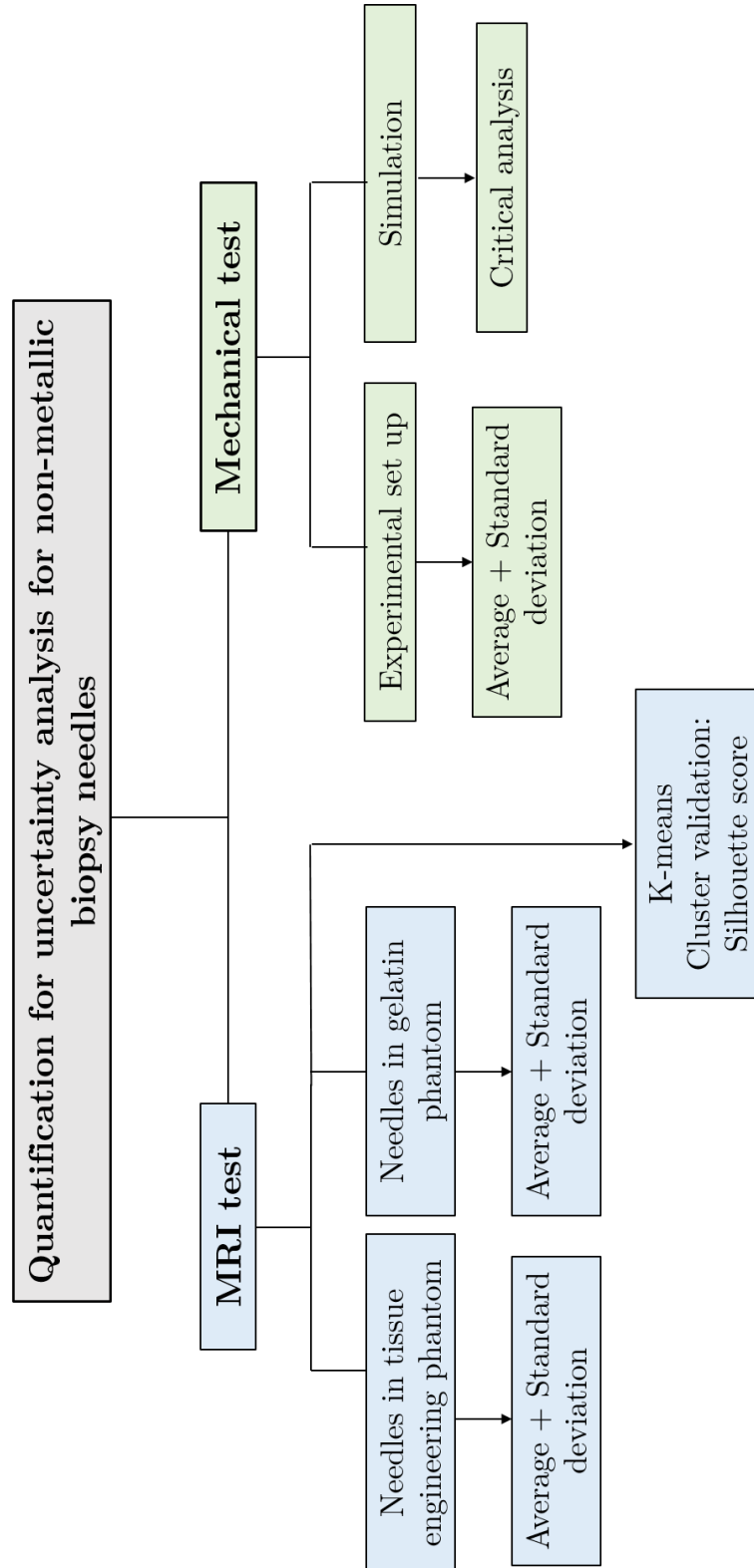


Figure 1.2: Diagram demonstrates the different methods used to quantify uncertainty in the MRI and mechanical tests. For the MRI test, uncertainty was assessed using both the average and standard deviation in one part and the K-means clustering algorithm with silhouette scores in another part. In the mechanical tests, uncertainty was assessed through the average and standard deviation of the experimental setup, and through critical analysis of the simulation results.

## **2 Theoretical framework and state of the art**

This chapter provides an overview of the current challenges in MRI-guided interventions, with a particular focus on biopsy needles. Biopsy procedures require precise and accurate guidance, making them an ideal application for MRI. However, current biopsy needles face several challenges, such as limited visibility, lack of maneuverability, and potential needle damage. To address these challenges, recent prototypes for biopsy needle products have been developed using materials and designs for MRI-guided interventions. In this work, I discuss recent developments and identify the gaps and limitations in the existing literature. In addition, the chapter explains the theoretical framework to characterize the biopsy needle performance from an imaging and functionality perspective. The imaging perspective shows how the image is formed in an MRI scan and describes its parameters, including the susceptibility artifacts generated in the MRI image. Furthermore, the characterization for the functionality perspective was clarified based on experimental and simulation techniques.

### **2.1 Fundamental principles in imaging of biopsy needles**

The following chapter provides a comprehensive review of the principles for the MRI and its working environment, including the guiding aspects for the biopsy needles and explaining the concept of the susceptibility artifacts generated from biopsy needles and their applications. In addition, a detailed description of the characterization technique used for biopsy needles in the MRI field.

#### **2.1.1 Magnetic resonance imaging**

The MRI system consists of two primary components: the control center and the machine housing. The control center, located where the operator operates, houses the "host" computer equipped with a graphical user interface. The connected electronics and power amplifiers are typically positioned in an adjacent area and connected to the second group of equipment. The machine housing, where the patient is situated, contains the components responsible for generating and receiving the MR signal. These components include the primary magnet coils, three gradient coils, shim coils, and an integrated radio-frequency (RF) transmitter coil, as depicted in Fig. 2.1. To ensure the utilization of RF electromagnetic waves in MRI, the room must be shielded from potential sources of electromagnetic noise. To achieve this, the magnet and its associated coils are enclosed

within a dedicated copper-lined testing room, forming a Faraday shield [38, 39]. This shielding principle is fundamental to MRI systems. The fundamental operating principle of MRI machines involves generating a strong magnetic field that aligns the spins of hydrogen atoms in the body. This process will be elaborated upon in the following section.

According to Maxwell's equations, the flow of electric current through a wire generates a magnetic field [40]. However, this current flow encounters resistance, which hinders its flow and generates heat. To minimize resistance and heat production, superconducting magnets are used in the main magnetic coils. These magnets utilize a special type of metal conductor that is cooled to extremely low temperatures. Superconducting magnets allow for high-strength magnetic fields to be generated using high electric currents without excessive heat generation. In clinical MR systems, superconducting magnets are utilized in the main magnetic coils, typically made of a superconducting metal alloy cooled to a temperature close to absolute zero (-269 degrees Celsius or 4 Kelvin) using cryogenic liquid helium, which is a costly process [41]. The main magnet coils produce a strong and constant magnetic field known as  $B_0$  to which the patient is exposed. The strength of this magnetic field is measured in Tesla units (T). Presently, most clinical MR systems are superconducting and operate at field strengths of 1.5 T, 3 T, and 7 T. Additionally, researchers at the University of Minnesota are preparing to conduct initial tests on human subjects using MRI machines with a magnetic field strength of 11.7 T. [42, 43].

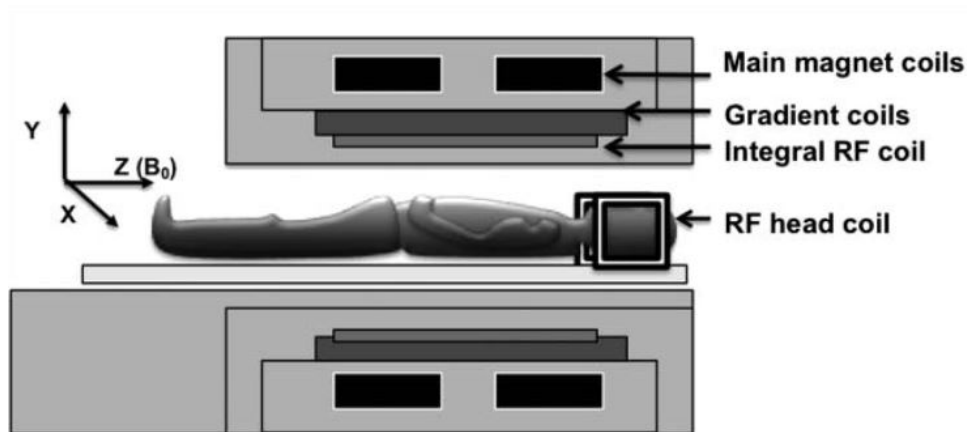


Figure 2.1: The schematic diagram illustrates the positioning of the various MRI magnet coils used during an MRI scan. The patient is positioned on the table within the machine's bore and encircled by a series of coils. An additional radiofrequency (RF) head coil is positioned around the patient's head to optimize the signal-to-noise ratio (SNR), (taken from [38, 44]).

A set of coordinates is used to define the direction of the magnetic field. Gradient coils representing the three orthogonal directions (x, y, and z) are arranged concentrically within the main magnet, as shown in Fig. 2.1. These gradient coils are not supercooled and operate at temperatures close to room temperature. Each gradient coil can generate a

magnetic field in the same direction as the main magnetic field  $B_0$ , but with a strength that varies with location and the direction of the gradient coil. The magnetic field produced by the gradient coils is superimposed on top of the main magnetic field  $B_0$ , causing the main magnetic field strength to vary along the path of the applied gradient field, as depicted in Fig. 2.2.

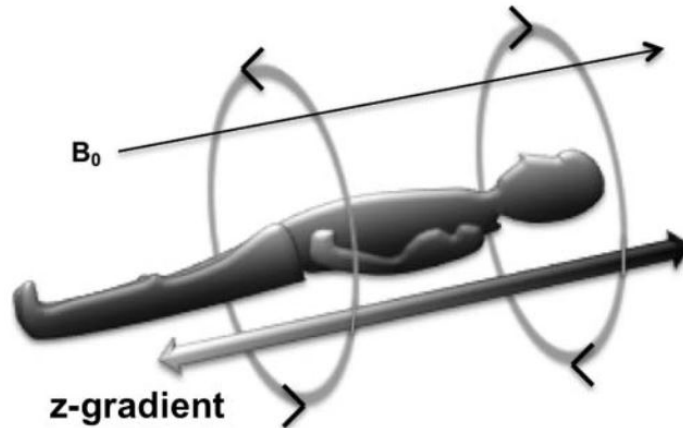


Figure 2.2: Image illustrates the direction of a gradient  $B_0$  in the Z direction. Using Maxwell pair of coils in which the current flowing through them runs in opposite directions to each other (Maxwell pair type) (field captured from [45]).

During an MRI scan, the anatomical structures of interest are imaged in three dimensions. The planes of imaging used in an MRI scan are the sagittal plane when the image is taken from the side, the coronal plane when the image is taken from the front, and the transverse plane when the image is taken from the top down, as demonstrated in Fig. 2.3 [46]. The sagittal, coronal, and transverse planes obtained from MRI provide an accurate three-dimensional representation of anatomical structures, allowing for the visualization and assessment of various medical conditions such as tumors, injuries, and abnormalities. This information is crucial in assisting clinicians with the diagnosis, planning, and monitoring of treatments, and evaluating the effectiveness of interventions. MRI planes can also be used for guiding surgical procedures, as they provide precise information about the location and orientation of structures in the body.

#### 2.1.1.1 MRI signals and radio-frequency coils

The MR signal used to generate the majority of clinical images is sourced from hydrogen nuclei, which are composed of a single proton carrying a positive electrical charge from the human body as presented in Fig. 2.4(a). The MRI scanner utilizes the principles of nuclear magnetic resonance to interact with the protons in the human body and produce a measurable signal as shown in Fig. 2.4(b). Under the influence of the strong magnetic field  $B_0$  in the scanner's bore, the protons undergo random adjustments and become aligned

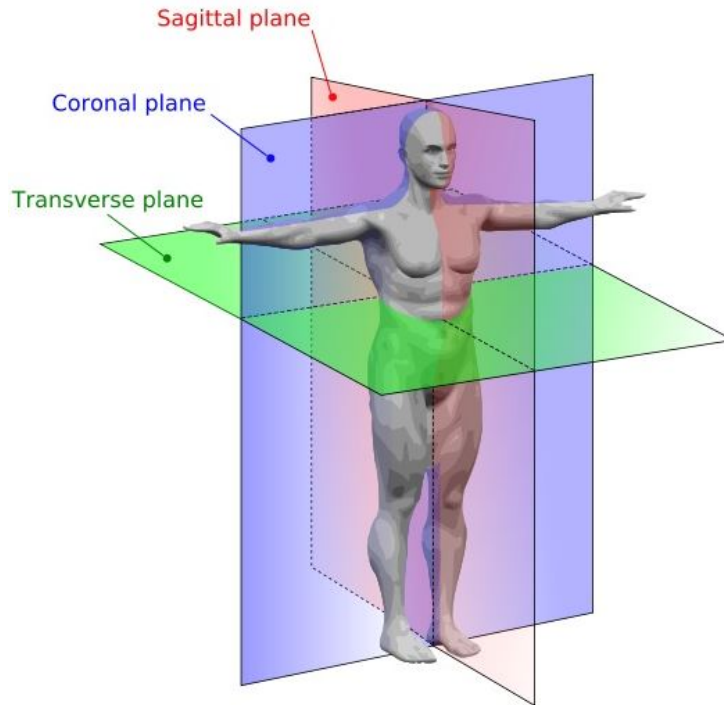


Figure 2.3: The three basic anatomical planes: transverse, coronal, and sagittal (taken from [47]).

along the direction of the magnetic field. A rapidly repeating sequence of RF pulses produced by the scanner causes excitation and resonance of protons [48]. When the RF pulse is turned off, the protons return to their original alignment with the magnetic field, producing a radio-frequency signal that can be detected and converted into an image [49]. RF coils are essential hardware components of magnetic resonance imaging (MRI) systems. They play a critical role in determining the spatial and temporal resolution, sensitivity, and uniformity of MRI images. RF coils serve as the "antennas" of the MRI system, with two primary functions. First, they transmit RF power to stimulate the magnetization of the tissue being imaged. Second, they receive the signal generated by the excited spins in the tissue. Some RF coils perform both transmission and reception of RF energy, while others are designed for either transmission or reception only [50, 51].

### 2.1.1.2 Static magnetic field

The observation of magnetic resonance solely occurs when a robust magnetic field is present. The intensity of the static magnetic field, denoted as  $B_0$  is quantified in Tesla (T) units. The static magnetic field used in MRI is a uniform magnetic field. In MRI, the expression "magnetic field" is used for the main static magnetic field. Because the working volume of this homogeneous static magnetic field is air, the relative permeability  $\mu_r$  is considered to be 1. According to electromagnetic theory [52] the magnetic field strength  $H$  (magnetizing field) in units of A/m is given by the static magnetic field  $B_0$  (saturation):

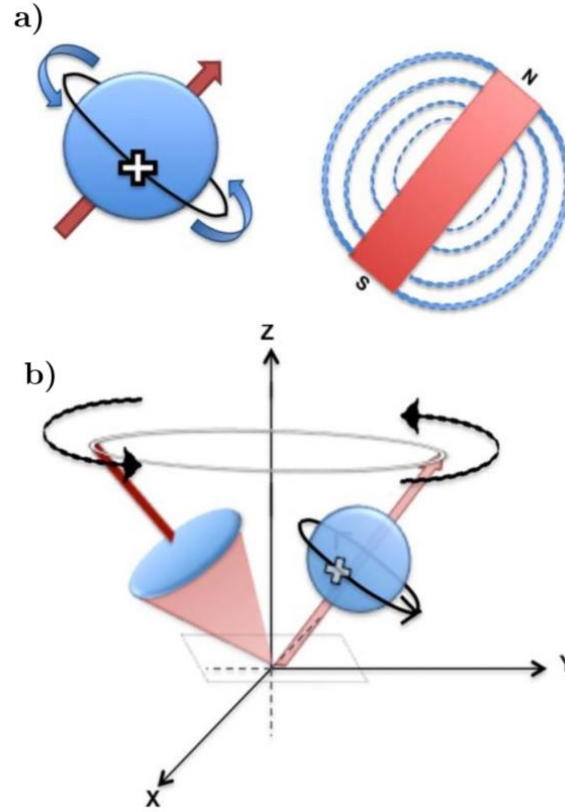


Figure 2.4: The behavior of protons in the MRI environment: a) protons possess a positive charge and are constantly revolving around their own axes. This creates a magnetic field making protons similar to bar magnets, b) the movement of protons likened to the wobbling motion when a spinning top is spun follows a circular path (taken from [38]).

$$\beta_0 = \mu_r \mu_0 H \quad (2.1)$$

The equation (2.1) connects the magnetic field strength  $\beta_0$  with the static magnetic field  $B_0$  using electromagnetic theory. Here,  $H$  represents the magnetic field strength in A/m, while  $\mu_r$  signifies the material's relative permeability, indicating how easily it can be magnetized compared to vacuum permeability  $\mu_0 H$ . In essence, the equation (2.1) illustrates that the magnetic field strength is directly proportional to both the relative permeability of the material and the applied magnetic field strength, providing insights into material responses to magnetic fields. The magnetic field is generated by a large magnet, typically a superconducting magnet that surrounds the patient during the imaging process. According to Maxwell's equations, the flow of an electric current through a wire creates a magnetic field [40]. However, this flow of current is subject to resistance, which can impede the current's flow and generate heat. To reduce resistance and minimize heat production, a special type of metal conductor can be used that is cooled to very low temperatures. This principle is the basis of superconducting magnets, which can generate high-strength

magnetic fields using high electric currents without generating excessive heat. In clinical MR systems, superconducting magnets are used in the main magnetic coils.

### 2.1.1.3 Slice selection and spatial encoding

The process begins by gradually increasing the magnetic field gradient in the slice selection direction, as illustrated in Fig. 2.5. Once the magnetic field gradient stabilizes, an RF pulse is applied, employing a frequency range that aligns with the Larmor frequencies of the targeted region for excitation. The dimensions of a voxel, a single spatial volume, are determined by the user-defined field of view and matrix. The cumulative signals emitted from a voxel determine the brightness of the corresponding pixel on the screen. The sole factor utilized for spatial encoding is the variation in the precessional frequency of the transverse nuclear magnetization, which is contingent upon the magnetic field strength at that specific location. The incoming signal is converted into digital form based on the dimensions of the matrix and the frequency range, and then it is stored in a raw data matrix. Each data point within the raw data matrix is assigned an index called "k," hence why it is also referred to as k-space. To gather sufficient information for image reconstruction, multiple repetitions with distinct phase-encoding gradients are necessary, taking into account the matrix size in the phase encoding direction.

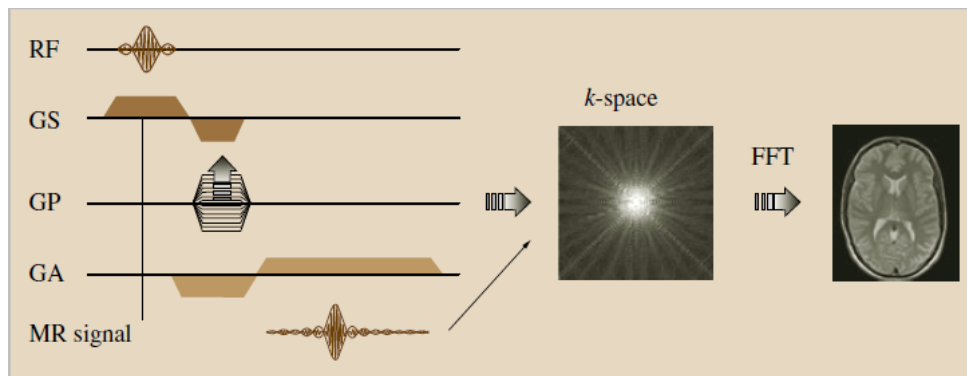


Figure 2.5: The sequence diagram illustrates the following steps: Once the slice selection gradient (GS) reaches its designated value, an RF excitation pulse is administered. Subsequent to the excitation pulse, the transverse nuclear magnetization, which becomes dephased due to discrepancies in resonance frequencies along the slice selection direction during excitation, is rephased. Concurrently, the phase-encoding gradient (GP) can be applied, and preparations can be made for rephasing in the frequency encoding direction (GA). This rephasing is necessary as the transverse nuclear magnetization will experience dephasing caused by differences in resonance frequencies due to the frequency-encoding magnetic field gradient during the readout period. The acquired data are saved in a raw data matrix known as k-space. By subjecting this data to a two-dimensional Fast Fourier Transformation (FFT), the final image can be obtained (taken from [43]).

#### 2.1.1.4 Spin echo sequence

The spin-echo sequence (SE), including the half-Fourier single-shot turbo spin-echo (HASTE) variant, which was discovered unexpectedly while measuring the tissue-specific T1 relaxation time, is highly effective in producing high-quality images with a favorable signal-to-noise ratio. When combined with the spatial encoding scheme of an imaging sequence, it is commonly referred to as the SE sequence. However, its slow imaging speed remains a limitation, as each phase-encoding step requires one repetition time (TR). In a T2-weighted sequence, the typical TR ranges from 2-3 seconds, and at least 256 phase-encoding steps are required for a typical MR image. Consequently, the acquisition of an entire image can take approximately 600 seconds or 10 minutes. The spin echo phenomenon arises after the application of a  $180^\circ$  pulse, which rephases the protons and compensates for fixed magnetic field inhomogeneities. The spin echo phenomenon arises after the application of a  $180^\circ$  pulse, which rephases the protons and compensates for fixed magnetic field inhomogeneities. Here, the half-Fourier single-shot turbo spin-echo (HASTE) sequence plays a significant role. HASTE is designed to rapidly acquire multiple echoes in a single shot, reducing the impact of motion artifacts, which is particularly beneficial in areas like abdominal and pelvic imaging where patient motion can be challenging. It's important to note that this effect does not correct for intrinsic T2 dephasing, which continues uninterrupted. While the protons initially remain in phase at TE (echo time), they subsequently dephase, leading to a decay in the spin echo signal. However, it is possible to restore the signal by applying another  $180^\circ$  pulse to rephase the protons once again. Magnetic susceptibility ( $x$ ) is a critical parameter in the realm of imaging that provides insights into how a material responds to changes in an external magnetic field. This property essentially signifies whether a material's magnetic properties are influenced by the application of an external magnetic field. There are three primary behaviors observed: paramagnetic and ferromagnetic materials respond by increasing their magnetization in the direction of the field, while diamagnetic materials exhibit a decrease in magnetization. In the context of tissue imaging, particularly in MRI, the behavior of protons within a specific tissue is influenced by an effective magnetic field. This effective magnetic field  $\beta_0(ef\!f)$  experienced by the protons is determined by the parameter  $\beta_0(ef\!f)$ , the magnetic susceptibility. The relationship between the effective magnetic field and the external magnetic field  $\beta_0$  can be expressed through the equation:

$$\beta_0(ef\!f) = (1 + x)\beta_0 \tag{2.2}$$

In the equation (2.2),  $x$  represents the magnetic susceptibility of the tissue. If  $x$  is positive, it indicates paramagnetic or ferromagnetic behavior, resulting in an increase in the effective magnetic field. On the other hand, if  $x$  is negative, the material displays diamagnetic behavior, leading to a decrease in the effective magnetic field. This concept is



central to the understanding of how different tissues respond during MRI. By knowing the magnetic susceptibility, one can gain valuable insights into the behavior of protons within tissues and how they interact with the applied magnetic fields. This, in turn, affects the resonance frequencies and ultimately influences the quality and information obtained from MRI images. The equation 2.2 quantitatively captures the relationship between the effective magnetic field experienced by protons and the external magnetic field, giving researchers a tool to understand and manipulate the behavior of tissues in the magnetic resonance imaging process. The spatial distribution of various resonance frequencies remains fixed over time. In the context of MRI, mitigating the dephasing effect is crucial for acquiring accurate information. To achieve this, a technique called the spin echo sequence is employed. This involves the use of radiofrequency (RF) pulses. Specifically, a  $180^\circ$  RF refocusing pulse, also known as an RF refocusing pulse, is utilized in conjunction with a  $90^\circ$  RF excitation pulse. When the  $180^\circ$  RF pulse is applied, it effectively realigns the faster component of the transverse nuclear magnetization, placing it behind the slower component. This realignment generates what is called a spin echo, a phenomenon that is crucial for preserving the coherence of signals. Importantly, this spin echo is produced while a frequency-encoding magnetic field gradient is present, allowing differentiation of spatial locations within the sample. In practical terms, to reconstruct an image, the MRI process requires multiple repetitions with varying phase-encoding steps. The interval between these repetitions is known as the Repetition Time (TR). Additionally, the time duration between the excitation pulse and the acquisition of data is referred to as the Echo Time (TE) as displayed in Fig. 2.6. These parameters play a significant role in the resulting image's contrast, resolution, and sensitivity to specific tissue properties. This interplay of techniques, involving RF pulses and controlled timing, is central to the process of MRI image formation.

#### **2.1.1.5 Gradient echo sequence**

The gradient echo sequence (GE) provides an alternative to SE-based sequences. In contrast to the latter, the GRE sequence does not employ a  $180^\circ$  refocusing pulse and retains  $T2^*$  dephasing. This attribute can be advantageous in scenarios where susceptibility effects are prominent. Additionally, the GR sequence is substantially faster than SE-based sequences, as there is no need to wait for rephasing after the refocusing pulse [53]. Omitting the  $180^\circ$  RF refocusing pulse leads to generating an echo by using bipolar gradient switching in conjunction with frequency encoding as depicted earlier in Fig. 2.5. Different manufacturers employ various acronyms to denote this general approach, such as Fast Low-Angle Shot (FLASH), Fast Field Echo (FFE)-T1, or Spoiled Gradient Recalled Acquired Steady State (SPGR). When the  $180^\circ$  RF refocusing pulse is not employed, the signal decay is no longer solely governed by intramolecular spin-spin interactions represented by the T2 relaxation time. Instead, it becomes influenced by local magnetic field inhomogeneities, which are

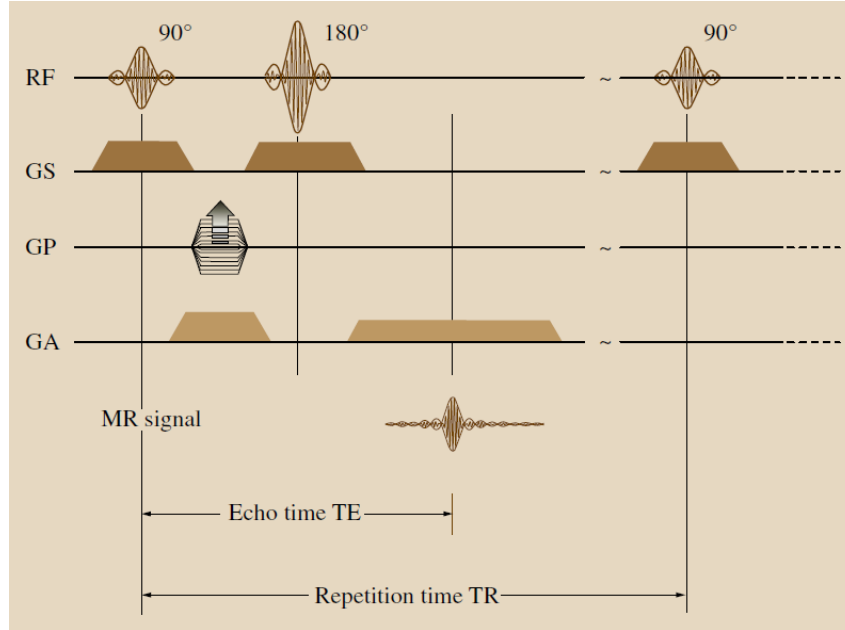


Figure 2.6: Sequence diagram depicting a spin-echo sequence, showcasing the repetition time (TR) and echo time (TE) (taken from [43]).

partially introduced by the patient due to variations in the magnetic susceptibility of adjacent tissues. The accelerated signal decay resulting from these dephasing mechanisms is characterized by the relaxation time  $T^*2$ . The utilization of  $T^*2$  sensitivity plays a crucial role in the detection of hemorrhagic lesions and is extensively employed in susceptibility-weighted imaging (SWI) for optimal results. In GE, it is customary to optimize signal amplification by utilizing a low-angle excitation pulse rather than a  $90^\circ$  excitation pulse [43].

### 2.1.1.6 Larmor equation

When an external static magnetic field is applied to the protons in the human body, it has a collective effect on a group of protons that are individually aligned either parallel or anti-parallel to the direction of the magnetic field, denoted as  $B_0$ . This results in a classical motion of the group of spins, known as precession. The precession of the protons can be likened to the motion of a spinning top. When spun, the top swings do not fall over and the axes of the top circles form a cone shape as presented in Fig. 2.4(b). The speed of precession, that is, how many times the protons process per second, is measured as the precession frequency named the Larmor frequency  $\omega_0$  (MHz) and determined by the Larmor equation:

$$\omega_0 = \gamma B_0 \quad (2.3)$$

$\gamma$  with a constant for a particular nuclear species (e.g., hydrogen) termed the gyro-magnetic ratio with the value of 42.6 MHz/T for the proton. The Larmor equation (2.3) indicates

that precession frequency is proportional to the strength of the magnetic field [38, 54]. In addition, MRI images are defined by the plane in which they are acquired, with the imaging coordinate system consisting of three orthogonal planes to describe the standard anatomical position of a human.

### 2.1.1.7 MRI test parameters

MR images are generated through the application of specific pulse sequences, predominantly SE or GE. These two sequences exhibit several distinctions. Firstly, SE sequences employ a single RF pulse, allowing for shorter TE compared to GE sequences. Secondly, GE sequences typically employ low flip angle excitations (e.g., 5°- 40°) in contrast to the 90° flip angle used in SE sequences. Moreover, SE sequences tend to have longer TR and TE durations [38, 50, 55]. It should be noted that additional test parameters further influence the resulting MR image, which will be discussed subsequently.

**Proton density:** The tissues with a higher density of protons (hydrogen atoms) produce higher signal intensities and appear brighter on the image [56].

**T1-weighted:** T1-relaxation times are prolonged with higher magnetic fields, and differences between tissues are often reduced, leading to a reduction of contrast in T1-weighted images. The sensitivity to gradients in magnetic susceptibility is increased with field strength, as the magnet field inhomogeneities increase proportionally to the product of magnetic field strength and magnetic susceptibility. T1-weighted images in MRI are generated by manipulating the TR between two RF excitation pulses. This sequence of RF pulses results in a specific timing that highlights the signal emanating from tissues with short T1 relaxation times. The resulting images are characterized by bright signals from fat tissue within the body. In addition to timing, the contrast and brightness of T1-weighted images are largely determined by the T1 properties of the imaged tissues. To achieve optimal T1-weighted contrast, short TE and TR times are used. These imaging parameters are crucial for the effective interpretation of T1-weighted images in clinical settings [57].

**T2-weighted:** T2-weighted images are produced by using longer TE and TR values. The contrast and brightness of T2-weighted images are predominantly determined by the T2 properties of the tissue. The timing of the RF pulse sequences used to make T2-weighted images highlights the differences in the T2 relaxation time of tissues, with fat and water appearing bright due to their unique T2 values. In T2-weighted imaging, protons within the body lose phase coherence following an RF pulse due to spin-spin interactions within the tissue (T2 relaxation) and the local static magnetic field's inhomogeneity. The de-phasing caused by T2 relaxation is a random, unrecoverable process, while the de-phasing caused by magnetic field inhomogeneity can potentially be recovered. T2-weighted imaging is a type of MRI sequence that provides a way to visualize tissue characteristics and highlight differences in the T2 relaxation times of tissues. T2 relaxation time is the time it takes for

the excited protons to return to their original state after a radiofrequency pulse is applied. By utilizing longer TE and TR values, T2-weighted imaging can capture more information about the spin-spin interactions and magnetic field inhomogeneity of the tissues being imaged. This allows for improved contrast between tissues with different T2 relaxation times, making it particularly useful for detecting certain pathological conditions such as edema, inflammation, and tumors [39].

**Flow:** During MRI scanning of a vessel containing flowing blood, the blood within the slice is affected by the radio wave generated by the energizing RF pulse. However, when the MR signal is sampled, the blood that was influenced by the radio wave will be replaced by new blood flowing into the slice without magnetization. This is because the radio wave causes the magnetic moments of the blood to align in a specific way, but as the blood flows out of the slice and is replaced by new blood, the magnetic moments no longer align and no signal is acquired from that region. As a result, the vessel appears black on the MRI image. This phenomenon is known as flow-induced dephasing and is an important consideration in interpreting MRI images of blood vessels [58, 59].

**Pulse sequence:** The pulse sequence actually executed during the measurement is defined from parameters selected by the operator and variables defined in template files [60]. It is important to mention that each phase-encoding step requires a new pulse sequence the total image acquisition time will depend on the product of TR (time interval between pulse sequences) and NP (number of phase-encoding steps). Conventional pulse sequences such as SE and GE acquire only one phase-encoding step (one line of k-space) per TR, making the image acquisition time considerably long [60].

**Echo time:** It is the time between the delivery of the RF pulse and the receipt of the echo signal [61, 62].

**Inversion time:** Is the time between 180° inverting pulses and the 90° pulses [38, 63].

### 2.1.2 Magnetic susceptibility artifacts in biopsy needles

Magnetic susceptibility refers to how much material is magnetized when placed in a magnetic field. Materials with high susceptibility can distort the magnetic field around them and create image artifacts on MRI scans [44, 64]. In the majority of instances, MR image artifacts primarily impact the diagnostic significance rather than patient safety. Artifacts that compromise image quality can obscure critical information or lead to misrepresentations of a device’s position within the MR image. This is particularly evident in cases such as during needle insertion, the placement of X-ray markers, or radioactive seeds [65]. In such scenarios, safety considerations become critical for the overall diagnostic procedure. The presence of susceptibility and RF artifacts is contingent upon various parameters, including the magnitude and orientation of  $B_0$ , the alignment of the medical device relative to  $B_0$ , and the specific MR pulse sequence parameters employed. Susceptibility measures the magnitude to which a material becomes magnetized when

located in a magnetic field environment. MRI relies on the interaction of magnetic fields with tissues within the body. Depending on their magnetic properties, materials can be classified as paramagnetic, diamagnetic, or ferromagnetic. Paramagnetic materials are attracted to magnetic fields and can cause local distortions in the magnetic field within the body. This can lead to an increase in the signal intensity on MRI images, resulting in affected tissues appearing brighter than surrounding tissues. Examples of paramagnetic materials used in MRI include gadolinium-based contrast agents. Diamagnetic materials, on the other hand, are weakly repelled by magnetic fields and do not cause significant distortions in the magnetic field within the body. Therefore, they do not greatly affect the MRI signal intensity. Most tissues in the body, such as bone, muscle, and fat, are diamagnetic. Ferromagnetic materials, however, are strongly attracted to magnetic fields and can retain their magnetization even after the external magnetic field is removed. When present in the body, ferromagnetic materials can cause significant distortions in the magnetic field, leading to image artifacts and posing serious safety risks to patients. Examples of ferromagnetic materials that can cause problems in MRI include iron, cobalt, nickel, and certain alloys and compounds that contain these metals [38,41,63]. Particularly, magnetic susceptibility can be defined as the degree of magnetization in an object in response to an external magnetic field. Moreover, MRI susceptibility artifacts are caused by field inhomogeneities around an object caused by the interaction with an applied magnetic field. Comprehensive artifact testing is necessary to provide artifact information for all relevant configurations [8]. Artifacts do not primarily affect patient safety but rather have high clinical relevance for adequate diagnosis in detecting the exact position of the devices involved in MRI procedures such as needles, cannulas, guide-wire, or implantation of markers or radioactive seeds and stents [66]. The theoretical background of magnetic susceptibility artifacts in MRI involves understanding the physical principles behind magnetic susceptibility and its impact on the imaging process:

- **Magnetic susceptibility:** Magnetic susceptibility is a property that describes how a material responds to an external magnetic field. It quantifies the degree to which the material becomes magnetized when subjected to a magnetic field. The susceptibility of a material is influenced by its chemical composition and microscopic structure.
- **Magnetic field distortions:** When a material with a different magnetic susceptibility is placed within a uniform magnetic field, it causes local magnetic field distortions around it. This occurs due to the interaction between the external magnetic field and the induced magnetization within the material.
- **Phase and frequency shifts:** The local magnetic field distortions caused by variations in magnetic susceptibility lead to phase shifts and frequency shifts in the MRI signal. Phase shifts refer to a change in the relative timing of the MRI signal, while frequency shifts correspond to a change in the resonant frequency of the signal.

- **Signal loss and pile-Up:** Variations in magnetic susceptibility can result in signal loss or pile-up in the MRI image. Signal loss occurs when the local magnetic field distortions cause the dephasing of the MRI signal, leading to a reduction in the detected signal intensity. Signal pile-up refers to the accumulation of signal in regions adjacent to areas of high magnetic susceptibility, as the distorted magnetic field affects the encoding of the signal.
- **Blooming and Artifacts:** Blooming artifacts occur when high magnetic susceptibilities objects, such as metallic implants or air-filled cavities, exhibit a larger apparent size in the MRI image than their actual size. This blooming effect is caused by magnetic field distortions spreading beyond the physical boundaries of the object.

To mitigate magnetic susceptibility artifacts, various strategies are employed. Gradient echo sequences are often used instead of spin echo sequences, as they are less susceptible to susceptibility artifacts. Advanced imaging techniques, such as parallel imaging and iterative reconstruction algorithms, can also help reduce susceptibility artifacts by accounting for the underlying magnetic field distortions [67, 68].

## **2.2 Current challenges in MR-guided biopsy interventions**

The central core of an MRI machine produces a powerful magnetic field, which poses significant risks to human health and safety. As such, access to this area must be restricted to authorized personnel who have received appropriate training in MRI safety procedures. Prior to entering the MRI suite, patients must be screened for the presence of any metal devices, such as pacemakers or other implants, to avoid potential harm from magnetic forces or radiofrequency heating [64, 69]. In addition, the interaction of the high magnetic field of the MR environment with paramagnetic, and diamagnetic materials for the intervention devices such as needles, stents, guide-wire, and biopsy needles during the imaging can lead to artifacts in the image, degrading the quality of the image. Moreover, these materials depend on the torque and displacement in the magnetic field. For interventional procedures guided by MRI, particular non-magnetic components with low susceptibility are required due to the powerful magnetic field (usually between 15,000G and 30,000G or 30,000 to 60,000 times the earth's magnetic field) [70]. Nowadays, the majority of the research has been conducted aiming to design interventional biopsy needles for MRI-guided procedures with minimum artifacts. Many parameters should be taken into account such as materials type, the magnetic field strength, needle angulation inside the MRI fields, MRI sequences, and mechanical performances in resistance to kinking. Besides, to ensure patient safety in the MR environment with an ongoing commitment, the American Society for Testing and Materials (ASTM) international standard protocol needs to be followed [71–74]. New materials and innovative fabrication strategies have been proposed for satisfying the strict

requirements of the MRI environment [36]. In most developments, there is a trade-off between the proper mechanical characteristics, which depends on the clinical application, and the artifact behavior during MR imaging [75]. When performing tissue biopsies or needle injections, metallic guides are commonly utilized and typically manufactured using specialized surgical materials such as treated stainless steel grades 316L and 316LVM, as well as cobalt-chromium (CoCr) and nickel-titanium (NiTi) alloys. Another alternative is the use of carbon tubes. However, all these solutions are not optimal, as stainless steel/CoCr needles cause artifacts in MRI images, degrading the accuracy of biopsy puncture. On the other hand, utilizing carbon and nitinol in the needle with an aim to improve image quality leads to an increase in the cost of the needle product. Therefore, there is a need to develop and introduce new materials used for biopsy needles that are compatible with MRI-guided interventions and ensure patient safety.

To meet these challenges, a range of materials, including nylon, polytetrafluoroethylene (PTFE), polyether ether ketone (PEEK), wood, copper, ceramics, acetal co-polymers, aramid, polyester, and various fibers, have been proposed and investigated for their compatibility with the MRI environment [36, 73, 76–78].

These materials can be a solution for the construction of biopsy needles which have the required mechanical properties and many other materials that come under MRI compatible category and present acceptable artifacts [79]. Other materials that have produced higher susceptibility artifacts, such as aluminum, titanium, nitinol, and magnesium, will present high artifacts, but they may still be acceptably used due to mechanical properties in medical applications [80, 81]. In the interventional needles case, they can have high susceptibility artifacts on MRI scans but can still be used if they are placed at a small distance from the region of interest. This means that the area of the body being imaged should not be covered by the artifact caused by the needle. The physician performing the procedure should be aware of this and position the needle accordingly to avoid interference with the image of the region of interest. For example, a non-magnetic stainless steel biopsy needle has high susceptibility artifacts but can also be accepted at a small distance from the region of interest [80]. In addition, many studies proposed improving the MRI visualization by using active and passive methods of MRI artifacts by selecting material and passing under a treatment process such as polished, coating, etc. [21, 82, 83]. However, the material modifications can still result in a distorting influence on the homogeneity of the magnetic field, which can lead to distortions in the MR image due to susceptibility artifact [84, 85]. It is important to re-evaluate its MR compatibility because some manufacturing processes can alter the magnetic properties of the element. Another factor to consider is the material's conductivity and the needle's design, whether long like a guide wire or short like a needle. In addition, the presence of pulsed RF and gradient fields produce eddy currents, heating, and artifacts [67, 86, 86, 87]. It is important to mention that assessing MRI artifacts should be implemented at an early stage of the development process of

biopsy needles to check the behavior of materials within or close to the imaging field of the MRI system. A commercially available interventional needle is the carbon fiber needle produced by the Radimed company (Bochum, Germany). This type of needle is well-suited for performing MR-guided interventions at 1.5 T, as it generates fewer artifacts than a titanium alloy needle during an MRI scan. However, it is important to consider that the needle's complete visibility, particularly towards its tip, may not always be guaranteed. This partial visualization can potentially introduce localization uncertainties, affecting the accuracy of its precise positioning within the targeted area [88]. While the stainless steel grade 316L needle is the most common material used for manufacturing needles due to high stiffness but still has drawbacks of enormous artifacts in an image resulting in increased shaft size and unclear tip ending as shown in Fig. 2.7(a). In order to tackle this challenge and compare artifact levels, alternative needle materials have been explored. Examples include gold and austenitic stainless steel, which is a type of stainless steel that contains high levels of nickel and chromium with non-magnetic properties presented in Fig. 2.7(b) and (c) [29].

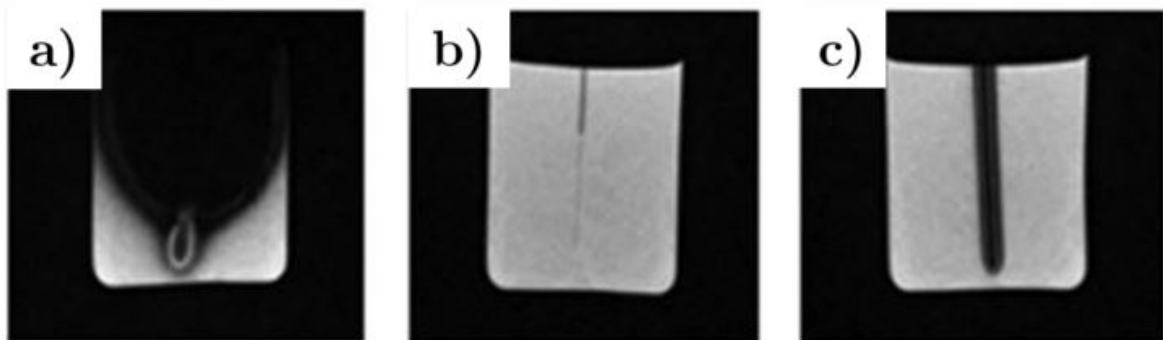


Figure 2.7: Comparison of the three distinct types of MRI artifacts generated by needles a) standard stainless steel needle produced a large imaging artifact; b) gold needle generated a small artifact, and c) austenitic stainless steel needle produced some artifact on the MRI (taken from [29]).

Furthermore, needles made from NiTi highly improve visibility but still suffer from artifacts depending on the image sequences used for MR guidance. Consequently, it does not allow the precise placement of the needle [89]. Alternative techniques, such as the use of ceramics needles, have been proposed for enhanced visualization [90,91]. However, these concepts are associated with certain limitations such as reduced sharpness, instability, or increased wall thickness. In addition, the presence of iron in needle alloys can limit their utility for MRI procedures. To overcome this limitation, special alloys with high nickel content have been developed, with nickel percentages ranging up to 35% or 49%. As the percentage of nickel in the alloy increases, the degree of artifact produced by the needle during MRI imaging decreases in an inverse proportion [92]. Another commercial example of the currently used interventional needle is the StarBurst MRI radiofrequency ablation



(RFA) needle manufactured by AngioDynamics company (USA), which is compatible with MRI during needle placement. However, it produces massive artifacts during MRI procedures [88,89]. Fig. 2.8 displayed the actual length for the RFA needle as 10 mm while the image produced by the MRI records a length of 13 mm. This difference of 3 mm can make it difficult for clinicians to accurately locate the needle tip in relation to the target during surgery. Furthermore, Fig. 2.9 shows examples of needles causing two kinds of big or

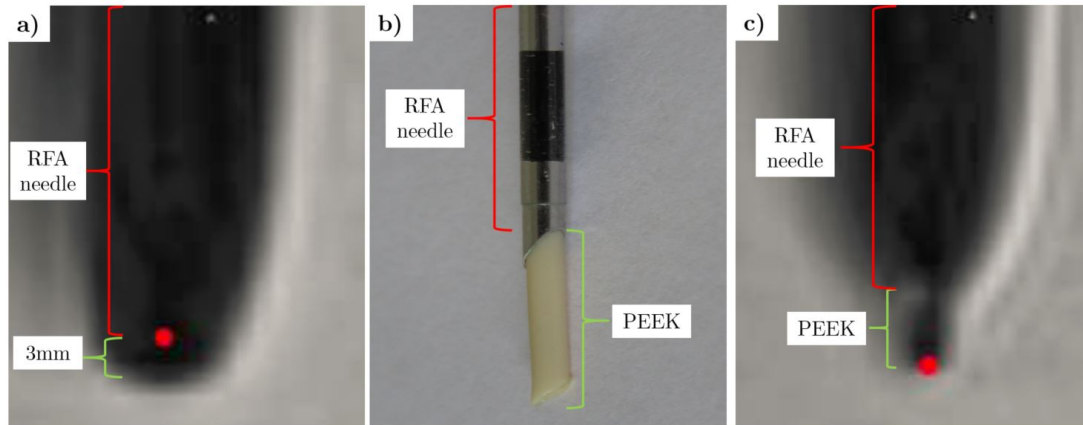


Figure 2.8: An MRI radio-frequency ablation (RFA) needle [93] with preliminary steps to reduce the artifacts during MRI: a) the original RFA needle under MRI shows significant artifacts with a 3 mm error from the real length shaft, represented at the red point, b) to reduce artifacts, a PEEK rod material was attached as a tip to the RFA needle and c) the MRI image for the RFA needle with the PEEK rod attached shows a significant reduction in the artifact, with the rod point indicating the reduced artifact area.

small artifacts that can not show the needle end in the MR image. Assuming that we have a smaller suspected tumor, and the presence of such an artifact, it is difficult or impossible to reach such a target precisely. Besides, the needles manufactured by SOMATEX Medical Technologies company (Berlin, Germany) are non-magnetic metal alloys that provide MRI visibility. Nevertheless, their needle material produces large artifacts than the original size as shown in Fig. 2.10. Biopsy needles manufactured by ITP company (Bochum, Germany) made from conventional nitinol were used in MRI interventional procedures. Despite that, it still produces artifacts [94–96]. Polyetheretherketone (PEEK) and polymer-based needles have recently been developed to reduce artifacts in MR imaging [36,95,97,98]. However, those materials are limited by their low bending stiffness [97]. Consequently, fiber-reinforced-polymer designs were introduced, which showed improved mechanical properties in an MR guide wire prototype [99]. Another promising glass-fiber reinforced guide wire [100] was developed and tested in several patients [77,101]. It seems that such fiber-reinforced needles have the potential to become suitable needles for MR-guided interventions. However, despite their potential advantages, the clinical adoption of fiber-reinforced needles remains limited due to several factors. For example, the size, shape, and

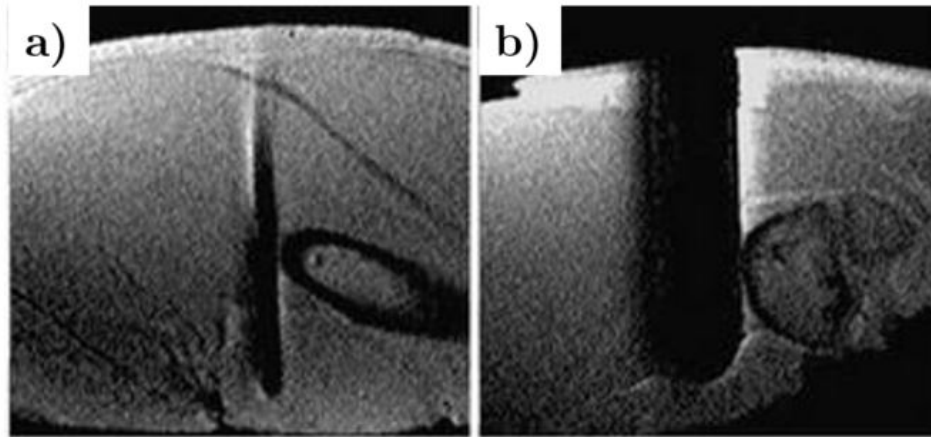


Figure 2.9: Example of MRI needles artifacts during insertion: a) the needle entrance is not clear and a boundary is not clear, b) needle is showing enormous artifacts (taken from [37]).

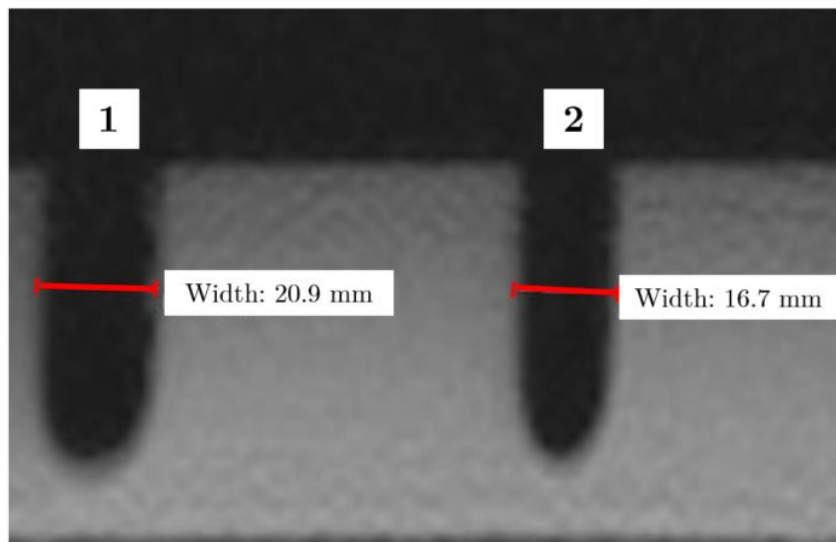


Figure 2.10: Preliminary test for measuring width artifacts in SOMATEX needles in MRI images using Dicom viewer software: needle labeled (1) is 20 G with the width of 0.95 mm while in the image it is given 20.9 mm. Meanwhile, the needle labeled (2) is 22 G with a width of 0.70 mm, but appears as 16.7 mm during MRI imaging due to width artifact.

material properties of these needles may not be suitable for certain applications, which limits their usability. Additionally, the production and manufacturing of such needles can be more complex and costly than that of traditional metal needles, which further limits their availability and commercialization. Artifacts influencing image quality can hide information, provide unrealistic object sizes and result in an incorrect depiction of the position of a device. Such an error can lead to positional distortions of up to several millimeters, as shown in Fig. 2.11 of ceramic zirconia ( $ZrO_2$ ) cannula within MRI-guided surgery [66].

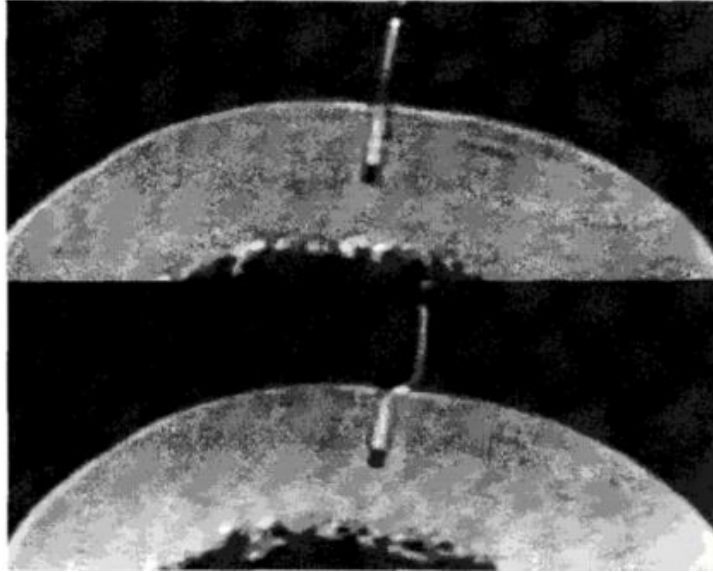


Figure 2.11: This study presents an example of a needle artifact in an MR image that results in positional errors (taken from [66]).

Susceptibility artifacts resulting from the presence of needles in MRI scans are influenced by several factors, including the strength and orientation of the main magnetic field  $B_0$ , the alignment of the needle with respect to the magnetic field  $B_0$ , the MRI pulse sequence parameters, the composition of the needle, and the imaging parameters employed during the scan. These artifacts manifest as inhomogeneities in the magnetic field around the needle, caused by the alteration of magnetic field lines, and can vary based on the needle's position within the scanner. It is important to consider these factors when performing MRI-guided needle procedures in order to minimize the impact of susceptibility artifacts on the quality. A practical example highlighting the effects of SE and GE sequences is presented in Fig. 2.12 [102]. The study compares the use of titanium (T) and ceramics (C) needles in SE and GE sequences, as shown in Fig. 2.12 (b) and (c). It is observed that GE sequences are more susceptible to artifacts caused by magnetic field disturbances induced by both titanium and ceramics needles compared to SE sequences. The presence of metallic objects can give rise to significant susceptibility effects, resulting in various artifacts such as signal loss, distortion, and blooming in the vicinity of the object. These artifacts manifest as signal voids, geometric distortions, or bright streaks in the acquired MR images. On the other hand, SE is less affected by T and C needles compared to GE sequences. While SE can still exhibit artifacts near metallic objects, they are typically less severe than GE sequences. This is because applying two RF pulses in SE sequences helps mitigate some of the artifacts caused by local magnetic field disturbances. However, if the metallic object is large or composed of highly magnetic materials, it can still produce artifacts in spin-echo images, albeit to a lesser extent. It's important to note that the severity and specific characteristics of artifacts can vary depending on various factors, including the composition and size of the object, the imaging parameters used, and the

specific MRI system. The best visibility was noted for the needle made from carbon-nitinol

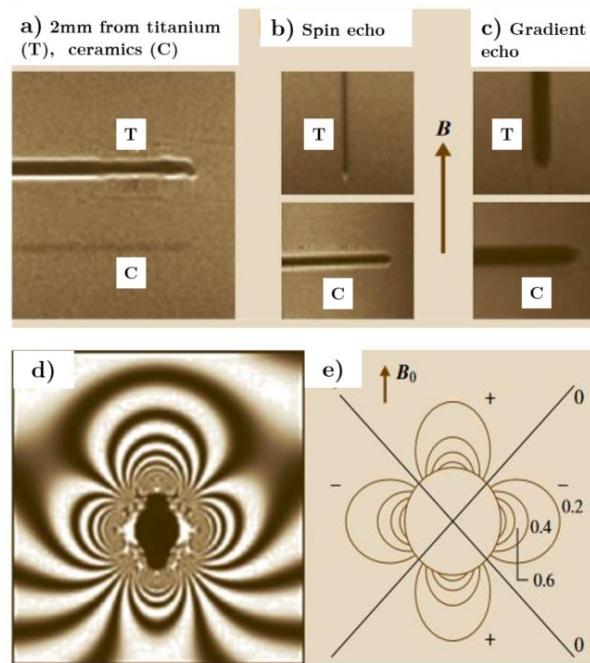


Figure 2.12: Examples of artifacts needles in MRI: a) needle from titanium referred to as (T) and from ceramic referred to in the image as (C) in interventions MRI. b) artifact from the needles according to orientation and spin echo sequence, c) needles artifact according to orientation and gradient sequence, d) field mapping of needle artifact, a cross-section of a 1 mm titanium probe e) graphic view of the magnetic field perturbation; spins near the object to the left and right are at the lower resonance frequency, whereas those above and below the object are at the higher resonance frequency (edited and taken from [103]).

at an angle of  $90^\circ$  which is against the main magnetic field. While at the angle of  $30^\circ$ , the artifact was hardly recognizable in SE sequence as shown in Fig. 2.13, this gives difficulty to recognize the accurate location inside the body. The observed phenomenon from Fig. 2.13 of decreasing artifact contrasts with decreasing angles in GE and SE images of a carbon needle with a nitinol mandrin immersed in gadolinium-doped water can be attributed to the influence of magnetic field distortions and susceptibility effects. When a metallic object, such as the carbon needle with a nitinol mandrin, is placed within the strong magnetic field of an MRI scanner, it creates local magnetic field distortions around itself. These distortions can cause variations in the magnetic field strength and uniformity in the vicinity of the object. In GE sequences, the presence of magnetic field distortions due to the metallic object can lead to signal loss or distortions in the acquired images. This can result in reduced contrast between the artifact and the surrounding tissue or water, leading to a decreased visibility of the artifact as the angle decreases. As the angle between the metallic object and the main magnetic field decreases, the distortions become more pronounced, further impacting the image contrast [88]. In the SE sequence, they

generally exhibit fewer susceptibility artifacts compared to GE sequences, the presence of a carbon-nitinol needle can still introduce local magnetic field variations and susceptibility effects, leading to signal loss or distortions. Therefore, similar to gradient echo sequences, the contrast between the artifact and the surrounding tissue or water may decrease with decreasing angles. A comprehensive assessment has been conducted to evaluate the efficacy

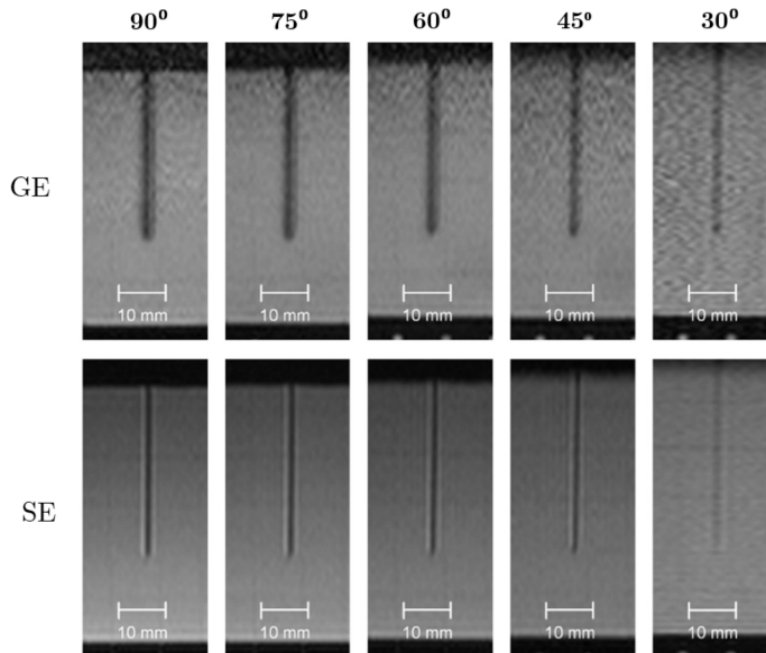


Figure 2.13: Different angulation against the main magnetic field shows decreasing artifact for the carbon-nitinol needle in two sequences GE and SE adopted from [88].

of the current commercial MRI biopsy needles, as presented in Fig. 2.14. This assessment focused specifically on the materials selection of the biopsy needles and the potential for artifacts to be generated during an MRI scan. To facilitate a direct comparison of the effects of different materials, the material composition of each needle was analyzed, and characteristics of the artifacts in the MRI environment were presented in Table 2.1, clearly highlighting the appearance of each artifact in MRI imaging. Linear pathways in medical surgeries are sometimes not feasible or possible due to sensitive structures or bones on the line. Therefore, standard conventional needles tend to kink when strongly bent during the procedure when the path is not straight. This indicates the limitation in the degree of flexibility, and only straight lines between the entry point and the target location are possible, as shown in Fig. 2.15 [105, 106].

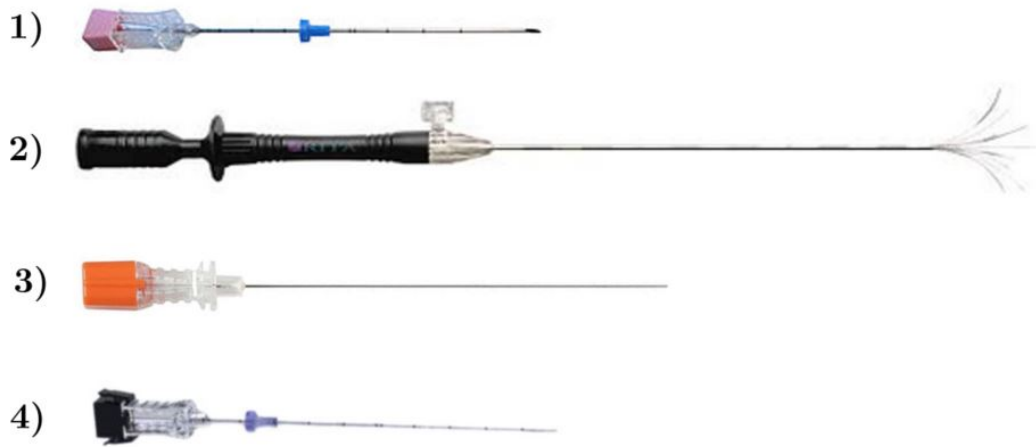


Figure 2.14: Selection of commercial MRI needles: 1) SOMATEX needle [14], 2) StarBurst RFA needle [93], 3) Radimed needles [91] and 4) ITP needle [104].

Table 2.1: Comprehensive comparison table of commercially available MRI-compatible biopsy needles. It includes information on manufacturing sources, composition, gauge (G) sizes, application areas, and MRI visibility properties.

Manufacture	Composition	Gauge (G)	Applications	MRI visibility
SOMATEX needle, Medical Technology GmbH, Germany [97]	Special non-magnetic alloy Nitinol	20 and 22	Intraoperative tumor localization/pain therapy	Produce massive artifacts
StarBurstXL needle, RFA, Angiodynamics company, USA [62]	Grid from metal; Flexible polymer trocar section	14	Liver ablation	Produce artifacts inside the tumor
Radimed needle, Radimed GmbH, Germany [49]	Carbon fiber/Nitinol	Range (18-21)	Pain therapy	Produces artifacts
ITP Innovative Tomography products, Germany [96]	Nitinol	Range (21-22)	Pain therapy	Produce massive artifacts

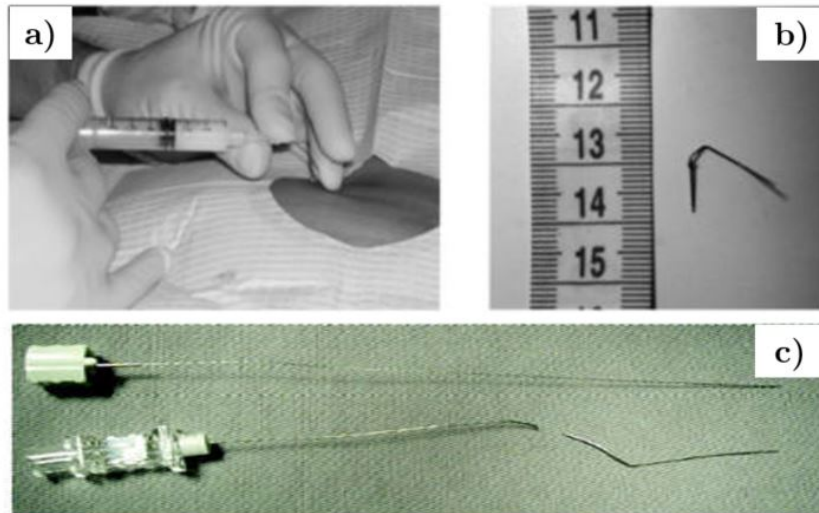


Figure 2.15: The current clinical problem for the conventional needle: a) the clinicians tend to bend the needle during intervention surgery, b) and c) present fractured biopsy needle after intervention procedure (taken from [107]).

In summary, there are mainly two requirements that need to be fulfilled by the needles to be developed:

1. Enhances the visibility of biopsy needles in the MR image without introducing excessive artifacts.
2. Optimizing the mechanical properties of conventional needles, which are normally used in MRI procedures.

### 2.2.1 Criteria for selecting compatible materials for biopsy needles

MRI imaging systems demanded particular parameters for biopsy needles used in the MRI, which should be compatible, effectively viewed, and safety materials used to fabricate the biopsy needles with durable mechanical performance [108]. Thus, to be MRI-compatible and safe biomaterials, three main aspects need to be considered: (1) degree of susceptibility artifacts, (2) ferromagnetic attraction, and (3) RF-associated device heating [109]. For example, inductive heating can be a concern when performing MRI-guided procedures, such as biopsy. To mitigate this effect, diamagnetic materials, such as composite ceramics and polymers, are recommended for use in biopsy needles. However, optimizing these materials to achieve the required stiffness and hardness for thin-wall tubes with small diameters can be challenging. Ensuring sufficient elasticity is also important but can be difficult to achieve. Even with the use of safe and compatible materials, artifacts may still occur, resulting in distortions in MRI images and complicating the accurate determination of needle position. Therefore, careful material selection and optimization are necessary to minimize such artifacts and ensure accurate needle placement [43, 67, 109].

Materials with good magnetic compatibility, such as ceramics and thermoplastic polymers, are commonly used in MRI-guided procedures due to their electrical insulating properties, which minimize artifacts and reduce the risk of electrical hazards. However, some metallic materials, such as copper, brass, and aluminum, may also be suitable for use in experimental designs of biopsy needles due to their good magnetic properties. Careful consideration should be given to the specific application and potential risks associated with these materials, as metallic materials may generate more artifacts than non-metallic materials. Overall, selecting materials with appropriate magnetic and electrical properties is crucial for the safe and effective performance of MRI-guided procedures [66,67].

### **2.2.2 Computational methods for artifacts detection**

Medical images such as MRI, CT, and US are commonly used in clinical practice but may contain artifacts that can obscure important diagnostic information. Machine learning techniques offer a promising solution for artifact detection, enabling automated analysis of medical images to identify areas with high susceptibility artifact levels and quantify the dimensions of the artifact. To develop a machine learning algorithm for artifact detection, the first step is to collect a large dataset of medical images that includes both normal and artifact-affected images. This dataset can be curated from existing medical image archives or generated specifically for this purpose. The quality and diversity of the dataset are critical factors in the success of the machine learning algorithm, as a larger and more diverse dataset can help the algorithm generalize better to new cases. Once the dataset is collected, data pre-processing is necessary to extract relevant features that the machine learning algorithm can use. This may include image normalization, filtering, and segmentation, which can help reduce noise and enhance the visibility of important structures. Feature extraction is a critical step in the machine learning pipeline and uses various techniques. After feature extraction, the next step is to train the machine learning model using the supervised or unsupervised approach, where the algorithm learns from labeled examples of normal and artifact-affected images. The performance of the algorithm can be evaluated using various metrics such as accuracy, sensitivity, and specificity. Once the model is trained, it can be used to classify new medical images as normal or artifact-affected [110,111]. In current clinical practice, the clinicians evaluate the artifacts manually according to the standard American Society for Testing and Materials (ASTM): F2119 for evaluation of MRI artifacts from passive implants directly [112].

However, it is a time-consuming procedure for medical staff and limited reproducibility [113]. Therefore, recent studies have proposed various assessment methods for measuring artifacts in MR images, such as automatic and machine learning detection approaches [89, 114–116]. These approaches apply specific algorithms such as density-based clustering algorithm (DBS), hierarchical algorithm (HDA), and K-means algorithm [117, 118]. For example in DBS, the clustering does not work well for sparse datasets or data points with varying



densities, which can result in noisy clustering outcomes. In addition, we cannot control the K value (number of clusters) like in K-means. DBS requires the radius and number of cluster member parameters to be pre-determined, which may be challenging to identify accurately in this case. While a hierarchical algorithm (HDA) clustering needs a set of nested clusters that are arranged as a tree. HDA generates overlapping, nested clusters [116]. The aim is to generate non-overlapping clusters using K-means to distinguish between cluster members clearly. To this end, each pixel is assigned to only one cluster and is not included in multiple or overlapping clusters. However, these algorithms are often limited to specific medical applications, such as those related to the brain and breast [119–121]. Furthermore, automatic detection of biopsy needles has been restricted to specific imaging modalities such as photoacoustic, computed tomography (CT), and MRI [113, 117, 122]. Regarding MRI applications, Mehrtash et al. developed a detection approach specifically for visualizing a prostate biopsy needle [113]. There is a lack of applying a simple machine learning approach for detecting the artifacts for MRI spinal biopsy needle applications [89, 122]. Therefore, To address this gap, our work proposes an unsupervised machine learning approach based on K-means clustering that is simple to implement and computationally efficient. The method utilizes only one hyperparameter, which is the number of clusters (K) [117, 118]. Moreover, K-means clustering is unaffected by varying densities of data points since it uses pixel intensity values for clustering. Clustering involves dividing the set of data objects into non-overlapping subsets (clusters) such that each data object is part of only one subset. Additionally, unsupervised machine learning saves time on annotation for generating ground truth, which is required for performing supervised machine learning tasks. Overall, machine learning approaches can be a powerful tool for detecting artifacts in medical images, and can potentially improve the accuracy and efficiency of medical image analysis.

### **2.2.3 Mechanical characterization used in interventions MRI biopsy needle**

#### **2.2.3.1 Stress-strain analysis**

The stress-strain test is one of the most common methods in the evaluation of the mechanical properties of developed prototypes [123–125]. This test is designed to determine the response of a material to an applied load, providing valuable information on its mechanical behavior. In the context of a bending test, the inhomogeneous nature of material deformation is reflected in the material’s characteristics. Therefore, the stress and strain experienced by a point on a bent specimen are dependent on its location relative to the neutral axis of the cross-sectional area of the specimen [126]. Any stress-elongation curve consists of three main points known as the yield point, the ultimate tensile point, and the fracture tensile point as shown in Fig. 2.16. The yield point represents the maximum limit where the sample still can be elastic [128]. While the plastic region is the area

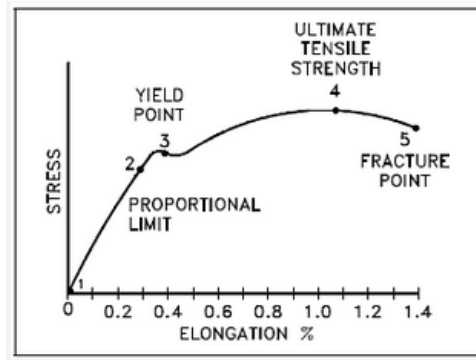


Figure 2.16: Stress strain curve (taken from [127]).

prior to the yield point where the sample can return back to its original shape after removing the load which is represented by Young's modulus. The tested sample is placed in between two grips of movable and stationary fixtures, in a screwdriver device which pulls the sample until it breaks by measuring the applied load versus the sample elongation. Young's modulus is the ratio of stress to elongation within the elastic region. It's also known as the modulus of elasticity which is measured by the slope of elastic stress and elongation in the graph. A stiff material will have a high module of elasticity while a flexible material will have a low module of elasticity [129]. In this work, Young's modulus measurement will be considered one of the main parameters to select the best samples. The yield point is defined as the stress at which the sample begins to deform and move under force. Prior to the yield point, the sample will deform elastically, and it can return to its original shape when the stress is removed. Once the Yield point is passed it leads to the loss of its properties to come back to the original shape and the deformation will be permanent in the sample. The measurement of this parameter is important together with the measurement of Young's modulus to choose the optimal proposed sample [127]. The ultimate tensile strength represents the plastic region for the sample elongation [130]. The ultimate tensile strength is described by two measurements which are the maximum force that can be applied to the sample in MPa, and the percentage of elongation that the sample can resist before its break. Fracture tensile stress is the state of material where the sample elongates and then separates into two pieces under the action of tension applied by the machine [131]. Similarly to the ultimate tensile point, the fracture tensile point is characterized by two parameters such as fracture force in MPa and the elongation of the sample in percentage. An example of a 2-point bending test for a crystal sample is presented in Fig. 2.17. The stress-strain test known as the mechanical bending test is a crucial method for determining the ductility, bending strength, and resistance to breaking of various materials [133]. These characteristics are particularly important in assessing whether a material can withstand higher forces and stresses, especially in the construction of biopsy needles that involve ductile materials subject to bending forces. Furthermore, the bending test is a suitable technique for assessing the tensile strength of brittle materials

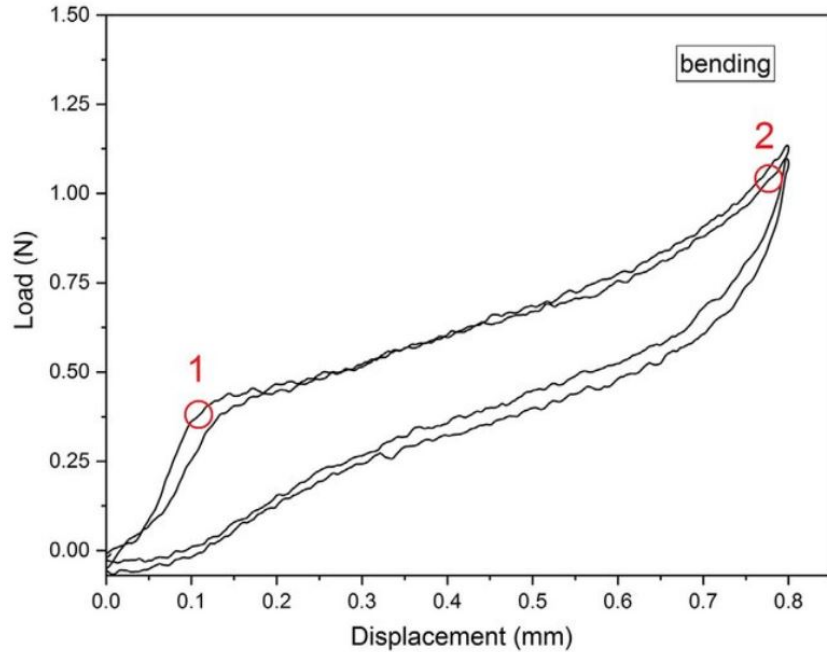


Figure 2.17: An example of a bending test for a sample with an applied force of 1.125 N and maximum displacement at 0.8 mm. In this image, the load-displacement curve of the two-point bending test was performed for two cycles for a Single crystalline Ni-Mn-Ga is well known as a prototype ferromagnetic shape memory alloy (FSMA). The red circles indicate the forces used for stress distribution calculations (taken from [132]).

that are prone to cracking when tested under uniaxial tension. Various types of bending tests can be performed, including cantilever, 2-, 3-, and 4-point bending tests [134].

### 2.2.3.2 Finite element analysis (FEA)

FEA technique has gained widespread use in the study of biomedical challenges [135]. Specifically, FEA has been intensely used in biomedical contexts to examine, simulate, and predict the material behavior and non-linear biomechanical properties of soft tissues, organs, bones, and joints. It is also instrumental in applications of modeling, testing, and verification of medical device designs, such as artificial implants, stents, biopsy needles, catheters, and guide wires. The number of reported studies that utilize finite element modeling and related computational numerical methods in the advancement of biomedical and clinical research, development, diagnosis, and treatment applications has constantly increased since 1980 [135–138]. The modeling step is preferred due to the software’s flexible options, lower time and cost requirements, and ability to simplify complex designs for prototyping. It provides an intermediate step in the proposed design process to apply many mechanical tests and ensure the desired requirements are met. FEA encompasses several crucial testing steps in the simulation process, which are fundamental in achieving accurate and reliable results [139, 140]:

- Mesh generation: the first step in FEA is to divide the problem domain into smaller elements, such as triangles or tetrahedra in 2D or 3D problems, respectively. These elements form a mesh that represents the geometry of the structure or system under analysis.
- Governing equations: the behavior of the system is described by a set of governing equations, typically partial differential equations (PDEs). These equations represent physical principles such as the conservation of mass, momentum, or energy. In the context of solid mechanics, the most common equation is the linear elasticity equation.
- Shape functions: each element in the mesh is associated with a set of shape functions. These functions interpolate the behavior of the unknown variables within the element based on the known values at the element's nodes. Shape functions are typically polynomials of a certain order.
- Displacement approximation: the unknown variables in FEA are often the displacements of the structure or system. Using the shape functions, the displacements are approximated as a linear combination of nodal displacements within each element.
- Element equations: by substituting the displacement approximation into the governing equations, element equations are derived for each finite element. These equations are typically expressed in terms of nodal displacements, element properties (such as material properties), and element geometry.
- Assembly: the element equations are assembled to form a global system of equations that represents the behavior of the entire structure or system. This involves combining the element stiffness matrices and load vectors into a large system matrix and vector.
- Solution and post-processing: the global system of equations is solved numerically using techniques such as the finite element method or matrix inversion methods. Once the solution is obtained, post-processing techniques are applied to analyze and visualize the results, such as stress distribution, displacement patterns, or fluid flow characteristics [141, 142].

## 3 Materials and Methods

This chapter offers a comprehensive overview of the materials utilized for the fabrication of biopsy needles, including their dimensions and mechanical properties. Additionally, the chapter outlines the design concept behind the proposed biopsy needles, followed by a detailed description of the fabrication process. The performance of the biopsy needles was subsequently evaluated through a series of experimental tests, including MRI scanning, mechanical testing, and FEA modeling. The MRI scanning was conducted in two stages: first, with the proposed needles fixed in a gelatin phantom, and second, with the needles fixed in a biological-engineered 3D tumor model phantom. To facilitate artifact detection for the biopsy needles, a machine-learning approach was applied to the MRI images. A detailed account of each test and its results is presented in this chapter. This research provides valuable insights into the development of biopsy needles, which could potentially improve the accuracy and reliability of biopsy procedures.

### 3.1 Materials selection protocol

As previously mentioned, designing biopsy needles require adherence to strict MRI safety guidelines. This includes ensuring that the coaxial needle is compatible with the MRI imaging system and poses no risk to the patient, such as magnetic attraction, heating, or electric charging. Additionally, acceptable levels of image artifacts must be maintained [36]. To fulfill the strict requirements, a new combination of non-metallic materials is proposed in this study. Following the magnetic-induced deflection force was measured on medical devices in the magnetic resonance environment, following the ASTM (F2052-/15) standard test method [72, 143]. Additionally, the proposed needle design adheres to the ISO (International Organization for Standardization) 7864:2016 standard requirements for needles and catheters [75, 144] Besides, it is important to consider the trade-off between the new materials used for artifact behavior during MR imaging and the appropriate mechanical characteristics for effective biopsy needles.

Moreover, My investigation focuses on a novel technique for creating a biopsy needle using a multi-layered concept. By employing combination and arrangement of non-metallic materials as presented in Table 3.1. These materials were selected based on the cost-saving benefits of a polymer base that is compatible with MRI and its ability to provide a thin-walled structure with enhanced stability for use in MR interventions. In parallel, a standard NiTi needle manufactured by Innovative Tomography Products company ITP

(Bochum, Germany), with a standard gauge of 21G, was used and listed as a reference for later performance comparison during the tests.

Table 3.1: Raw materials used to fabricate the proposed biopsy needles

Materials	Abbrev.	Manufactured by
Nickel-Titanium alloy	NiTi	ITP Innovative Tomography Products, Germany
<ul style="list-style-type: none"> <li>• Polyether ether ketone</li> <li>• Fluorinated ethylene</li> <li>• Polytetrafluoroethylene</li> </ul>	<ul style="list-style-type: none"> <li>• PEEK</li> <li>• FEP</li> <li>• PTFE</li> </ul>	<p style="text-align: center;">Victrex, UK ZEUS, USA</p>
Fiber bundle	FB	FibreCableConnect (FCC), Germany
<ul style="list-style-type: none"> <li>• Shrink tube Polyester</li> <li>• Polyimide tube</li> </ul>	<ul style="list-style-type: none"> <li>• SH</li> <li>• PI</li> </ul>	Vention Medical Andorson, USA
Glass rod	GR	Hilgenberg, Innovative Glass Products, Germany

## 3.2 Fabrication strategy for the proposed non-metallic biopsy needles

### 3.2.1 Multi-layer concept for polymeric biopsy needles

To improve the strength and stability of biopsy needles, a multi-layer design concept was proposed for a coaxial biopsy needle. An initial prototype of this design concept, as shown in Fig. 3.1(a), was developed using a round PEEK core with a diameter of 1.75 mm, selected from PEEK filament manufactured by Victrex (UK). PEEK, is known for its hardness and form stability. To construct the hollow outer needle, three layers of Polyimide (PI) tubes with three different diameters 1.84 mm, 1.91 mm and 2.01 mm manufactured by Vention Medical (USA), were coaxially arranged in a cascade to counteract the expected bending strain. Each layer has a wall thickness of 0.03 mm. The layers were joined using Loctide 4902 glue. The outer diameter of the final hollow needle is 2.39 mm; the inner diameter is 1.76 mm. With a minimal wall thickness of 0.03 mm at the distal end and a maximum thickness of 0.12 mm mm at the proximal end, as depicted in Fig. 3.1(b).

### 3.2.2 Flexible polymeric biopsy needle

The proposed non-metallic materials used in the fabrication of needles possess favorable mechanical properties, characterized by flexibility, which enables non-linear access to pathologies and prevents kinking or buckling during insertion. These properties enhance the performance and reliability of the biopsy needles, allowing for improved precision and accuracy in medical procedures. Therefore, the second trial of prototyping was accomplished to address the issues of flexibility for nonlinear accesses. In this context, a prototype of a fully non-metallic polymeric needle was developed, consisting of an inner mandarin and an outer hollow sheet.

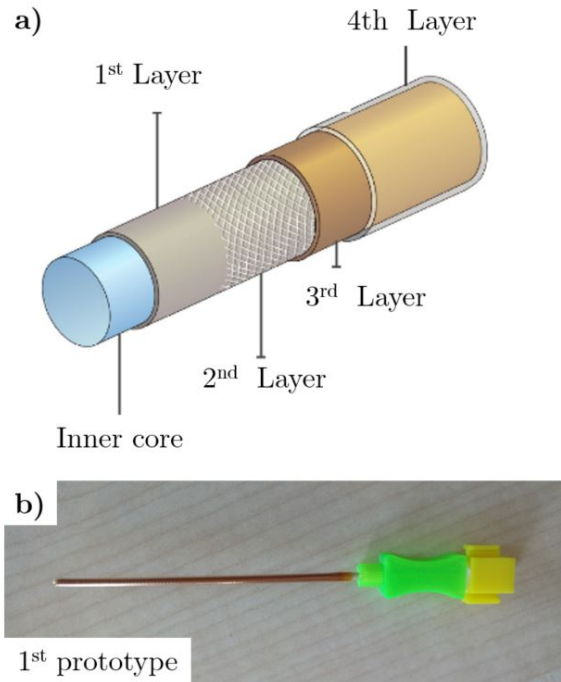


Figure 3.1: An early prototype of the biopsy needle, featuring a multi-layer design: a) CAD design presenting the concept of layers, b) fabricated biopsy needle based on multi-layer concept (published in [145]).

The inner mandrin is made of PEEK as a core produced by Victrex (UK), with an average diameter of 1.21 mm in the range of 21,22 Gauge [20]. The sheet has a multi-layer design combining different layers of thin wall plastic tubes made of (1) PI, with inner diameters of 0.07, 0.073, and 0.77 mm, and (2) PEEK, with an inner diameter of 0.075 and 0.085 mm, produced by Vention Medical Anderson (USA). To ensure the flexibility of the prototype needles, they were tested at three different angles (30°, 60°, and 90°). The work referenced in this statement, which was published in [146] is shown in the Appendix Fig. A.1. A summary of the initial and subsequent trials revealed the successful fabrication of a group of seven non-metallic biopsy needles, consisting of an inner core and outer sheet. The needles were developed using a multi-layer and flexible design, using the standard gauge 21G for biopsy needles.

### 3.2.3 Inner core: structuring

In the context of the structuring process for the prospered inner core (PIC) of biopsy needles, the inner core composition comprises several materials. Specifically, the inner core was composed of fiberglass (FG), a matrix glue, a shrinking tube, and a hardened tip fabricated from either GR or NiTi. Three of FG with an average diameter of 0.245 mm were inserted inside the Polyester shrinking tube. Then, a heated fan shrank the tube to create a single FB. The FB was inserted and glued with Loctide 406 into a Polyimide (PI) tube with an average diameter of 0.65 mm. At the distal end of the PI tube, a tip of

3 mm was made out of a GR with a diameter of 0.6 mm for 6 needles. For the seventh needle, NiTi tip with a diameter of 0.5 mm was utilized and securely bonded to the PI tube using adhesive. Fig. 3.2(a) shows the longitudinal section structure of the needle core while Fig. 3.2(b) displays the cross section for the core. Two-needle tips NiTi and GR were sharpened using an angled abrasive paper to achieve a simple Chiba cut which is commonly used to puncture the abdominal cavity or internal organs [147]. The idea of using the NiTi tip as a marker in MRI during a scan. Simultaneously, investigating the performance of artifacts using GR for this particular material is being conducted. Fig. 3.2(c) illustrates the raw materials during the fabrication steps used to structure the core needle.

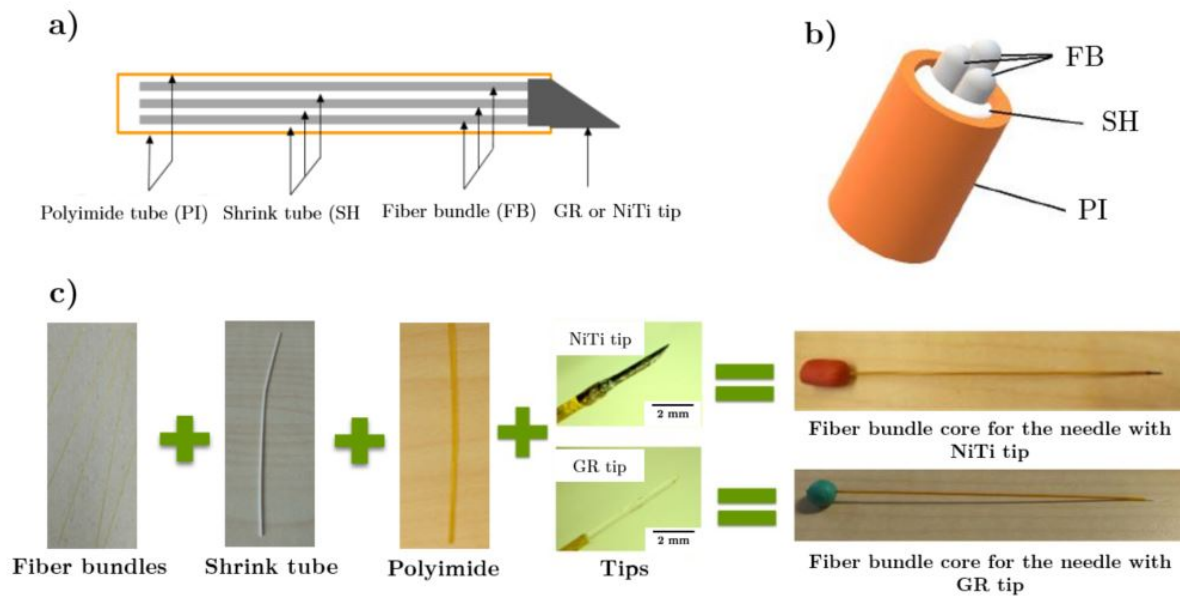


Figure 3.2: The proposed inner core (PIC) with the multi-layer concept for the needle: a) longitudinal section for the core needle with materials used for fabrication, b) CAD model for the constructed core needle showing the three FB with SH and PL, and c) raw materials used to structure the cores using two types of needle tips.

### 3.2.4 Outer hollow sheet

A group of polymeric outer sheet tubes was chosen considering MRI compatibility with two types of wall thicknesses 0.15 mm light wall (LW), 0.25 mm thin wall (TW) based on the American Wire Gauge (AWG). The dimensions of outer sheets are listed in Table 3.2. The NiTi outer sheet corresponds to the standard biopsy needle (SBN). While the remaining outer sheets stand for the sheets of the proposed biopsy needle (PBN). The objective of selecting different outer sheet tubes was to explore their mechanical performance for these non-metallic polymeric materials. The outer sheets were combined with the proposed inner core (PIC) resulting in seven primary prototypes of proposed biopsy needles (PBN) with



Table 3.2: Technical specifications for biopsy needle outer sheets, with an outer diameter (OD) of 1 mm, using two types of wall: thin wall (TW) and light wall (LW) measured all in millimeters (mm).

<i>Needle labeled</i>	<i>Outer sheet</i>	<i>Specifications</i>
1	PEEK	TW: 0.25 mm
2	PTFE AWG 21	TW: 0.25 mm
3	PTFE AWG 22	LW: 0.15 mm
NiTi	Standard	LW: 0.15 mm
4	FEP AWG 22	TW: 0.25 mm
5	PTFE AWG 20	LW: 0.15 mm
6	PTFE AWG 22	TW: 0.25 mm
7	PTFE AWG 21	LW: 0.15 mm

a length of 10 cm numbered from 1 to 7, as shown Fig. 3.3. The holder for the inner core and outer sheet was made using a 3D printer machine from Formlabs, Form 2 (USA).

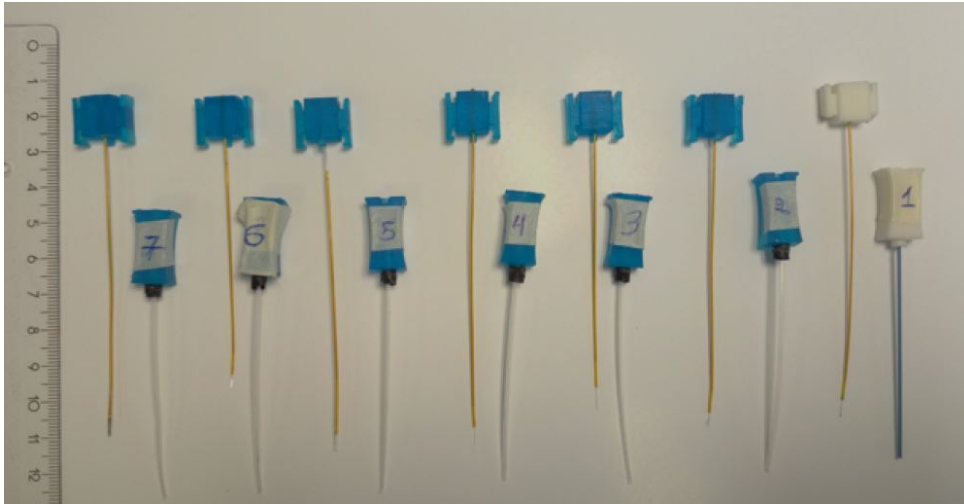


Figure 3.3: Seven non-metallic PBN used in this work, numbered from 1 to 7, each needle composed of 2 parts outer sheet and inner core.

### 3.2.5 Biopsy needle tips

In this work, the GR tips for the PBN were sharpened using an angled abrasive paper to achieve a simple Chiba cut, the same as the standard needle tip NiTi needle. Two types of tips used in the Fig. 3.4 (a) and (b) show the glass rod tips used for the six PBN while the NiTi tip was used for the seventh proposed needle when (c) and (d) display how the tips connected to the proposed inner cores.

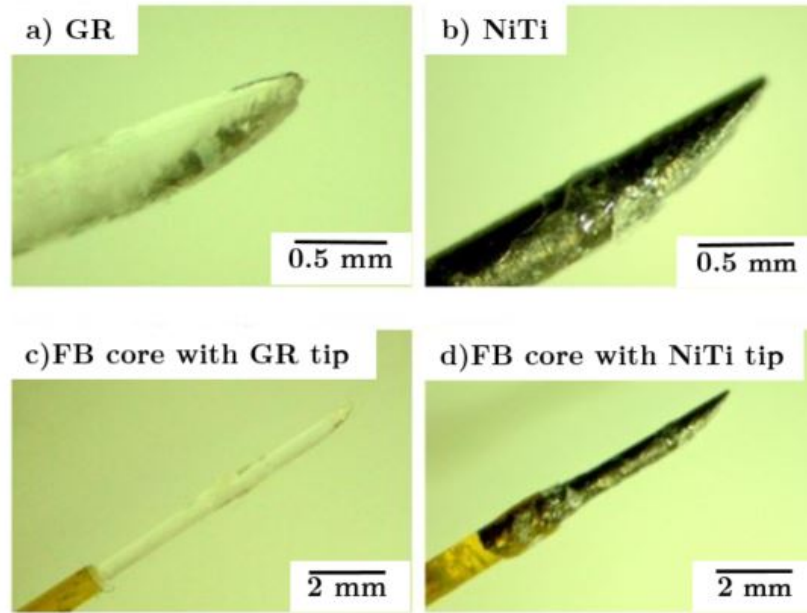


Figure 3.4: Microscopic images with different magnification scales for the proposed biopsy needle tips used for the needles: a) represent the GR tip with Chiba cut while b) is the NiTi tip. c) displayed the GR tip connected to the FB core and d) described the NiTi tip connected to the FB core.

### 3.3 Preparation of phantoms

Phantoms play an invaluable role in medical research, modeling tissue properties to evaluate clinical imaging approaches, therapeutic device performance, and medical procedures in a standardized test environment without risk to animal or human subjects [148, 149]. The most commonly used phantoms in guided biopsy needle research are gelatin phantoms. These phantoms exhibit properties closely resembling those of soft tissue, making them highly suitable for evaluating needle performance [150]. This study aimed to establish an experimental basis for evaluating the performance of biopsy needles in the presence of susceptibility artifacts during MRI-guided interventions. To this end, two types of phantoms were prepared to fix the needles during the experiments. The preparation process of the phantoms is described in detail in this section, including the materials used and the fabrication methods.

#### 3.3.1 Gelatin phantom

In this study, a custom MRI phantom was created using Paltin reinst 240 Bloom gelatin powder obtained from the Carl Roth GmbH (Germany) [148]. The phantom was prepared by mixing 300 grams of gelatin powder in 1,8 liters of hot water at 70°C. The mixture was allowed to cool to room temperature and left to set overnight. The following day, the standard NiTi needle and the PBNs were inserted into the phantom and labeled for subsequent MRI scanning.

### 3.3.2 Tissue-engineered phantom

In this study, I fabricated a three-dimensional tissue-engineered phantom designed to mimic in-vivo conditions. The purpose of this phantom was to evaluate the performance of biopsy needles and their impact on image artifacts. The 3D tumor model was created using tissue engineering techniques to mimic the complex properties of biological tissue. This approach provides a more clinically relevant MR imaging environment [151–153]. The preparation of this phantom was carried out under the supervision of Prof. Dr. rer. Heike Walles in the Core Facility Tissue Engineering at the Faculty for Process and Systems Engineering, Institute for Chemistry in OVGU. The methodological workflow was divided into four main steps, as shown in Fig. 3.5.

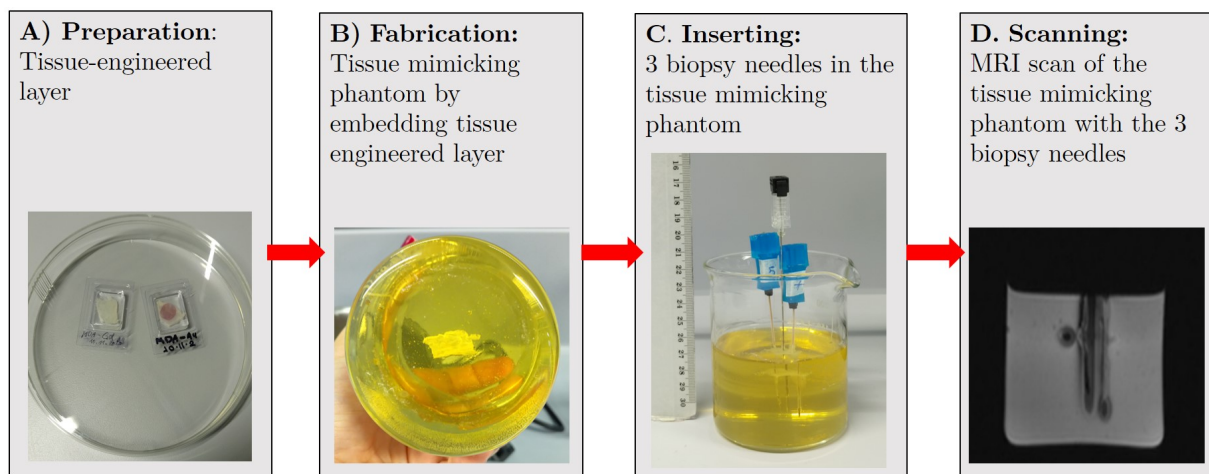


Figure 3.5: Workflow explains the steps used in 3D tissue-engineered phantom and MRI scan: A) preparation of the 3D tissue-engineered tumor model, B) fabrication of the gelatin phantom, then embedding the 3D tissue-engineered tumor model. C) inserting the biopsy needles and D) MRI scan of the three needles in the tissue-engineered phantom.

**A) Preparation:** The tumor model was prepared according to standardized protocols on the SISmuc platform acquired from a porcine intestine with dimensions of  $500\mu\text{m}$  thickness, 12 mm diameter [154] as presented in Fig. 3.6(A). The SISmuc scaffold was fixed in a cell crown between two metal rings seeded on the scaffold's luminal side. The cell crowns were placed in 12-well plates and covered with approx. 2.5 ml RPMI-1640 cell culture medium containing 10 % fetal calf serum (FCS). The cells were kept in an incubator with 5 %  $\text{CO}_2$  under high humidity at  $37^\circ\text{C}$ , and a medium exchange was done every 2–3 days.

**B) Fabrication:** After 14 days of tissue culturing, the tissue layer was ready for embedding in the gelatin powder consisting of 20% gelatin powder from Paltin type in a 0.5 glass cylinder as shown in Fig. 3.5(B).

**C) Inserting:** Subsequently, the three needles labeled as 1, 2, and NiTi were inserted in the tissue-embedded gelatin phantom as illustrated in Fig. 3.5(C). Needle 1 has a GR tip, while needle 2 has a NiTi tip to allow for a comparison of artifact ratios between the tips

after the MRI scan.

**D) Scanning:** Fig. 3.11 presents the three biopsy needles in the 3D tissue-engineered tumor phantom inside the MRI scan to evaluate the artifact's performance, as depicted in the MRI image shown in Fig. 3.5(D).

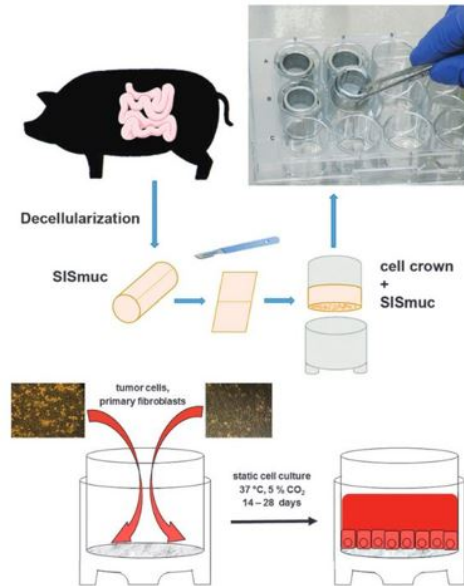


Figure 3.6: Schematic illustration for preparation of the tissue-engineered 3D tumor model (taken from [154]).

### 3.4 Image acquisition from gelatin and tissue-engineered phantoms

In this work, the MRI data acquisition for the biopsy needles was accomplished in two stages, first when the biopsy needles were in the gelatin phantom, and second when the biopsy needles were in the tissue-engineered phantom. The technical information for the used MRI scan parameters acquisition for each stage is explained in detail in this section.

#### 3.4.1 MRI scanner

The MRI measurements were carried out using a Siemens MAGNETOM Skyra 3T MRI scanner presented in Fig. 3.7 Research CAMPUS STIMULATE Otto-von-Guericke-Universität Magdeburg (OVGU), Germany. The technical specifications of the MRI scanner used for the measurements include a 70 cm bore size with an Open Bore Design, a magnet length of 163 cm, Zero Helium boil-off technology for helium consumption, and a combination of passive and active shimming for ensuring a uniform magnetic field. The machine also features XQ Gradients with a gradient strength of 45 millitesla per meter (mT/m) at 200 tesla per meter per second (T/m/s), which makes it ideally suited for image-guided interventions [155].



Figure 3.7: Photograph of the 3T MRI Siemens (Skyra), in Research Campus STIMULATE, Otto-von-Guericke-Universität Magdeburg (OVGU), Germany.

### 3.4.2 MRI scan parameters

The main purpose of this investigation was to assess the susceptibility artifacts generated by newly non-metallic PBNs in MRI scans. To achieve this goal, I utilized two sequence parameters during MRI intervention to compare and evaluate the performance of the proposed needles with the NiTi standard needle. The objective was to determine the optimal MRI sequence for visualizing a biopsy needle with fewer artifacts. Therefore, this section outlines the MRI scan procedures carried out using standard test parameters that are commonly used in biopsy needle imaging, as summarized in Table 3.3. In this study, MRI scans were performed using a group scan concept, where all needles were imaged together, and using an individual scan concept, where each needle was imaged separately. The purpose of this approach was to measure and quantify the artifacts present that differed when all needles were imaged together compared to when each needle was imaged alone.

Table 3.3: MRI imaging protocol used in this work for testing the non-metallic and standard NiTi needles.

MRI test parameters		
Sequence type	Gradient Echo (GE)-Flash	Spin Echo (SE)-Haste
Image weighting	T1	T1/T2
Slice thickness (mm)	7/3/2	7/3/2
Repetition time (ms)	144	600
Echo time (ms)	4.8	6
Slice resolution (mm)	1	1
Orientation	Transverse (tra), sagittal (sag), coronal (cor)	Transverse (tra)

### - MRI scan for core needles in gelatin phantom

As depicted in Fig. 3.8, three inner core needles were embedded in the gelatin phantom. PIC numbers (1, 3) and NiTi stand for the standard inner core (SIC). To perform a comprehensive assessment of image quality and susceptibility artifacts produced by the cores, a two-dimensional (2D) mode was used for two separate imaging sequences, each utilizing standardized test parameters. These protocols were carefully selected to enable meaningful comparisons between the two sequences and provide a thorough evaluation of the performance of the cores within the phantom:

- T1-weighted/GE/Flash/tra/2 mm
- T2-weighted/SE/Haste/tra/2 mm

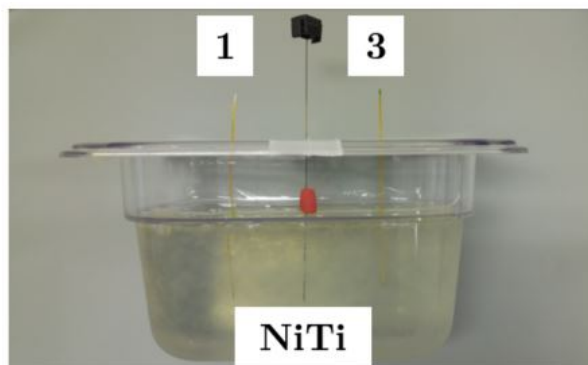


Figure 3.8: MRI gelatin phantom featuring three core needles: PIC 1 comprises a Polyimide tube containing three FG wires and a glass rod tip. NiTi represents the SIC needle, serving as a reference for comparison. Additionally, PIC 3 is composed of a Polyimide tube with three FG wires and a NiTi tip.

### - MRI scan of complete needles in gelatin phantom

Seven PBN non-metallic needles, consisting of an inner core and outer sheet, were tested alongside with standard NiTi needle by being inserted into a gelatin phantom. The needles and their placement within an MRI machine are illustrated in Fig. 3.9 and Fig. 3.10, respectively. The MRI test was conducted in 2D mode, utilizing the following parameters

- T1-weighted/GE/Flash/tra/7 mm
- T2-weighted/SE/Haste/tra/7 mm

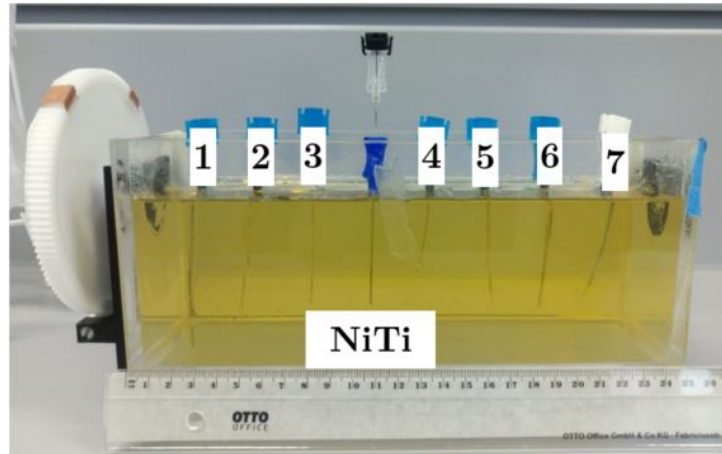


Figure 3.9: Gelatin phantom including seven PBNs numbered from 1 to 7 from (left to right) aligned in the same line along with the NiTi needle located in the middle to compare the artifacts performance during the MRI scan.

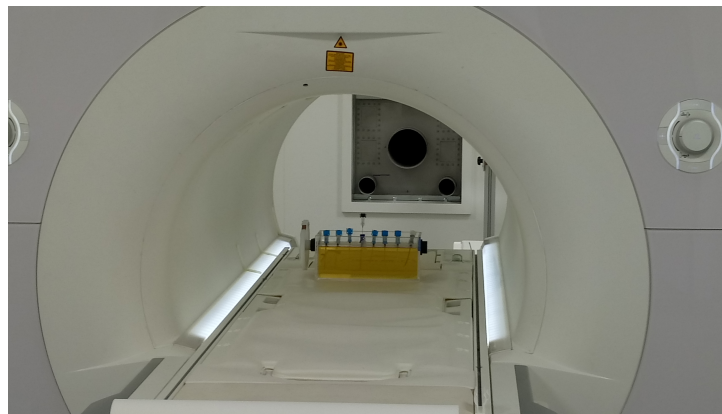


Figure 3.10: Seven non-metallic PBNs with NiTi needle inside the MRI scanner.

#### - MRI scan of rotated biopsy needles in gelatin phantom

MRI scans were conducted to evaluate the artifact orientation resulting from the rotation of biopsy needles in the axial position at four distinct rotational angles ( $0^\circ$ ,  $90^\circ$ ,  $180^\circ$ , and  $270^\circ$ ), as illustrated in Appendix Fig. A.2. In this context, a NiTi needle was represented as a standard needle (SN), and one proposed needle (PN) was impeded in the gelatin phantom with an insertion depth of 55 mm. Two indicators for angles were attached to the top of the phantom for each needle to guide the rotation process as displayed in Appendix Fig. A.2. The four angles were manually rotated during the MRI scan. For this analysis, the MRI test parameter for the rotation test was also performed in 2D mode with the following sequences:

- T1-weighted/GE/Flash/tra/2 mm
- T2-weighted/SE/Haste/tra/2 mm

### - MRI scan for biopsy needles in tissue-engineered phantom

To further evaluate the performance of non-metallic PBNs, three needles were selected: NiTi needles as SBN, and needle 1 and needle 3 from the PBNs. These needles were then subjected to conventional MRI scans, as depicted in Fig. 3.11. The needles were embedded within a 3D tissue-engineered phantom that had been prepared according to a protocol described in Fig. 3.5. The three needles were scanned in the MRI scanner using two modes to evaluate the presence of artifacts caused by the needles within the tissue-engineered layer. The artifact assessment steps are presented in Fig. 3.12. The utilization of a 3D imaging mode was employed for comparison against the conventional 2D mode in MRI. The 3D mode MRI can provide a more detailed view of the needle and surrounding tissue, however, the 3D mode requires more time to reconstruct the MR image [156]. The aim of this study was to demonstrate the robustness of the non-metallic materials used in the needles and compare them with the NiTi needle. Therefore, the MRI test parameters for this phantom followed the following sequence:

(1)- Group MRI scan for the three needles in 2D mode:

- T1-weighted/GE/Flash/tra/3 mm
- T1-weighted/SE/Haste/tra/3 mm

(2)- Individual MRI scan for each needle in 2D mode:-

- T1-weighted/GE/Flash/sag/3 mm
- T1-weighted/SE/Haste/sag/3 mm

(3)- Individual and group scan in 3D and 2D mode

- 3D/T1-weighted/GE/cor/0.5 mm
- 2D/T1-weighted/GE/Flash/sag/3 mm
- 2D/T1-weighted/SE/Haste/sag/3 mm

To quantify the artifacts of all biopsy needles, a numerical quantification step was performed on all MR images. MR images were imported into a DICOM viewer (RadiAnt DICOM, 3.2.2020), and the width and length directions for each needle were measured. This enabled the accurate quantification of artifact size and provided a reliable method for evaluating the performance of each biopsy needle in an MRI setting. The quantification results for the width and length direction for each needle represent as mean  $\bar{X}$  of three repetitive measurements of the data and its standard deviation (SD).





Figure 3.11: 3D tissue-engineered phantom with PBNs and SBN inside the MRI machine.

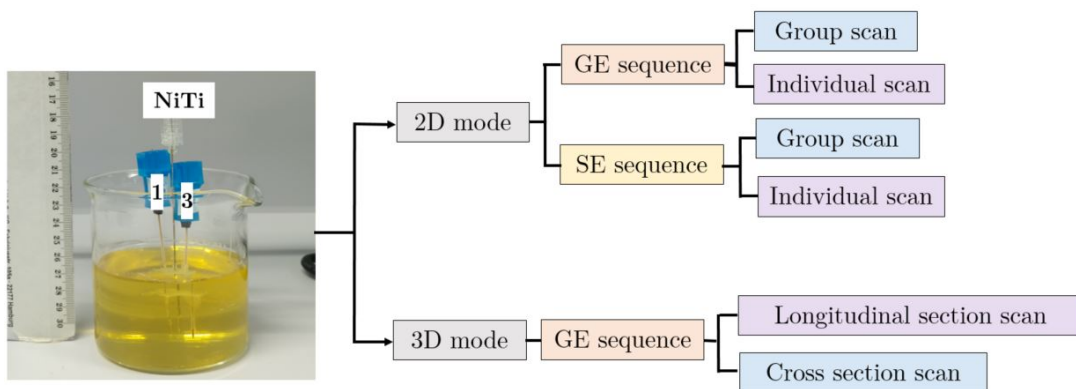


Figure 3.12: Schematic diagram presenting the MRI scanning steps for the three biopsy needles (1, NiTi, and 3) in tissue-engineered phantom using GE and SE sequences with 2D and 3D modes.

### 3.5 Approaches for evaluating the susceptibility artifacts for MRI

To evaluate the artifacts produced by non-metallic needles and their impact on MR image visualization, we utilized two approaches to detect and quantify susceptibility artifacts in the MR images: (1) an unsupervised machine learning approach using K-means and (2) a manual quantification approach. Fig. 3.13 presents the workflow quantification for the two approaches. As mentioned earlier, MRI data acquisition started by locating the seven fabricated non-metallic PBNs alongside the NiTi needle as SBN inside an acrylic glass filled with gelatin, then applying the MRI scan. The image acquisition parameters used in this work to mimic an MRI intervention for the T1-weighted sequence is a gradient-echo flash sequence, with a slice resolution of 1 mm, a slice thickness of 7 mm, a pixel bandwidth of 230, and a field of view (FOV) of 244\*244 mm. The needles in the resulting MR image were labeled from left to right as L1 to L8 to facilitate the artifact's quantification process. Moreover, all the proposed needles have a glass rod tip, except the needle which L1 has a NiTi tip, as shown in Fig. 4.13 as a small circular artifact. The quantification steps are explained in detail in the following sections.

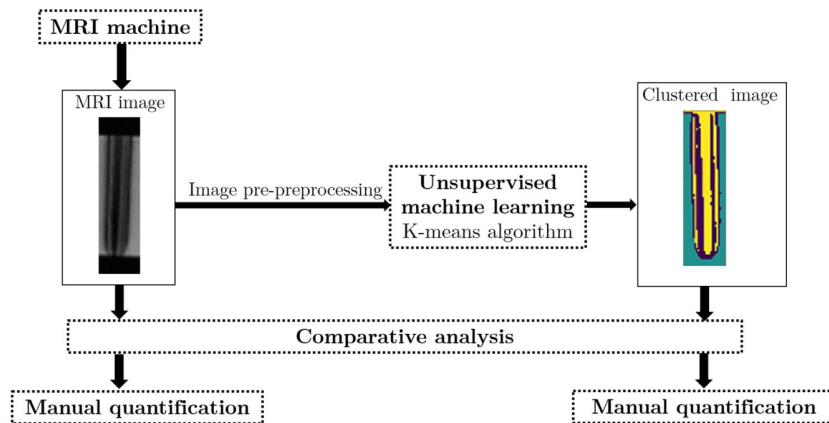


Figure 3.13: A graphical flow chart presenting the two approaches used to quantify the artifacts in the MR images of PBNs.

#### 3.5.1 Manual quantification

In this step, the quantification of artifacts was performed by importing the MR images into a DICOM viewer (RadiAnt DICOM, 2020.2.3). The artifacts were manually evaluated by measuring the width and length of each needle. The measurements were based on uncertainty assessment for the eight needles representing the mean  $\bar{X}$  of three repetitive measurements of the data and its standard deviation (SD) [118]. The manual quantification of needle width and length is detailed in Fig. 3.14.

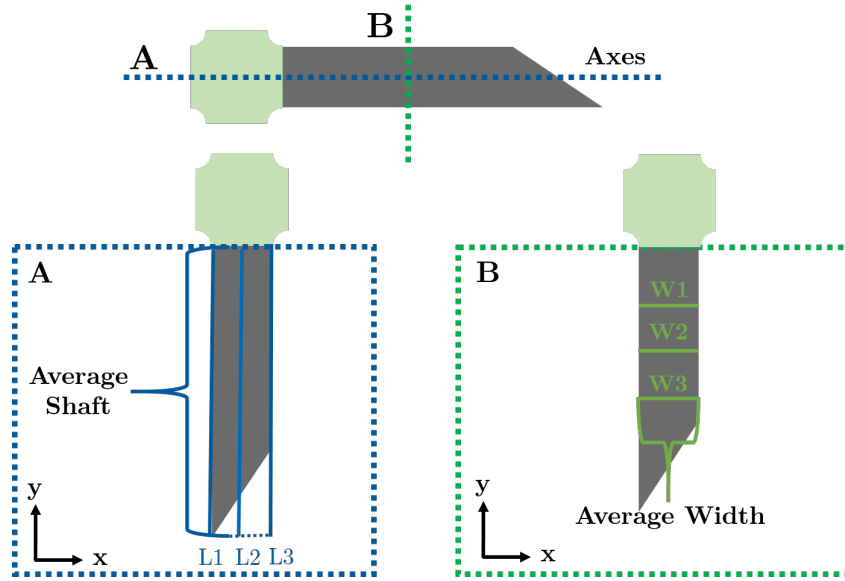


Figure 3.14: Graphical representation of a manual quantification method used to measure biopsy needle shaft and diameter.

### 3.5.2 Machine learning K-means quantification

Before applying the K-means algorithm, the MR images were subjected to a preprocessing step. The selected MRI image was taken from an MRI group scan presented in Fig. 3.15. The PBNs were labeled as (L1, L2, L3, L5, L6, L7, and L8), while the NiTi needle was labeled as (L4). The needle images were converted to the NIFTI format and then clustered based on pixel intensity [157]. Subsequently, a cropping step was applied to each needle before the K-means clustering. The clustering was computed by using the `opencv` and `scikit-learn` libraries in Python. For the dataset, random cluster centroid initialization has been used, wherein the centroids were further refined over several iterations to obtain optimal clusters. Additionally, the K-means clustering includes a parameter to validate the quality of the cluster, which is called silhouette coefficient [158]. Based on literature [159], [160] the silhouette score can be utilized to measure the goodness of clustering for a different number of clusters ( $K$ ) ranging from 3 to 7 in this study. Similar to the manual quantification approach described earlier, the width and length measurements were repeated for the clustered images to quantify the artifact appearance of the automatic approach. Fig. 3.16 displays schematic details for data processing in K-means clustering to detect and quantify the needle artifacts from the MR images.

## 3.6 Mechanical testing for non-metallic biopsy needles

This section provides a description of the mechanical test in two aspects: experimental setup and modeling setup for the biopsy needles. The idea was to characterize and optimize the mechanical performance and the dimensions of the proposed non-metallic

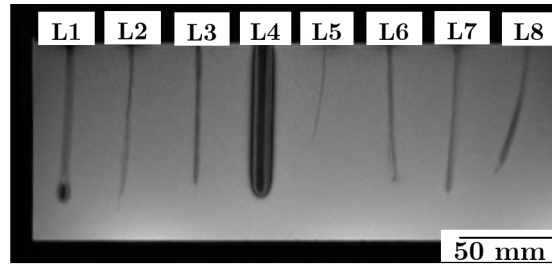


Figure 3.15: MRI image used to apply K-means algorithm to the biopsy needles

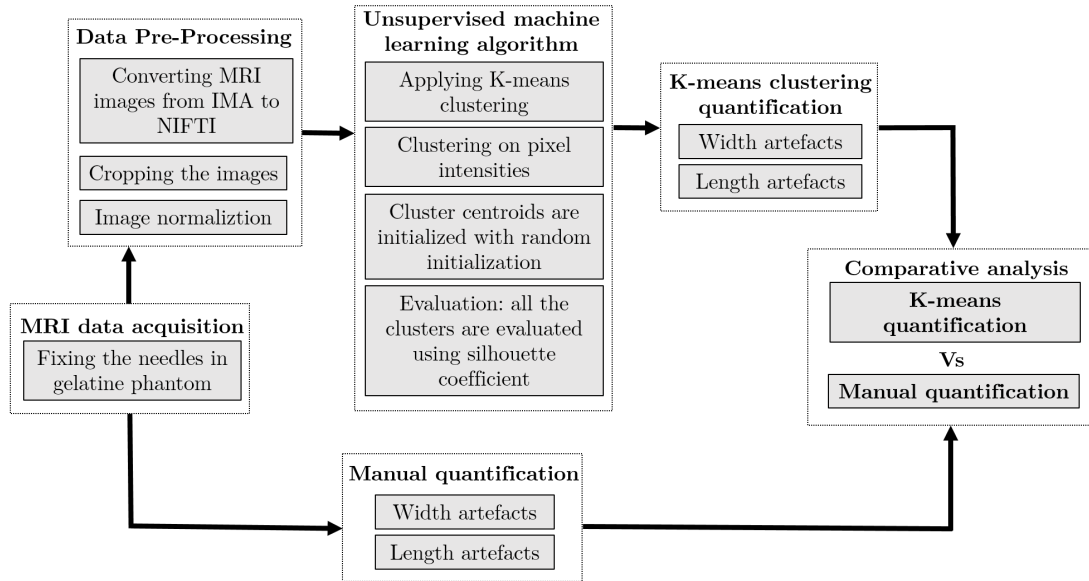


Figure 3.16: Comprehensive workflow illustrating the unsupervised machine learning and manual approaches proposed to quantify susceptibility artifacts of biopsy needles.

biopsy needles. Therefore, the experimental mechanical setup was accomplished through a custom-made bending setup. While the modeling design was executed by finite element analysis.

### 3.6.1 Experimental setup: Zwick Roell machine

The Zwick Roell machine is an effective tool for rapidly generating significant amounts of data on tensile strength and fatigue measurements. In this study, the mechanical properties of biopsy needles were evaluated using a Zwick Roell machine (Z0.5 model, Ulm, Germany) with a custom-made practical setup for a two-point bending test, as depicted in Fig. 3.17. The biopsy needles were placed horizontally on a fixation block with an overhang to evaluate stiffness. Then needles were bended applying a deformation of 2 mm at a 15 mm distance from the fixation point. The bending force was measured using the test protocol according to DIN EN ISO 626.03/2002 determination of stiffness of stainless steel needle tubing [161]. To assess the uncertainty in the measurements of

the mechanical properties of the biopsy needles, a threefold repetition of the two-point bending test was performed for each biopsy needle sample. The detailed results of this test are provided in Chapter 4. This approach is commonly used in mechanical testing to minimize the effects of variability and measurement errors such as (instrumentation errors, human errors, environmental conditions, and sample variability) and to obtain a more accurate measurement of the mechanical properties of materials. Test specifications parameter for Zwick Roell machine is shown in the Table 3.4.

Table 3.4: Bending test parameters used for the Zwick Roell machine.

sTest Parameter	Values
Speed	60 mm/min
Deformation	2 mm
Bending Length	10 mm
Pusher position	attached to the needle surface

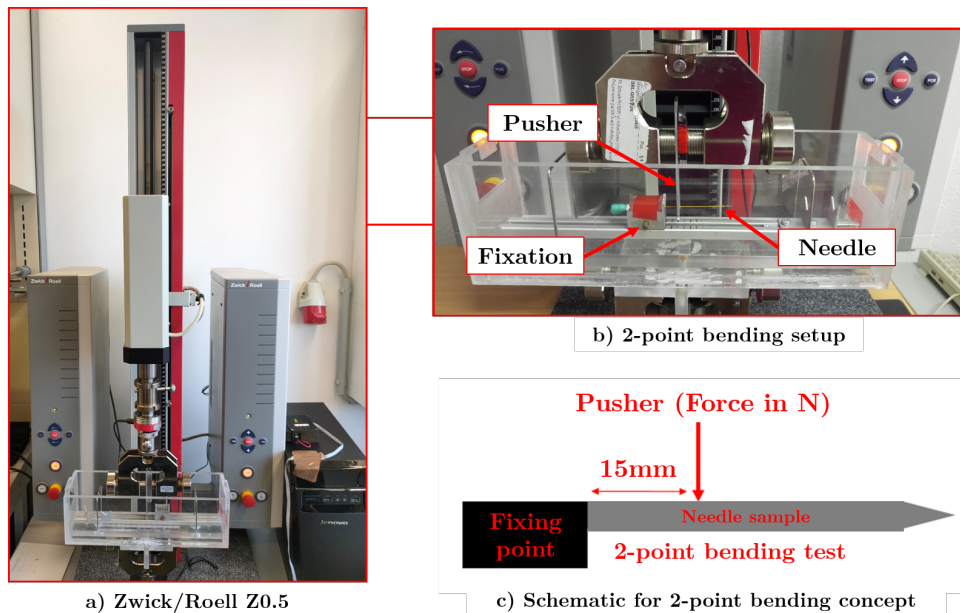


Figure 3.17: Mechanical experimental setup: a) Zwick/Roell machine used to employ mechanical tests to characterize the properties of the samples, b) custom-made setup used to perform bending test for the non-metallic needles attached to the Zwick Roell machine, c) sketch for the 2-point bending test concept showing the fixation point and direction of pusher toward the needle sample.

### 3.6.2 Modeling setup: Finite element analysis modeling

The experimental results obtained from the bending setup from the Zwick Roell machine for the biopsy needle prototypes, as shown in Fig. 4.16, suggest the requirement of further analysis and optimization to achieve an acceptable solution, particularly when compared to the performance of the NiTi needle. To address this issue, I developed a computational

model using FEA in ANSYS software from the Academic Teaching Mechanical version (R2, 2020) to test the mechanical properties and improve the functionality of the non-metallic MRI biopsy needle. The use of FEA allowed for a thorough examination of the biopsy needles' mechanical properties, enabling a more precise evaluation of their strength, stiffness, and durability. To execute the finite element simulation of the geometry, ANSYS software was used, which requires the specification of geometry, material properties, boundary conditions, and mesh with high precision during the input phase. Any deviation from the specified parameters can lead to unfavorable results [162–166]. The mesh element size is a critical parameter that significantly affects simulation outcomes. When the mesh element size is decreased, accuracy increases, but this also leads to an increase in simulation time. The meshing strategy plays a pivotal role in determining simulation accuracy and duration. A mesh element, a small geometric shape such as a triangle, quadrilateral, tetrahedron, or hexahedron, discretizes the overall structure geometry into simpler subdomains. These elements are interconnected at nodes and defined based on the material properties and structure geometry. Each element generates a local stiffness matrix, characterizing its rigidity. On the other hand, the global stiffness matrix, assembled from contributions of all individual mesh elements, represents the combined stiffness and interactions of the entire structure. Consequently, FEA with ANSYS involves dividing the structure into mesh elements, each having its local stiffness matrix. These local stiffness matrices are merged to create the global stiffness matrix, governing the overall structure behavior during simulation. The meshing strategy is integral in attaining accurate and efficient simulation results. Initially, ANSYS applied linear elements throughout the model. As the analysis progressed, more complex element types might have been adopted to achieve greater accuracy, especially when capturing intricate behaviors in specific areas. To comprehend needle behavior, the model is subjected to defined boundary conditions, restricting degrees of freedom. Toward the conclusion of the analysis, a global stiffness matrix is generated, enabling the solution of a system of equations for obtaining final results [167]. The meshing approach additionally validates simulations and quantifies uncertainties. The execution steps for FEA are illustrated as a flow chart in Fig. 3.18.

The simulation steps were executed in the following steps:-

1. Designing the models in 3D AutoCAD software to create biopsy needle structures with the required mechanical test setups.
2. Setting the mechanical properties of the materials used with test parameters to evaluate the performance and validate the prototypes by finite element analysis in ANSYS simulation.
3. Applying the mechanical bending test in the simulation environment with the required boundary conditions to find the best-proposed biopsy needle performance corresponding to the standard biopsy needle.

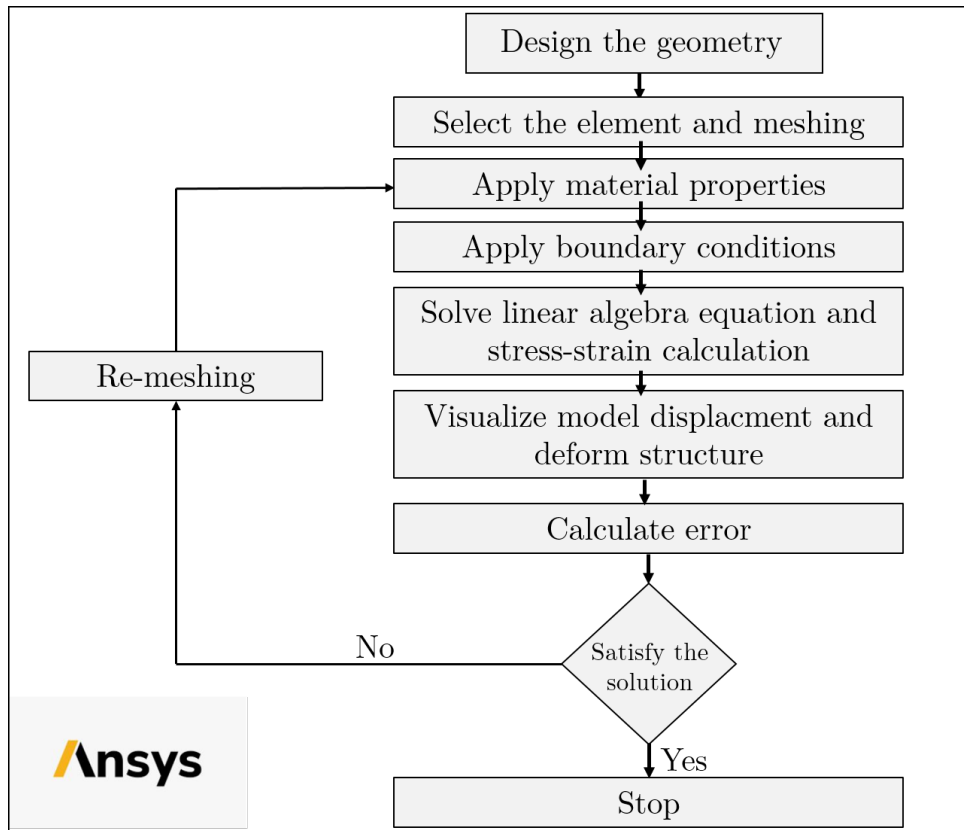


Figure 3.18: Workflow process for the FEA containing pre-processing, solver, and post-processing.

4. Employing fatigue or breaking point analysis for the needles by calculating the safety factor to find the maximum deflection based on the mechanical properties range.
5. Validating the results of simulation for the non-metallic needles using critical parameters.

The computational modeling using FEA is performed in two distinct stages, denoted as Design I and Design II, as depicted in Fig. 3.19. This two-stage approach is motivated by the structure of the biopsy needle, comprising an inner core and an outer sheet. In Design I, the focus lies on optimizing the inner core of the biopsy needle, while in Design II, the emphasis shifts to the design and optimization of the outer sheet. Consequently, to enhance the performance of the non-metallic PIC of the biopsy needle, mechanical bending tests were conducted. As discussed in this chapter, section 3.2.3, the process of the prospered inner core (PIC) was utilized for the inner core. Expanding upon this, Finite Element Analysis (FEA) was introduced to analyze PIC<sub>i</sub> with varying diameters. The subscript 'i' (i) denoted different diameters, considering four distinct designs referred to as proposed inner cores: PIC 1, PIC 2, PIC 3, and PIC 4. These inner cores were carefully designed with incremental diameters and subsequently compared to the standard NiTi inner core. The non-metallic inner core that was found to work mechanically closer to the standard inner core NiTi was selected as the best proposed inner core. While

Design II aimed to find the best non-metallic biopsy needle. As well, four proposed biopsy needles with different diameters for the outer sheet and materials were constructed and compared to the standard biopsy needle. The selected PIC from Design I was used as the core to construct the four non-metallic outer sheets of the biopsy needles in Design II. As mentioned in section 3.2.4, the four non-metallic outer sheets were referred to as PBNs numbered 1, 2, 3, and 4, while the NiTi needle was referred to as SBN. The PBN that behaved mechanically closer to the SBN was selected as the best non-metallic PBN for MRI-guided interventional procedures.

The modeling process was carried out in two distinct steps. Firstly, the design was created using AutoCAD software (2021). Secondly, ANSYS, was employed for conducting simulations. In this second step, the geometric assignment, meshing, and static structural analysis were performed. The proposed materials used during the initial stage of the fabrication process for biopsy needles, as well as in the subsequent mechanical testing through experimental setup along with its parameters were applied and executed in FEA. In the mechanical characterization, it should be noted that ultimate tensile strength is the maximum stress that material can withstand while being stretched or pulled before breaking [168]. Therefore, the equivalent test in FEA is the stress vs. displacement for the core needle in Design I and then for the biopsy needle in Design II.

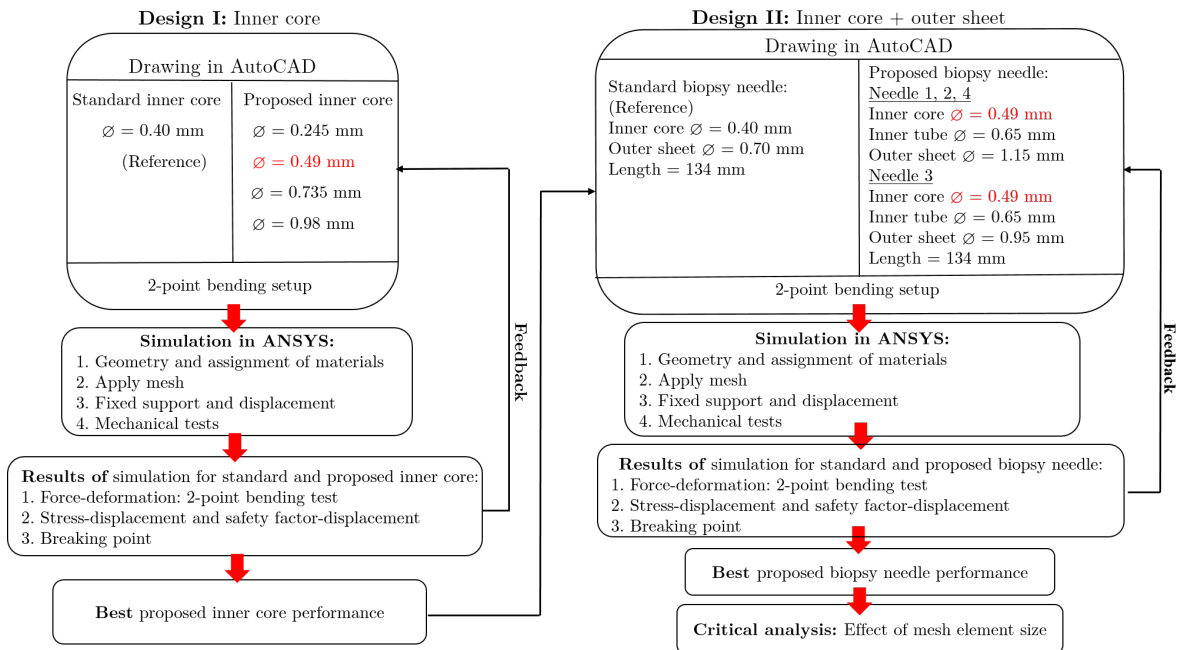


Figure 3.19: Workflow for the proposed methodology used in FEA to optimize the design and the performance of the non-metallic PBNs through executing two design steps: the first stage, referred to as Design I, focuses on optimizing the dimensions of the proposed inner core, while the second stage, known as Design II, is used to optimize the dimensions of the entire proposed biopsy needle.



An important test parameter used in this work during the simulation implementation is the Factor of Safety (FoS), as shown in equation 3.1. The FoS is calculated in ANSYS and serves to inform the user about the material's fatigue analysis and its potential for breakdown [169]. An important test parameter used in this work during the simulation implementation, defined as the Factor of Safety (FoS) as shown in equation 3.1 is calculated in ANSYS, which informs the user of the fatigue analysis or breakdown of the material [169]. FoS is the ratio between the ultimate tensile strength and the equivalent stress. ultimate tensile strength is a material property used to describe the maximum stress a material can withstand before it fails in tension. It is a critical mechanical property for evaluating the structural integrity and safety of engineering components. While equivalent von - stress is a scalar value used to represent the combined effect of different types of stress on a material element. FoS values are typically within the range of 0 to 15, which can help engineers assess the safety of their designs. Understanding the FoS values is crucial to identify whether a material or structure can withstand applied loads without failure. When the FoS value is between 0 and 1, it signifies that the equivalent stress has exceeded the ultimate tensile strength of the material. This situation indicates a critical safety concern, as the material is prone to failure and breakage under the applied load. On the other hand, FoS values between 1 and 15 indicate a safer scenario, as the equivalent stress is below the ultimate tensile strength. In this range, the material has a sufficient safety margin, and it is less likely to fail due to applied loads [170] [171]. A FoS value below 1 suggests that the design may not be safe and requires further modifications, while a value between 1 and 15 indicates a design with an acceptable level of safety, as the stress levels are below the material's ultimate tensile strength. In this study, I applied the factor of safety in both Design I and Design II. This parameter plays a significant role in assessing the structural integrity and safety of the designs.

$$\text{Factor of Safety (FoS)} = \frac{\text{Ultimate tensile strength}}{\text{Equivalent von - stress}} \quad (3.1)$$

To validate the results of the final prototype, ANSYS was used to perform an automatic mesh convergence test. Meshing is a critical step in FEA that involves dividing the geometry into a set of finite elements called nodes and elements [172]. The mesh ensures the accuracy and reliability of results. The accuracy of the FEA results is heavily dependent on the size and quality of the mesh used in the simulation [173]. It is essential to generate a mesh that has a sufficient element size, which increases the number of nodes and elements in the model. As the mesh element size decreases, the number of nodes and elements generated increases, resulting in a more accurate representation of the physical system being analyzed. [172, 174, 175]. The following section presents the computational modeling of Design I first then Design II in FEA consecutively.

- **3D model in AutoCAD for Design I**

Three-dimensional (3D) drawing designs were created for both the standard inner core, made of NiTi, and four proposed inner cores, each consisting of three main structures: the inner core, tip, and inner core holder as presented in Fig. 3.20. The designs included varying diameters to evaluate mechanical performance in comparison to the NiTi core. All sketches were initially created in the '.dwg' format, which stands for 'Drawing' and is a file format used by AutoCAD. Later, these sketches were converted to the '.sat' format, which stands for 'Standard ACIS Text', SAT files are used to represent 3D solid models and can store data related to the geometry, topology, and other attributes of the model. SAT files are commonly used for interoperability between CAD and FEA software, enabling simulation in ANSYS. Before conducting a simulation in ANSYS, the model was imported, and the materials for the FEA were specified as follows: NiTi was chosen for the NiTi core, Fiberglass (FG) was selected for the PIC with 4 different diameters, and Stainless Steel (SS) was used for the structural support to fix the core in place for performing the test. The dimensions used to sketch for both the NiTi core and PICs are shown in Table 3.5. The total length of the standard and proposed inner cores is 133.23 mm when all parts are assembled.

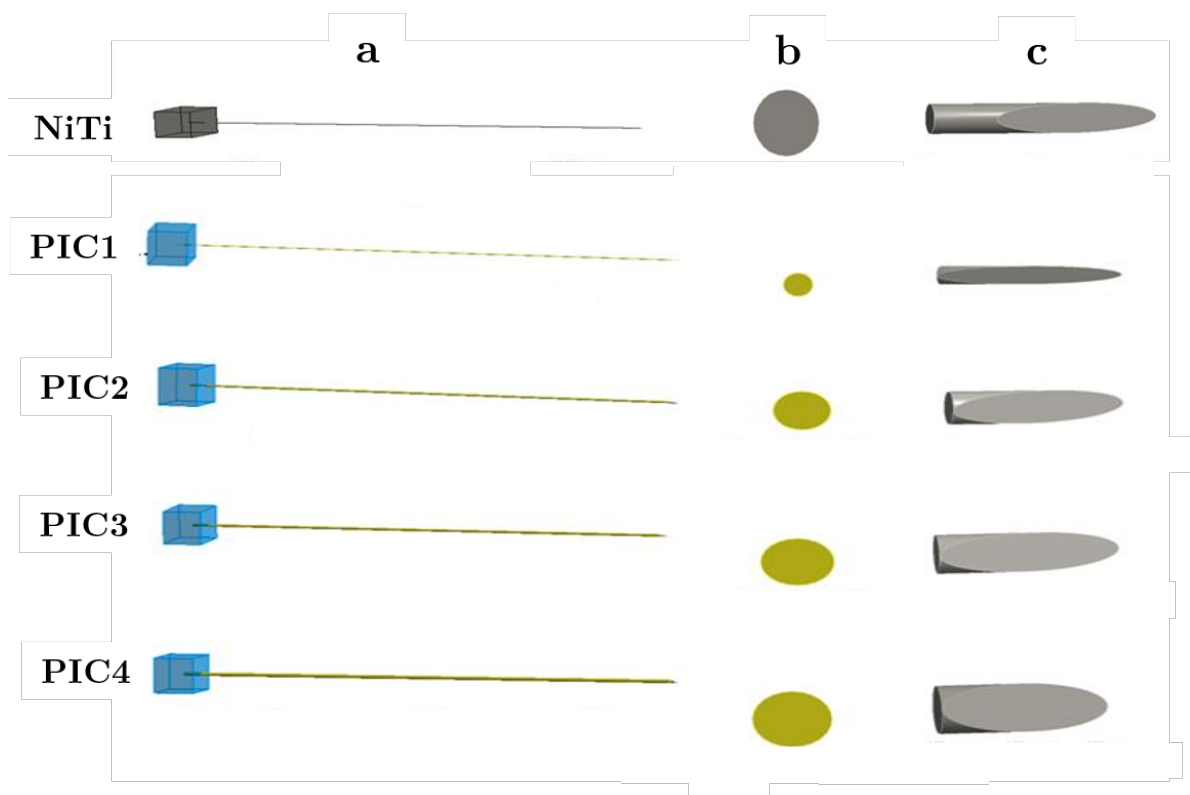


Figure 3.20: AutoCAD design structure for NiTi and PICs made from FG: (a) complete inner core structure, (b) cross-section for the inner core, and (c) inner core tip.

Table 3.5: Dimensions used in FEA simulation for the standard inner core and proposed inner cores.

Inner core	Core shaft dimensions		Holder dimensions			Tip dimensions		
	Length (mm)	Diameter (mm)	Length (mm)	Width (mm)	Height (mm)	Length (mm)	Diameter (mm)	Angle (°)
NiTi	125	0.40	10	15	10	2.23	0.40	13
PIC 1	125	0.245	10	15	10	2.23	0.245	6
PIC 2	125	0.49	10	15	10	2.23	0.49	12
PIC 3	125	0.735	10	15	10	2.23	0.735	18
PIC 4	125	0.98	10	15	10	2.23	0.98	24

While the dimensions to design the 3D parts for the mechanical 2-point bending setup were taken from the measurements of the dimensions of the experimental bending setup presented in Appendix Fig. A.3 and displayed as a 3D model from AutoCAD in Fig. 3.21 with the following dimensions for the pusher (length 20 mm×width 2 mm×height 97 mm) and for the fixation (length 25 mm×width 35 mm×height 25 mm). Subsequently, the complete setup used for the needles with different diameters is illustrated in Fig. 3.22.

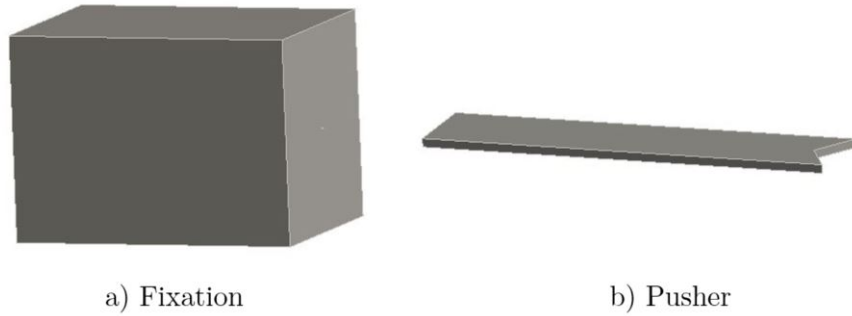


Figure 3.21: A 3D AutoCAD configuration used for 2-point mechanical bending setup parts a) fixation, b) pusher.

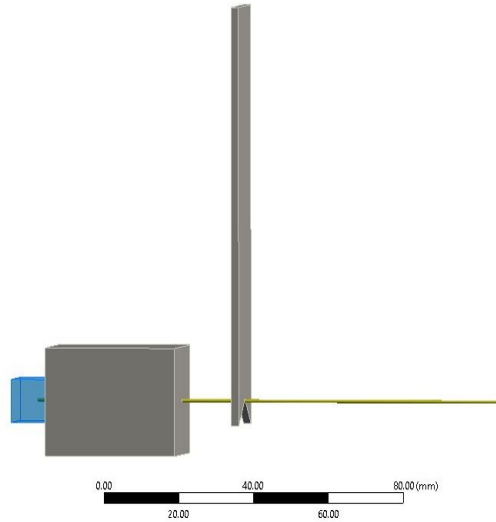


Figure 3.22: 3D modeling design of the mechanical bending setup used to test the mechanical properties of the cores in Design I. The setup was used to test cores with different diameters, including NiTi (0.4 mm), PIC1 (0.245 mm), PIC2 (0.49 mm), PIC3 (0.735 mm), and PIC4 (0.98 mm).

- **Simulation in ANSYS for Design I**

The 3D AutoCAD sketch was imported into ANSYS Workbench. The simulation steps for Design I were executed as follows:

1. **Geometry and properties of materials used:** The initial step in conducting an FEA using ANSYS simulation involved assigning the material properties to each part used in the model. The mechanical specifications of the materials used in needle design and bending setup were presented in Table 3.6. In our study, I assigned the bending setup parts as SS, the standard core as NiTi, and the proposed inner cores as FG.

Table 3.6: Mechanical properties of the materials used in the FEA simulation in Design I [162–166, 176–181].

Mechanical properties	Nitinol (NiTi)	Fiberglass (FG)	Structural steel (SS)
Young's modulus (GPa)	41 - 75	51.7 - 86.9	200
Poisson's ratio	0.3	0.21	0.3
Bulk modulus (GPa)	34.2 - 62.5	29.7 - 49.9	166.7
Shear modulus (GPa)	15.8 - 28.8	21.4 - 35.9	76.9
Density (g/cc)	6.5	2.11 - 2.46	7.85
Ultimate tensile strength (MPa)	1450	2415 - 4890	460

2. **Meshing and its parameters:** Generating a mesh composed of discrete elements that are connected by nodes to represent the geometry of the model. In the 2-point bending test used in this study, the regions of interest were the face where the inner core emerged from the fixation and the faces where

the pusher came into contact with the inner core. FEA simulations include three essential parameters: element size, resolution, and refinement. Element size refers to the size of each element in the mesh, with smaller elements resulting in higher mesh density and a more accurate representation of the geometry. When the mesh element size is decreased, accuracy increases, but this also leads to an increase in simulation time. Resolution determines the number of elements in the mesh, with a higher resolution resulting in a finer mesh, allowing for more detailed representation and improved analysis accuracy. Mesh refinement involves concentrating higher mesh density in specific regions of interest, capturing critical details, and obtaining accurate results while using a coarser mesh in less critical areas to optimize computational resources. By carefully optimizing these mesh parameters, engineers can strike a balance between accuracy and computational efficiency, ensuring reliable and meaningful results in FEA simulations. The resolution is typically specified as the number of elements per unit length, area, or volume, depending on the type of mesh being used. Refinement controls the level of mesh refinement in regions of interest. It is usually applied in areas where there are rapid changes in geometry or where high stresses are expected. A higher refinement level results in more elements being used in these regions, leading to a more accurate solution. Adjusting and selecting the appropriate mesh parameters is essential to achieve reliable and precise outcomes from the FEA analysis. In this study, the mesh parameters used for the 2-point bending test were specified as element size = 6 mm, resolution = 3, and refinement = 3. Despite attempts to further reduce the mesh size, it was not feasible to do so due to inherent limitations within the ANSYS software version. It is important to note that the mesh element size had to be maintained at a minimum value of 6 mm to ensure accurate simulations within these software constraints. However, to ensure the accuracy of the obtained results, the selected mesh element sizes were thoroughly validated and their impact on the study outcomes was discussed in the results and discussion section as uncertainty analysis. Table 3.7 presents the number of nodes and elements that are generated during the simulation for the standard and the proposed inner cores. Nodes and elements for the mechanical bending setup are illustrated in Table 3.8. The mesh behavior of all modeled core designs is depicted and presented in Fig. 3.23.

Table 3.7: Number of nodes and elements for NiTi core and PICs used in the ANSYS simulation for the bending setup.

	Standard inner core	Proposed inner cores			
	NiTi	PIC 1	PIC 2	PIC 3	PIC 4
Nodes	87360	117413	77758	64275	58778
Elements	52971	69493	47435	40229	37358

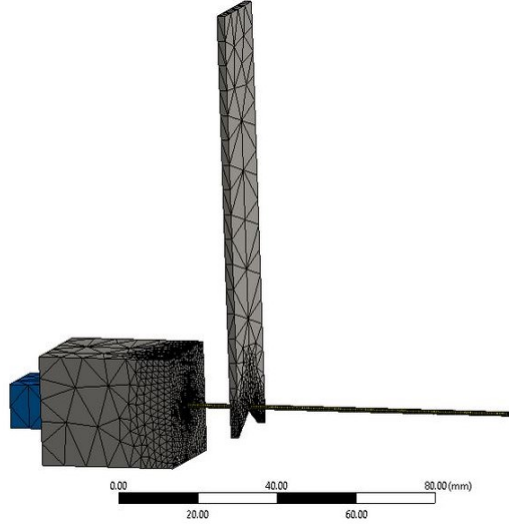


Figure 3.23: Meshing generation status for the bending setup and core needle.

3. **Static structural analysis:** According to the mechanical 2-point bending setup, the boundary conditions required that one side of the setup, including the standard inner core and proposed inner cores, be fixed in place (fixed support), while the other side remained free to move and underwent displacement. The fixed support was achieved by securing the faces of the inner core holder and the fixation, totaling nine faces, preventing any movement of the standard and proposed inner cores on that side. On the opposite side, all faces of the pusher, including the standard and proposed inner cores, were subjected to displacement in the direction of bending, amounting to four faces. The mechanical setup for both the standard and proposed inner cores was illustrated with fixed support and displacement boundary conditions in Fig. 3.24.

Table 3.8: Number of nodes and elements for SBN and PBNs in mechanical setup.

		Nodes	Elements
Standard biopsy needle	SBN	114961	54573
Proposed biopsy needle	PBN 1	184674	66987
	PBN 2	184674	66987
	PBN 3	208001	71303
	PBN 4	184674	66987

4. **Force reaction vs. displacement:** In the bending test simulation of Design I cores using ANSYS, the pusher displacement was set to 2 mm. The force was indirectly applied through a pusher displacement of 2 mm. The pusher represented the mechanism that applied the bending load to the cores' needles. As the pusher was displaced by 2 mm, it induced bending deformation in the cores' needles. This deformation generated internal forces, known as reaction forces, within the cores, resisting the applied displacement. To measure these reaction forces, a force reaction probe was used, which recorded the force values in Newtons (N) exerted by the inner core structures in response to the bending load. The pusher displacement for the bending test was set to 2 mm for the cores needles in Design I under ANSYS simulation. In this context, to check the variation for the force reaction results compared to the pusher displacement, minimum and maximum values of material mechanical properties were used in the ANSYS simulation from Table 3.6.
5. **Stress vs. displacement:** After the force reaction displacement test for the core needles, further mechanical simulation tests by FEA were applied to optimize the performance of the non-metallic biopsy needles. Therefore, a stress test was simulated to check if the stress crosses the ultimate tensile strength of the standard inner and the best proposed inner cores from the force reaction vs. displacement test. The ultimate tensile strength of the standard inner core material NiTi is 1450 MPa, as shown in Table 3.6. On the other hand, the proposed inner cores made of fiberglass material have a range of ultimate tensile strength values, ranging from 2415 MPa to 4890 MPa, as also shown in Table 3.6. Therefore, based on the results, there is conclusive evidence that the stress values have not crossed the ultimate tensile strength limit when the pusher displacement was 2 mm for both minimum and maximum values of mechanical material properties. For this reason, pusher displacement must be increased to find the breaking point in the standard inner core and proposed inner cores.
6. **Breaking point (safety factor vs. displacement):** As noted in the previous point, the stress vs. displacement test indicated that increasing the pusher displacement beyond 2 mm up to 10 mm was necessary to assess the breaking point or fatigue of both the standard and optimal non-metallic inner cores. This evaluation will incorporate the minimum and maximum range values of mechanical material properties to ensure accurate and comprehensive analysis. In the Design II stage, the simulation process commenced by using the optimal PIC diameter identified from Design I to develop a new coaxial configuration for the biopsy needles. As the study required a biopsy needle with a multi-layer concept, the single-core structure in Design I was replaced with three

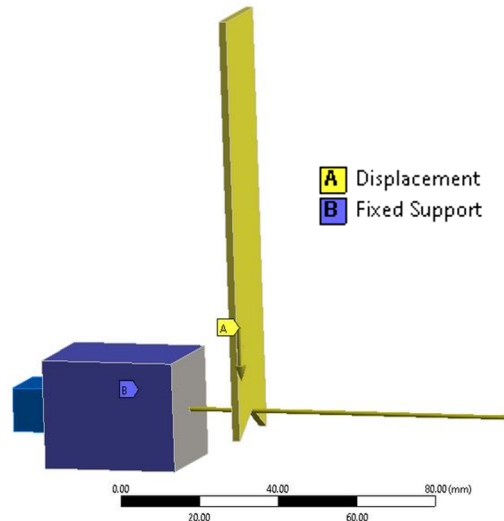


Figure 3.24: Static structural analysis performed using FEA on the fixed support in blue (referred to as B) and the displacement in yellow (referred to as A) for the inner cores. The fixed support is represented by nine faces, while the displacement is represented by seven faces.

core structures, each supporting a 0.245 mm diameter for the fiber bundle. Combining the diameters of the three cores resulted in an inner diameter of 0.49 mm. The proposed design, shown in Fig. 3.25, was accurately represented by applying four outer hollow sheets with varying diameters and different materials in the biopsy needle. Subsequently, a 3D model of four non-metallic biopsy needles was developed in AutoCAD, incorporating the best inner core diameter from Design I. The simulation process in ANSYS for Design I was replicated in Design II, encompassing the essential steps such as static structural analysis, mechanical bending test, and meshing. The detailed procedures for these simulations have been included in the Appendix for reference Fig.B.1, Fig.B.2, Fig.B.3, and Fig.B.4.

In Design II, I employed an advanced simulation methodology, refining it by adjusting additional parameters to significantly enhance result accuracy. The simulation process was precisely described, including the precise materials assignment. The focus was on modeling both standard biopsy needles (SBN) and the innovative proposed biopsy needles (PBN) are illustrated in the Appendix Table B.1 display the material properties used for SBN and PBN, respectively. The standard and non-metallic biopsy needles were designed using the dimensions represented in Table 3.10 and Table 3.11. For the non-metallic needles, the proposed outer hollow sheet materials included PEEK, PTFE, and FEP, while PI was assigned to the core needles as the middle hollow sheet layer. The mechanical properties of the materials used in Design II are listed in Table 3.9. The mesh parameters used in Design I were also applied in Design II, and the



nodes and elements were generated as shown in Appendix Fig. B.2.

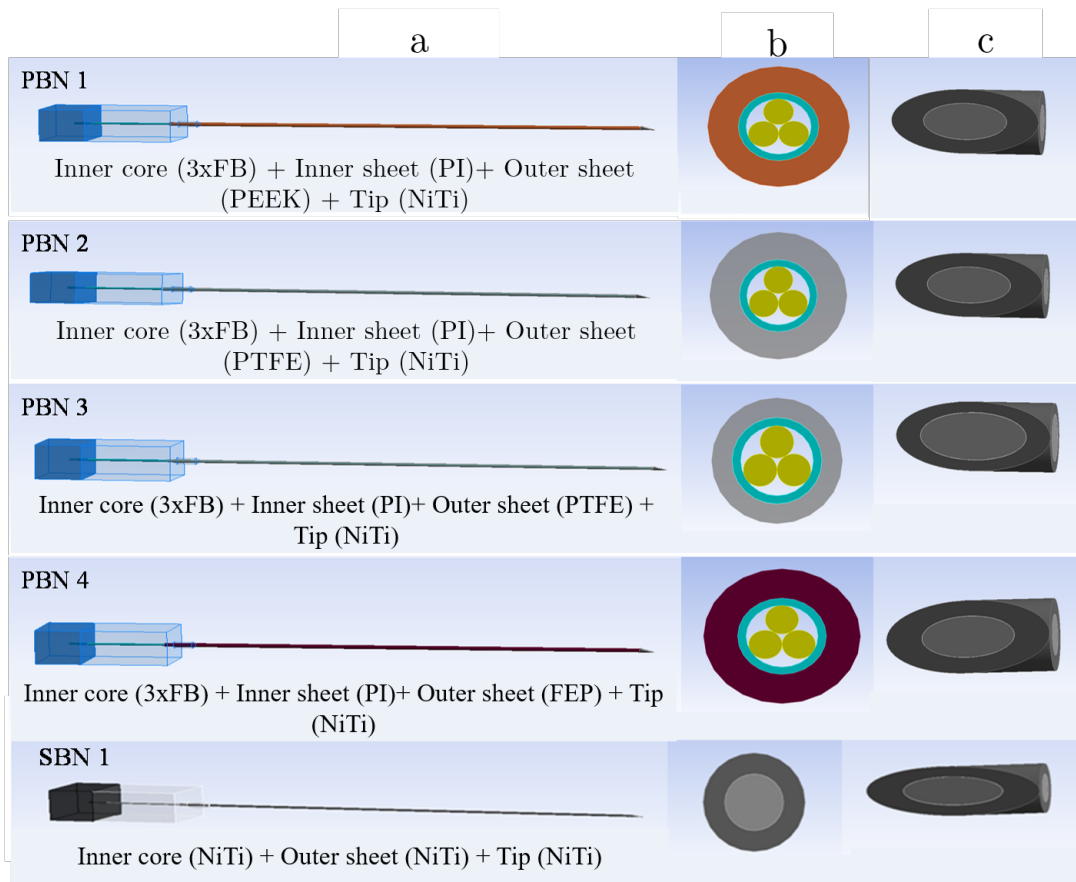


Figure 3.25: Biopsy needle design modeling in FEA: a) complete structure of the proposed biopsy needles (PBN1, PBN2, PBN3, PBN4) alongside the reference needle (SBN), b) cross-sectional view of the core needles, c) biopsy needle tips.

Table 3.9: Material mechanical properties used in FEA simulation to perform the Design II

Material properties	Nitinol	Fiber glass	Structural Steel	Polyimide	PEEK	PTFE	FEP
Young's modulus (GPa)	41-75	51.7-86.9		2.5	3.76-3.95	0.4-0.552	0.343-0.7
Poisson's ratio	0.3	0.21	0.3	0.34	0.3779	0.46	0.36
Bulk modulus (GPa)	34.2-62.5	29.7-49.9	166.7	2.6042	5.13-5.39	1.67-2.3	0.408-0.833
Shear modulus (GPa)	15.8-28.8	21.4-35.9	76.9	0.9328	1.36-1.43	0.137-0.189	0.126-0.257
Density (g/cc)	6.5	2.11-2.46	7.85	1.42	1.23-1.32	-	-
Ultimate tensile strength (MPa)	1450	2415-4890	460	231	70.3-103	-	-

Table 3.10: Dimensions used in FEA for the Design II stage for the standard biopsy needle (SBN).

Component	Dimension	Value (mm)
Inner core needle	Length	125
	Diameter	0.40
Inner core holder	Length	10
	Width	15
	Height	10
Inner core tip	Length	2.23
	Diameter	0.40
	Angle	13
Hollow outer sheet needle	Length	104
	Diameter	0.70
Outer sheet holder	Length	24
	Width	15
	Height	10
Hollow outer sheet tip	Length	3
	Diameter	0.70
	Angle	13

### 3.6.3 Uncertainty analysis in FEA: Critical analysis

To ensure the validity of the results obtained from the FEA simulation for the proposed design, it was necessary to conduct an uncertainty analysis. This process, referred to as critical analysis in ANSYS software, is a standard procedure that assesses the impact of variations or uncertainties in the input parameters on the simulation results. Through critical analysis, potential sources of error can be identified and quantified, thereby allowing for informed decision-making and enhancing the credibility of the simulation outcomes. ANSYS provides an automatic mesh convergence test as a means of validating the results. The accuracy of the results is highly dependent on the quality of the meshing process, which was essential for obtaining precise outcomes. Mesh convergence analysis is a technique used to determine the optimal mesh size required to achieve accurate results. By varying the mesh element size, the degree of deviation in the results could be observed [174, 175, 182, 183]. The error force is then utilized to estimate the accuracy of the numerical solution obtained through the chosen mesh size. Determining the optimal mesh size was achieved through a systematic process known as mesh refinement. This process involves progressively refining the mesh in specific areas of interest until the desired level of accuracy is achieved. The ideal mesh size was also influenced by the proposed design's style. In this study, the design was characterized by its elongated and slender shape, which required thorough attention to the

Table 3.11: Dimensions of the non-metallic PBNs in FEA.

Proposed biopsy needle		PBN 1	PBN 2	PBN 3	PBN 4
Inner core needle (mm)	Length	125	125	125	125
	Diameter	0.49	0.49	0.49	0.49
Inner core (mm) holder	Length	10	10	10	10
	Width	15	15	15	15
	Height	10	10	10	10
Inner core tip (mm)	Length	2.23	2.23	2.23	2.23
	Diameter	0.49	0.49	0.49	0.49
	Angle	21	21	18	21
Hollow inner sheet (mm)	Length	125	125	125	125
	Diameter	0.65	0.65	0.65	0.65
Hollow outer sheet needle	Length	104	104	104	104
	Diameter	1.15	1.15	0.95	1.15
Outer sheet holder (mm)	Length	24	24	24	24
	Width	15	15	15	15
	Height	10	10	10	10
- Hollow outer sheet - Tip angel	Length	3	3	3	3
	Diameter	1.15	1.15	0.95	1.15
	Angel	21	21	18	21

mesh element size. The findings related to the mesh size will be presented and discussed in Chapter 4.

## 4 Results and discussion

This section presents the results of our study on non-metallic needles from both an imaging and functional perspective. The results for the imaging in terms of the needle visualization were obtained through MRI scans, while the functional performance study was evaluated using both experimental and simulation analyses. In this chapter, the results are presented through qualitative and quantitative analyses conducted to compare the non-metallic proposed needles with a standard NiTi-based needle. Qualitative results were presented first, as they are particularly important for evaluating artifacts in biopsy needles in MRI scans and verifying the effectiveness of the proposed biopsy needles in reducing these artifacts. Secondly, quantitative results were presented, playing a crucial role in measuring the reduction ratio of artifacts from an MRI perspective and improving the mechanical performance of the needles.

### 4.1 Qualitative analysis for MRI artifacts

Qualitative analysis of MRI artifacts involves visual inspection of MRI images to identify the presence and nature of artifacts that are generated from biopsy needles. This analysis can provide important information for improving the quality of MRI images. We have presented the qualitative results of the MRI scans according to the type of phantom used and the parameters employed in the scan.

#### 4.1.1 Analysis of image artifacts based on MRI scans performed on a gelatin phantom

This analysis focused mainly on the appearance of the core and the complete biopsy needle for the proposed non-metallic needles in gelatin phantom and compared it with standard NiTi needle during the MRI scan.

##### 4.1.1.1 MRI results for the core needles

The MRI scan for the three cores needle in a gelatin phantom is presented in Fig. 4.1 using two different MRI sequences. Generally, based on the MRI images, the non-metallic proposed core needles 1 and 3 exhibited significantly reduced artifacts in both MRI sequences compared to the NiTi core needle. The gradient echo (GE) sequence showed more sharp details for the core's attitude in the MRI scan, such as core needle number 1, with the glass rod tip, which appeared as an air bubble artifact before the core end.

This is due to the glue used during the fabrication process, while core needle 2 appears as a complete core as artifacts. Conversely, core needle 3, which incorporated a NiTi tip at the end, presented as a "marker tip" in the MRI image, allowing for easy localization during medical interventions as shown in GE mode (left image) in Fig. 4.1. This is an indicator of localizing the core needle during interventions. Meanwhile, the spin echo (SE) sequence displays the three core needles. In principle, the appearance of the cores in the SE sequence was smaller than in the GE sequence. This difference is due to the nature of the SE sequence, which involves a refocusing step during the MRI scan. In the SE sequence, radiofrequency pulses are used to manipulate hydrogen nuclei in the tissues to create signals for image construction. However, these signals can become out of phase with each other, leading to a loss of signal intensity and contrast. To address this, the SE sequence includes refocusing pulses at specific intervals to realign the hydrogen nuclei and bring the signals back in phase. This refocusing process enhances image contrast and sharpness, resulting in smaller but clearer depictions of the cores in the SE images. On the other hand, the GE sequence does not have this specific refocusing step, leading to potentially larger but less distinct core appearances in the GE images. However, Based on the literature the refocusing step in the SE sequence helps to enhance image contrast and sharpness in certain cases, it may not always result in a significant improvement in image quality. The effectiveness of the refocusing step depends on various factors, such as the specific imaging parameters used, the nature of the tissue being imaged, and the presence of artifacts or other imaging challenges. In some situations, the improvement in image quality achieved through refocusing might be relatively minor, or the benefits may be outweighed by other factors impacting the overall image quality. Therefore, it is accurate to say that the refocusing step in the SE sequence does not guarantee a substantial improvement in image quality in all instances [184]. The results of the test indicated that in both sequences, cores 1 and 3 exhibit less artifacts compared to the NiTi needle. To quantify the artifact ratio in both MR image sequences, quantitative measurements were evaluated for each core's width and length, and the results were presented in the quantitative section in Fig. 4.8(a) and Fig. 4.8(b).

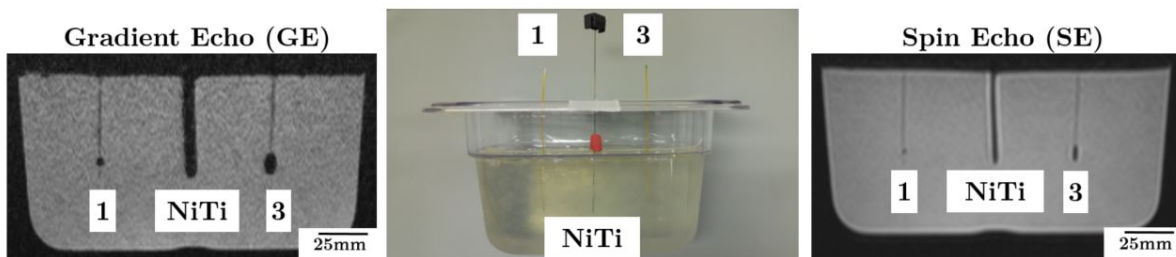


Figure 4.1: MRI scan results for the three cores needles 1, NiTi, and 3 inside gelatin phantom presented GE (left image) and SE (right image) sequences.

#### 4.1.1.2 MRI results for the biopsy needles

The results for the complete proposed non-metallic and NiTi biopsy needles in a gelatin phantom is illustrated in Fig. 4.2. Subsequently, the experiment was repeated using the same two MRI sequences as before. The non-metallic needles from (1 to 7) show significantly reduced artifacts compared to the NiTi needle in both sequences. It is important to note that both MRI images were obtained at the same location of the phantom with needles inside the MRI machine. Basically, the needles' performance regarding artifacts in the GE sequence shows large needle artifacts compared to the visualization of the needles in the SE sequence. Despite generating fewer needle artifacts, the SE sequence may present challenges in locating the needle within the MRI image when this type of artifact is present. They can affect the visibility of the needle in the image, making it difficult for medical professionals to accurately identify its precise location. Therefore, while the SE sequence offers benefits in reducing overall artifacts, it still has limitations related to needle localization, which could be critical for medical procedures requiring precise needle positioning. The visualization of the needle artifact should exhibit adequate visibility without being excessively enlarged. Furthermore, the artifact should accurately depict the precise location of the needle.

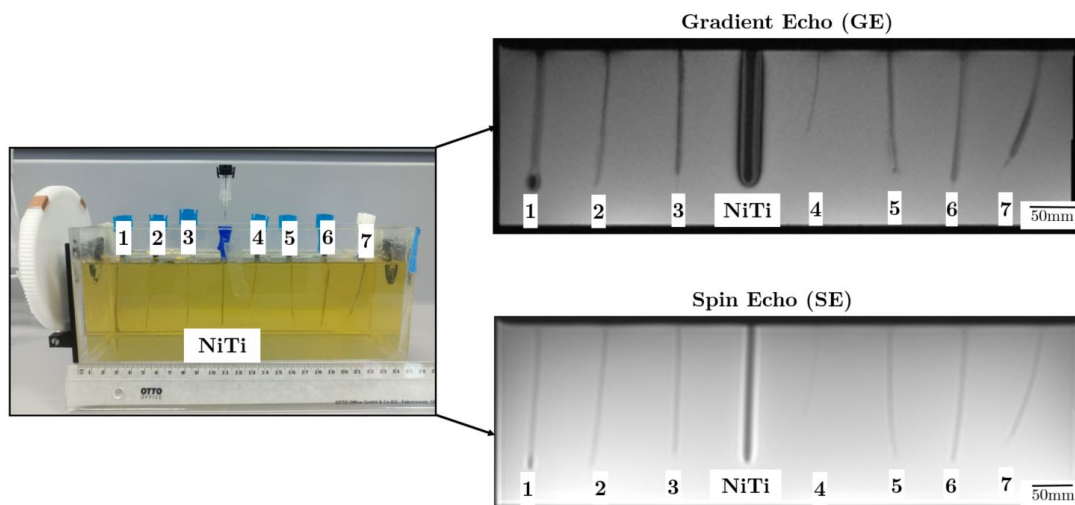


Figure 4.2: MR images of eight needles inside a phantom, with proposed needles labeled from (1-7) and a NiTi needle used as a reference. Images are shown in both the GE sequence (above) and the SE sequence (below). The proposed needles demonstrate minimal artifact levels, while the NiTi needle exhibits significant artifacts.

#### 4.1.1.3 MRI results of rotated biopsy needles in a gelatin phantom

The MRI results showed needle 1 and NiTi in four rotational steps using GE and SE sequences presented in Fig. 4.3. A noticeable artifact variation was observed in Fig. 4.3(a),

at  $0^\circ$  in both needles NiTi and 1 compared to the other angles in Fig. 4.3. While the needles in the SE sequence gave the same appearance for the four rotational angles. To quantify the impact of rotation on both needles, a measurement step was performed, and the results are presented in the section related to the quantification part in Table 4.1 and Table 4.2.

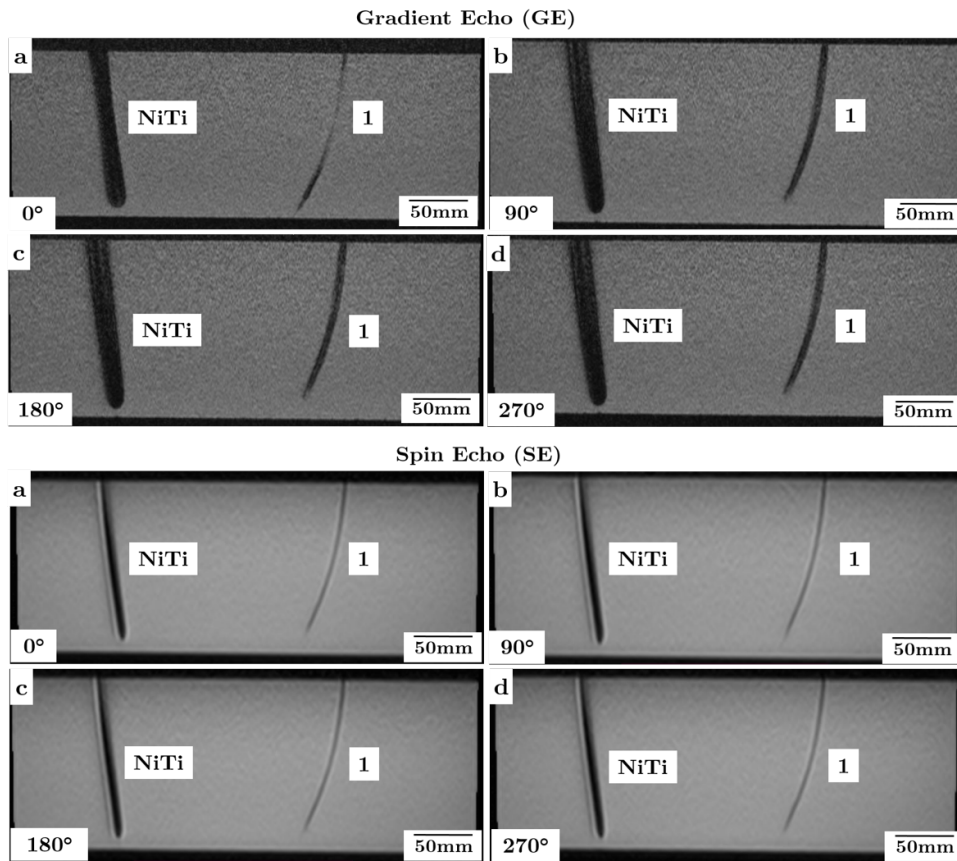


Figure 4.3: MRI scans of NiTi and needle number 1 in a gelatin phantom were obtained using GE and SE sequences at a)  $0^\circ$ , b)  $90^\circ$ , c)  $180^\circ$ , and d)  $270^\circ$  rotation angles to differentiate artifacts between the two sequences.

#### 4.1.2 Analysis of image artifacts based on MRI scans of needles in tissue-engineered phantom

This section presents a comprehensive analysis and discussion of the artifacts observed in non-metallic needles implanted in a tissue-engineered phantom, using both two-dimensional (2D) and three-dimensional (3D) modes during MRI scans. The MRI image confirmed significantly lower artifacts in the non-metallic 1 and 3 needles compared to the NiTi needle. The NiTi needle had the highest artifacts value in both GE and SE sequences. However, needle 1 was not detectable in the SE sequence due to needle alignment, and susceptibility artifacts were generally small in the SE sequence. Meanwhile, the artifacts for NiTi and needles 3 were too small to visualize the needles in comparison to the GE sequence. A



2D MRI scan was acquired using GE and SE sequences. The scan was performed on all needles collectively as a group scan, followed by individual scans of each needle using the same parameters. The resulting images were presented as displayed in Fig. 4.4 and Fig. 4.5 respectively. While the MRI scans were performed in 3D mode using the GE sequence to visualize three needles in both longitudinal and cross-sectional perspectives. In the longitudinal view, the MRI machine acquired images by aligning with the length of the long axis of the needles. This view provided a detailed portrayal of the needles along their entire length. In the cross-sectional view, the MRI machine obtained images by slicing the target area perpendicular to the long axis of the needles. This view allowed for a detailed examination of the internal structure of the needles at different levels. The resulting images for both perspectives are displayed in Fig. 4.6 and Fig. 4.7 respectively. Qualitatively, the visibility of the three needles was higher in the MRI scans obtained using the GE sequence, as illustrated in Fig. 4.4(a) and Fig. 4.5. Non-metallic needles (1 and 3) exhibited significantly fewer artifacts compared to the standard NiTi needle. However, in the SE sequence, the non-metallic needles were less visible due to their low-susceptibility artifact, which could potentially limit their use in biopsy procedures as depicted in Fig. 4.4(b) and Fig. 4.5. As a result, needles (1 and 3) may not have clear boundaries that can be easily distinguished from the NiTi needle. This could potentially have a negative impact on the overall image quality. The reduced visibility of needles (1 and 3) in the SE sequence can be attributed to their low-susceptibility artifact. A low-susceptibility artifact arises when an object has very little or no magnetic susceptibility, meaning it does not significantly disturb the surrounding magnetic field during the MRI process. This can lead to reduced signal intensity and poor visibility of the objects in the image. On the other hand, the standard NiTi needle, being metallic, was more susceptible to magnetic fields and causes more significant distortion of the magnetic field during the MRI scan. This results in a stronger signal and better visibility of the NiTi needle in the SE sequence compared to the non-metallic needles. In summary, the low-susceptibility artifact in the SE sequence affects the visibility of non-metallic needles (1 and 3) more significantly than the NiTi needle. This creates challenges in clearly distinguishing the boundaries of these needles in the SE images. As a result, the SE sequence might not be the optimal choice for visualizing non-metallic needles, and the GE sequence could be preferred for biopsy procedures involving such needles. Nevertheless, the proposed needles 1 and 3 demonstrated superior performance in terms of generating fewer artifacts in both GE and SE sequences, as compared to the standard NiTi needle. Additionally, longitudinal-section MRI scans of needles 1, NiTi, and 3 were acquired in a tissue-engineered phantom using both 2D and 3D modes. The resulting images were then compared to assess any differences in image quality. The comparison involved visually evaluating the clarity of needle boundaries, the presence of artifacts, and the overall image resolution. An illustrative example of these scans is provided in Fig. 4.6. The artifacts present in the MRI

scans of needles (1 and 3) were more noticeable in the 2D mode compared to the 3D mode. This difference in artifact visibility can be attributed to the way images are reconstructed in each mode. In 2D mode, only one plane (usually the sagittal plane) is used for image reconstruction. This means that the MRI machine captures data from a single slice through the target area, providing a two-dimensional representation of the object being imaged. As a result, any artifacts present in that particular slice become more pronounced and may affect the overall image quality. On the other hand, in 3D mode, the MRI machine acquires data from three planes (sagittal, transverse, and coronal). This allows for the construction of a three-dimensional representation of the target area. By combining data from multiple slices, the 3D mode reduces the impact of artifacts in any single slice and provides a more comprehensive and accurate visualization of the object. The increased artifact visibility in the 2D mode for needles (1 and 3) suggests that these artifacts are more localized to specific slices, leading to a more pronounced effect on the overall image quality when using a single plane. In contrast, the 3D mode's ability to incorporate data from multiple planes helps to mitigate the impact of artifacts and results in better image quality for the needles. Using 3D mode in MRI imaging allows for a more comprehensive representation of the needle's orientation. The 3D mode captures data from multiple planes (sagittal, transverse, and coronal), which helps to provide a three-dimensional view of the needle. By incorporating information from different perspectives, the 3D mode can reduce the influence of artifacts on the final image, leading to better image quality and improved visualization of the needle. However, it was observed that the proposed non-metallic needles exhibited fewer artifacts in both 2D and 3D modes compared to the NiTi needle. The presence of fewer artifacts suggests that the proposed non-metallic needles produced clearer and more reliable MRI images, leading to improved visualization and potentially more accurate diagnostic information. Moreover, cross-sectional MRI scans of the three needles were acquired in both 2D and 3D modes, providing an additional perspective on their artifact performance. An example of these scans is illustrated in the following Fig. 4.7. The MRI scan was performed in 2D mode using both GE and SE sequences for the same slice image. The results indicated that the NiTi needle exhibited higher artifact recording than needles 1 and 3. Conversely, only the GE sequence was available for the 3D mode. However, in our experience, applying the 3D mode in a real scenario can result in motion-induced artifacts that corrupt the image. Additionally, the imaging time for 3D mode is longer compared to the 2D mode [156].

In Fig. 4.4(a) and Fig. 4.5 circular artifact was noted surrounding the tip of needle 2, attributable to the use of NiTi as a tip material. In contrast, needle 1, featuring a GR tip, exhibited a clearly discernible needle end, signifying its superior capacity to accurately localize the target tissue.

In summary, the qualitative MRI image evaluation shows that GE sequences are more susceptible to artifacts on biopsy needles compared to SE sequences. This is because GE

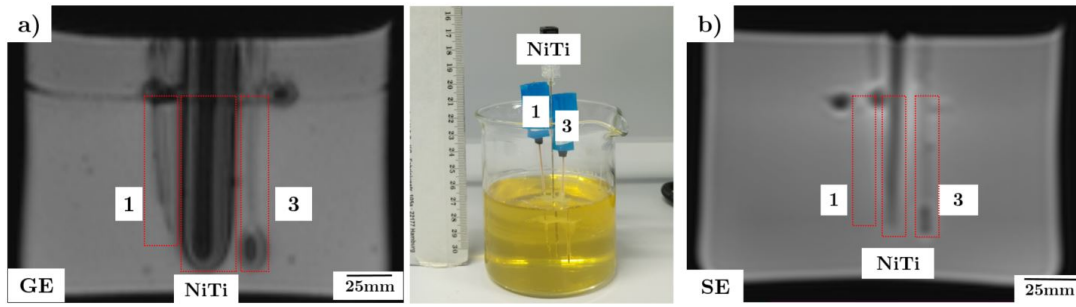


Figure 4.4: Qualitative comparison MRI group scans in the 2D mode in a) GE sequence and b) SE sequence for three biopsy needles (1, NiTi, and 3) in tissue-engineered phantom.

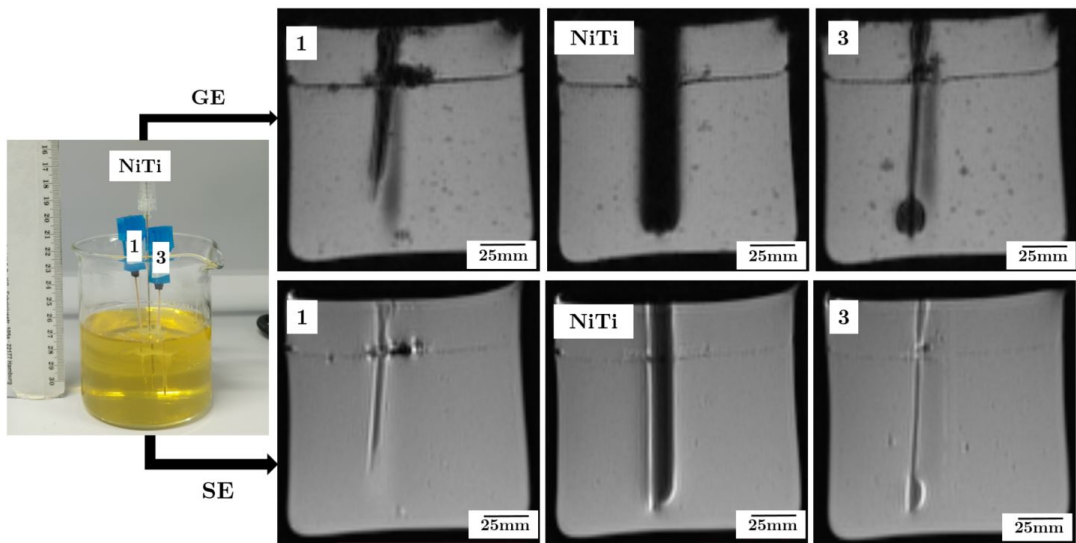


Figure 4.5: A comparison for individual 2D MRI scan between GE and SE sequence for (1, NiTi, and 3) biopsy needle in tissue-engineered phantom.

sequences are more sensitive to magnetic field inhomogeneities caused by objects, leading to signal loss and distortion. Additionally, the SE sequence may have its own limitations when it comes to visualizing biopsy needles, such as reduced signal-to-noise ratio and longer scan times.

## 4.2 Quantitative analysis for MRI artifacts

This section reports the quantitative findings from evaluating artifacts generated by non-metallic needles during MRI scans, in comparison to a NiTi needle. The objective was to quantify and compare the extent of artifacts generated by each type of needle.

To achieve this, the width and length of each needle were measured three times, and the resulting data were recorded along with their corresponding standard deviations. This approach allowed for a more precise and accurate characterization of the measurements, as it accounted for any inherent variability in the data. The artifacts generated by each

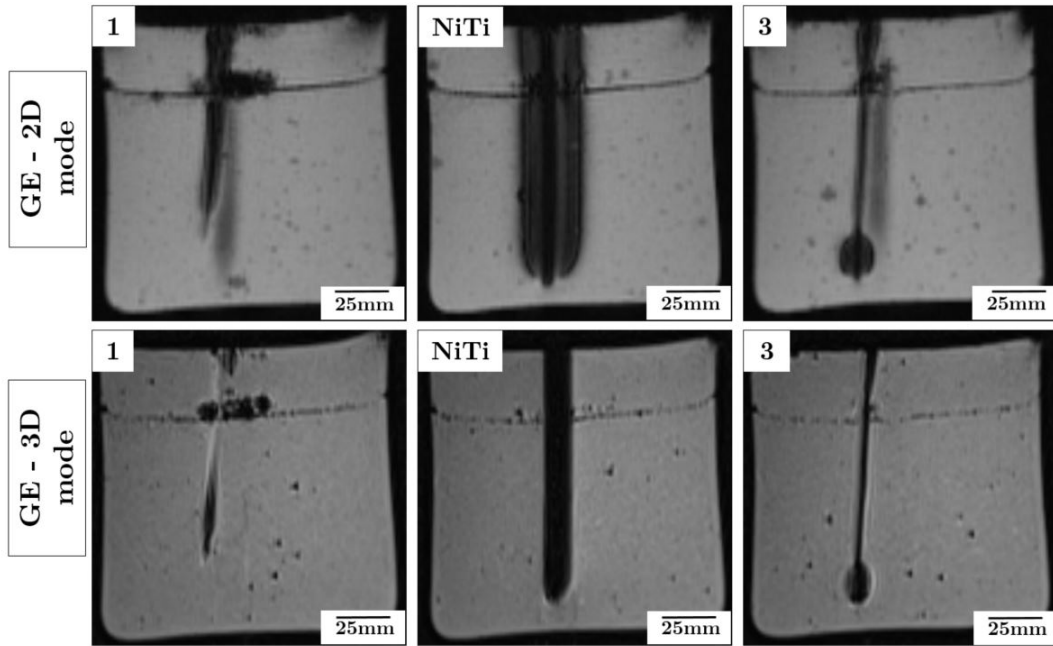


Figure 4.6: Qualitative comparison of individual MRI scans in 2D and 3D mode using GE sequence for longitudinal sections for the three biopsy needles, 1 and 3 for the proposed needle, and NiTi for the standard needle.

needle were then quantified and represented graphically as a bar chart. The analysis of the data obtained from the measurements provides a quantitative assessment of the impact of using NiTi needles on the quality of MRI images. This enables a more comprehensive understanding of the extent to which image quality is affected when using such needles in clinical practice.

#### 4.2.1 Assessing artifacts from core biopsy needles

The width and length artifacts of each core needle were measured, and the results demonstrated significantly lower artifact values in needles (1 and 3) compared to the NiTi needle, which was consistent with their visual appearance in the MRI image. Fig. 4.8 presents a comparative evaluation of the core artifacts between the acquisitions using the GE and SE sequences. The width artifact determination for needles (1 and 3) in the GE sequence was performed close to the reference line as seen in Fig. 4.8(a), the reference line indicates the actual width while the NiTi needle had higher artifact values. While Fig. 4.8(b) shows that the scanning using the SE sequence records a lower average length of artifacts compared to the scan in the GE sequence. The SE sequence scan demonstrated compromised visualization of the needle boundaries, resulting in reduced clarity and increased difficulty in differentiation compared to the GE sequence. The blurred boundaries in the SE sequence images made it challenging to accurately distinguish the needles' precise locations and orientations within the target area. In contrast, the GE sequence provided sharper and more distinct representations of the needle boundaries,

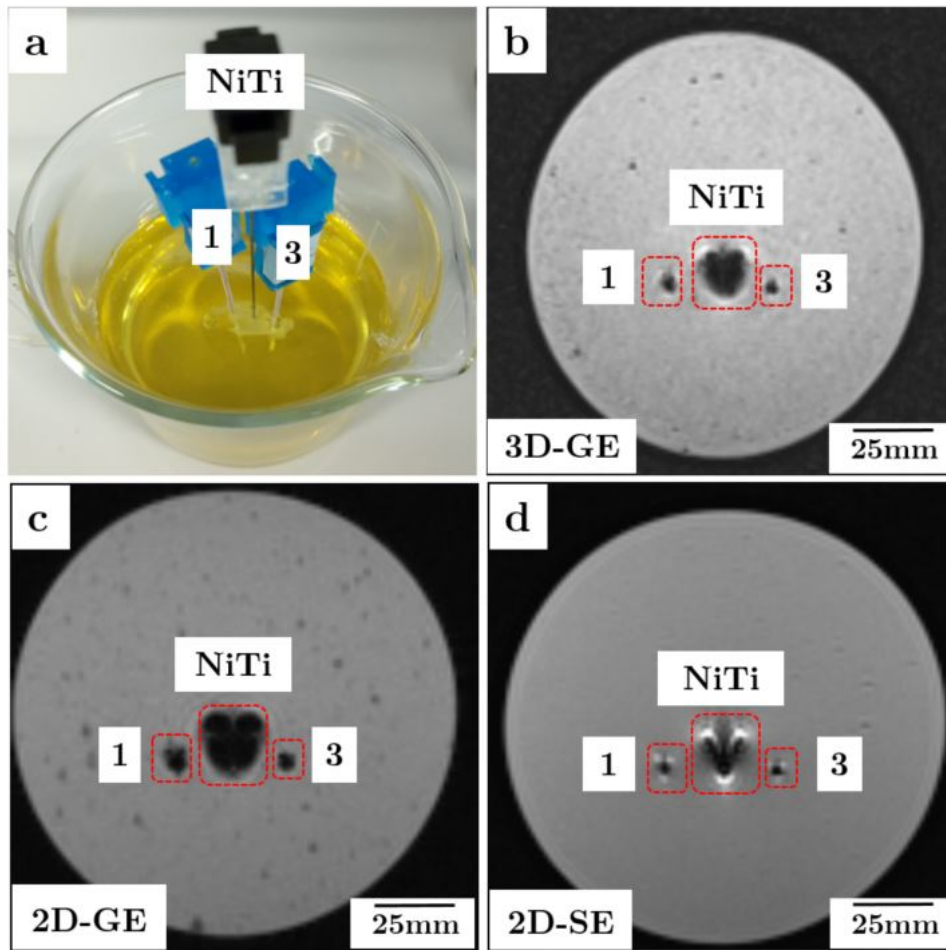


Figure 4.7: Comparison of MRI scans between 2D and 3D mode in cross-section perspective for the three biopsy needles, 1, NiTi, and 3 in tissue-engineered phantom: a) the three needles inside the tissue-engineered phantom, b) the cross-section MRI scan for the three needles in GE sequence 3D mode, c) MRI scan using GE sequence with 2D mode and d) MRI scan under SE sequence in 2D mode.

allowing for a more precise assessment of their positions and alignments.

#### 4.2.2 Assessing artifacts from the biopsy needles

The results regarding the quantification of the artifacts for complete biopsy needles are reported in terms of needle widths and lengths, which were used to assess the presence of imaging artifacts in the MRI scans. The average width measurements for each needle are presented in Fig. 4.9(a). The NiTi needle exhibited the highest width artifacts when the GE sequence was used for the MR imaging. The number of artifacts was higher for the needles in the GE sequence compared to the SE sequence, owing to the GE sequence's ability to show sharper details of the needle's performance. Similarly, the average length artifacts for the needles in Fig. 4.9(b) showed higher values in the GE sequence than in the SE sequence. The use of a glass rod tip with a sharp ending caused needle number 2 to exhibit the highest artifact length in the GE sequence.

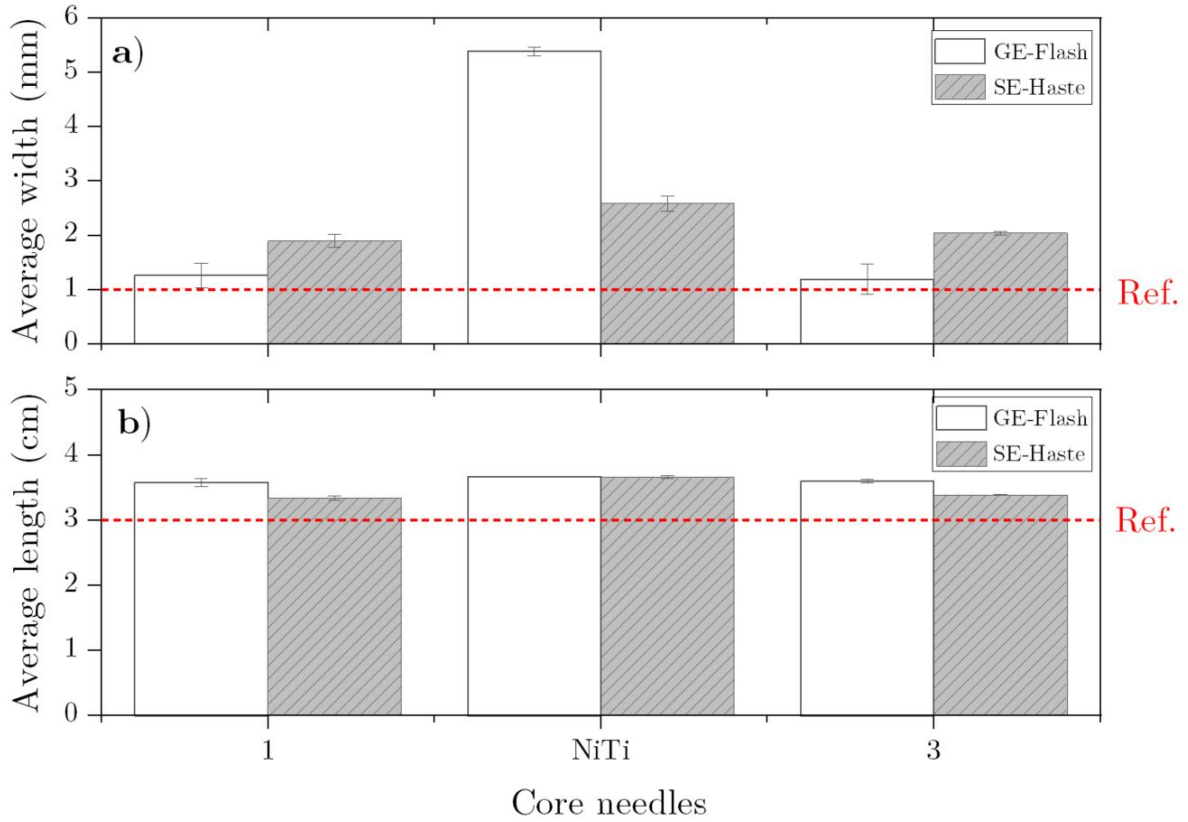


Figure 4.8: Artifacts evaluation for the (1, NiTi, and 3) cores, the x-axis represents the cores used. In contrast, the y-axis represents the average width and length measured in mm with a standard deviation: a) width measurements for 1, NiTi, and 3 cores in two MRI sequences GE represented in the white bar and SE represented in the gray bar and compared with reference standard width, while b) measuring the length for (1, NiTi, 3) cores in GE represented in the white bar while the gray bar for SE sequence. The red bar and discrete line represent the actual width and length used as a reference.

#### 4.2.3 Assessing artifacts of rotated biopsy needles in gelatin phantom

Table 4.1 presents the artifacts of both NiTi and needle number 1, as displayed in the images obtained using the GE sequence at four different rotation angles. It was observed that the artifact values for both needles were lower at  $0^\circ$  compared to the  $90^\circ$ ,  $180^\circ$ , and  $270^\circ$  angles. Furthermore, when needle 1 was rotated at  $90^\circ$ , a slight 0.6% reduction in length was observed, while the length remained the same at the other rotation angles. However, the width increased when the rotation angle changed from  $0^\circ$  to  $90^\circ$  and  $180^\circ$ . Additionally, Table 4.2 details the artifacts for both needles in the SE sequence at the same four rotational angles as used in the GE sequence. In this case, slight artifacts were detected for both needles at all four angles. This outcome can be attributed to the SE sequence's limited capability to display fine details when compared to the GE sequence. Overall, the results of our study suggest that the susceptibility artifacts produced by

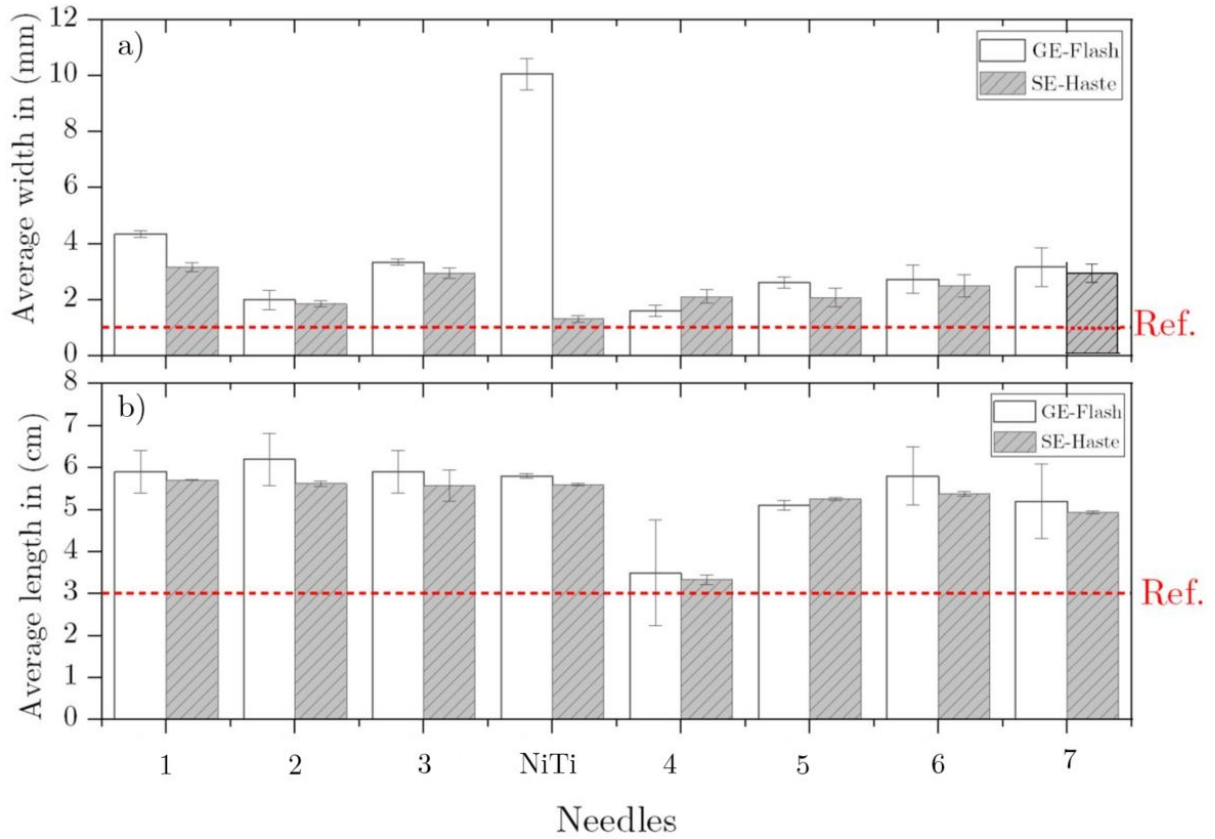


Figure 4.9: Artifacts evaluation for the seven prospered needles with NiTi needle in two MRI sequences: a) width needle compassion for each needle in GE sequence, which is represented in a White bar, while the gray bar represents the needles in SE sequence and b) average length measurements for the needles in mm in two sequences.

rotating the biopsy needle in an MRI scan are not significant. Although some artifacts were observed, their impact on the visualization of the needle or surrounding tissue was minimal. These findings suggest that rotating the biopsy needle during an MRI scan is unlikely to cause significant image distortion and should not affect the accuracy of diagnosis or treatment planning.

Table 4.1: Quantifying the width and length of the artifact for the needle (NiTi + 1) at four rotational angles when the MRI sequence is in GE.

Needle	Dimensions (mm)	0°	90°	180°	270°
NiTi	Width	8.32	8.78	9.52	8.93
	Length	70	71	70	71
1	Width	2.83	4.64	4.36	3.7
	Length	74	66	67	67

Table 4.2: Artifacts quantification for NiTi and 1 including the width and length for each needle in mm when the MRI sequence is SE.

Needle	Dimensions (mm)	0°	90°	180°	270°
NiTi	Width	6.79	6.78	6.50	6.61
	Length	70	70	70	71
1	Width	2.28	2.96	2.83	2.89
	Length	67.23	66.8	67.3	68.03

#### 4.2.4 Assessing artifacts of biopsy needles in a tissue-engineered phantom

The MR imaging results for the three needles inside the custom-made tissue-engineered phantom showed a clear reduction in the artifacts of the proposed non-metallic needles 1 and 3 compared with the standard NiTi needle. The mean  $\bar{X}$  and standard deviation (SD) were calculated for three repetitive measurements of the data in both the width and length directions for each needle. The artifacts were evaluated using MRI images for the needles from the group scan shown in Fig. 4.4, as well as, individual MRI scans for each needle, depicted in Fig. 4.5. The results of the evaluations are presented in Fig. 4.10(a), (b) and (c), d respectively. It was observed that the proposed needle 3 exhibited artifacts in length measurements, recording 3.3 mm, which closely aligned with the Reference Ref. line of 3 mm in both group and individual scans during the GE sequence, as shown in bar chart Fig. 4.10(c) and (d). Meanwhile, needle 1 exhibited length artifacts measuring below the Ref. line, which is 2.5 mm. This is due to the needle alignment bending a little during the insertion process in the phantom. Furthermore, the quantification for the needle artifacts in 2D and 3D MRI scans is presented in Fig. 4.11. The analysis revealed that the NiTi needle consistently exhibited the most significant artifacts in both 2D and 3D modes when utilizing the GE sequence. Among the needles, Needle 3 displayed the smallest disparity in artifact length, measuring at 3.3 mm, which closely aligns with the reference line of 3 mm. Additionally, Needle 3 demonstrated an artifact width of 1.2 mm, mirroring the reference line of 1 mm. In the same analysis, it was observed that the proposed needle 1 exhibited artifacts measuring less than 3 mm in length, a deviation from the reference line. This deviation can be attributed to needle bending and its non-conforming position, as it was not inserted perfectly straight. Additionally, the captured artifact width measured 1.5 mm, slightly surpassing the 1 mm reference line. In conclusion, the proposed non-metallic needles demonstrated lower susceptibility artifacts in various MRI scan setups used in this study when compared to the NiTi needle. This finding was quantitatively assessed, suggesting that the proposed needles may provide better image quality and accuracy in MRI-guided biopsy procedures, potentially improving diagnosis and treatment outcomes.



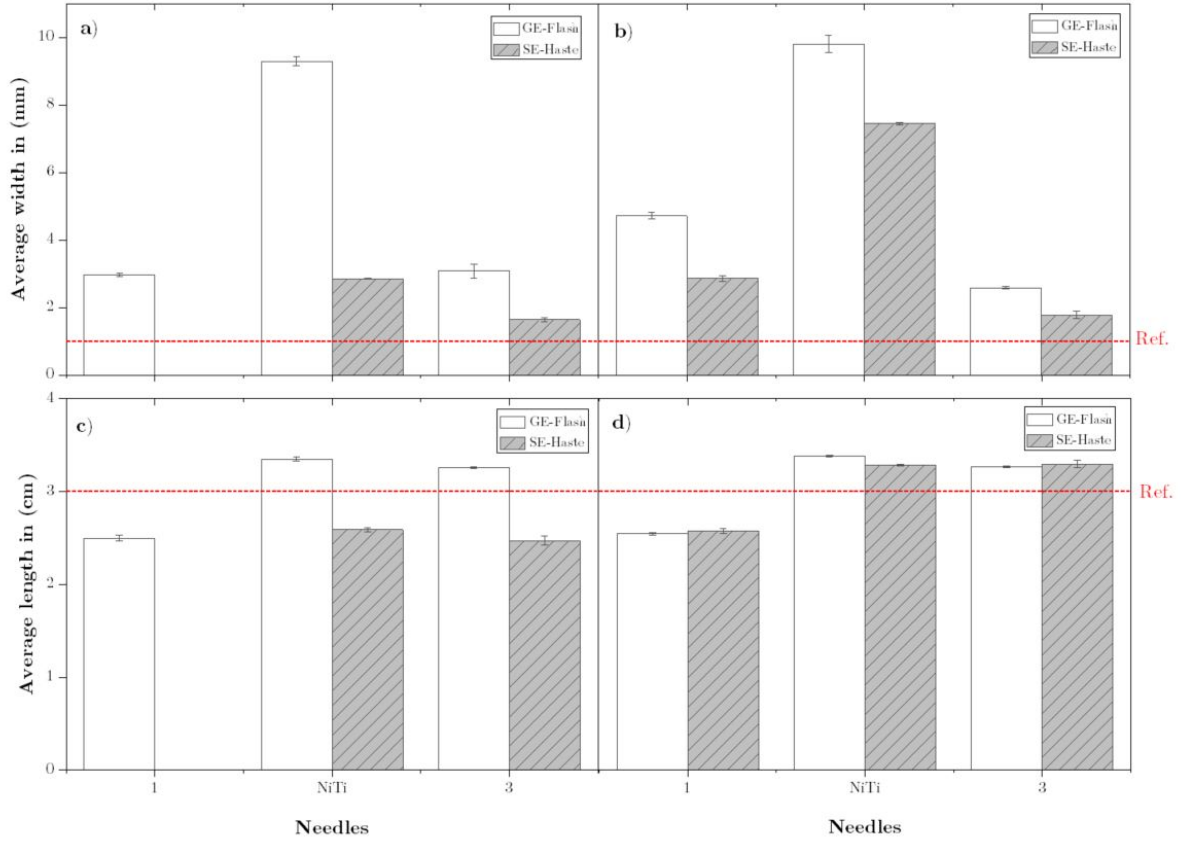


Figure 4.10: Results of artifacts evaluation for the widths and lengths of the three needles (1, NiTi, 3) in the gelatin phantom: a) and c) represent the average width and length in a group MRI scan, while b) and d) illustrate the average measurements for width and length each needle in individual MRI scan needles. The white bar represents the needles performance in the GE sequence, while the gray bar shows the needles in the SE sequence.

#### 4.2.5 Assessing artifacts of biopsy needles using machine learning

The K-means clustering algorithm was applied to the MRI images obtained from a group scan of the needles. The resulting clustered images as detailed in Chapter 3, section 3.5.2 displayed in Fig. 4.12. In this step, the proposed non-metallic needles were labeled as (L1, L2, L3, L5, L6, L7, and L8), while the NiTi needle was labeled as (L4). As substantiated by prior findings, these suggested non-metallic needles demonstrated a notable mitigation of susceptibility artifacts in contrast to the conventional NiTi needle (L4), which yielded considerable artifact manifestation. To numerically assess these artifacts, we employed the K-means algorithm to identify and measure them individually across varying needle widths and lengths. This quantification process proceeded as follows:

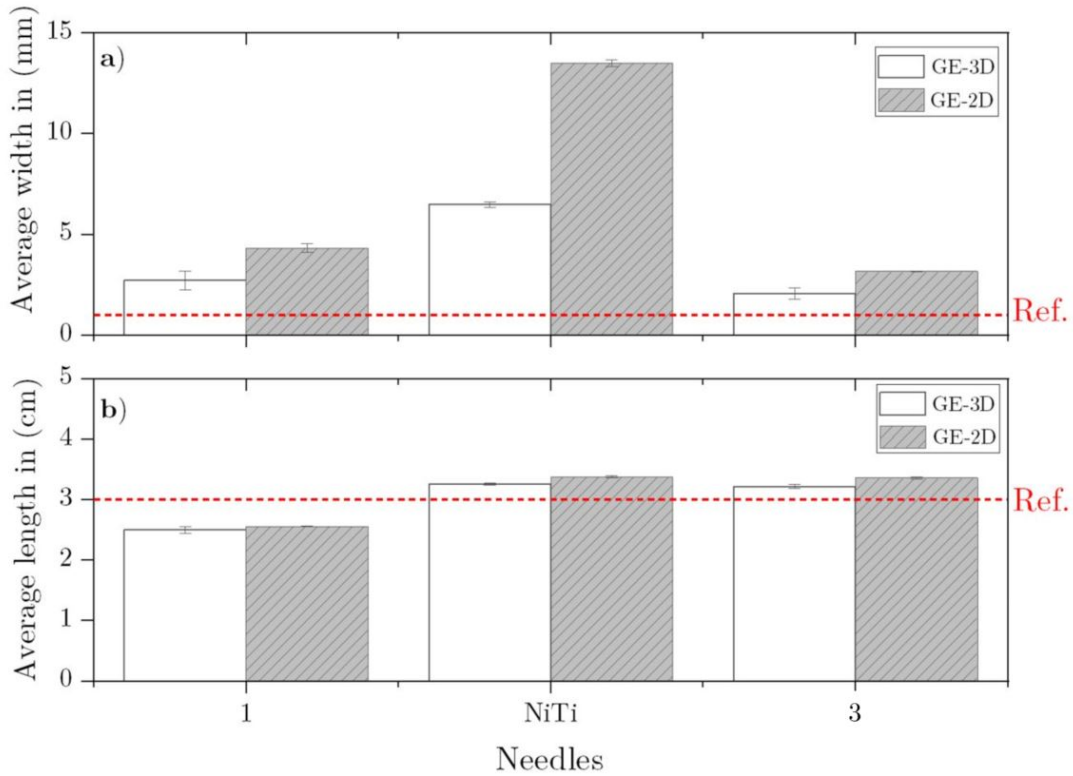


Figure 4.11: Artifacts assessment based on the MRI mode for the needles (1, NiTi, and 3) in tissue-engineered phantom: a) represent the average width with standard deviation for the needles in 3D mode and 2D mode, while b) describes the average length for the needles (1, NiTi and 3) in 2D mode reflect in the white bar although the gray bar illustrates the artifacts for the length in 3D.

#### 4.2.5.1 Artifacts quantification: Needles width

The width quantification results for manual and K-means clusters applied to the eight needles are shown in Fig. 4.13. The results encompassed uncertainty quantification for determining the artifact width across the eight needles. Therefore, Fig. 4.13 has eight sub-figures corresponding to each needle. Each sub-figure shows a comparison of two quantifications in the form of the mean  $\bar{X}$  of the data and its standard deviation (SD) for each needle measured in (mm). The manual measurements were made directly from the MR images using the RadiAnt Dicom viewer. The results are represented as gray bars for each needle from L1 to L8 in Fig. 4.13. The width measurements for K-means clustered images are depicted as light blue bars for each needle after applying different cluster numbers. Moreover, a red dotted reference line for each sub-figure in Fig. 4.13 serves as ground truth to indicate the geometric needle width in mm. The K-means clustering algorithm was applied to the images to determine the optimal number of clusters that would detect the entire body of the proposed non-metallic needles as well as the standard needle. The evaluation of the clustering performance was based on the alignment of the achieved values with a reference line. Our results showed that for needle L2, most clusters

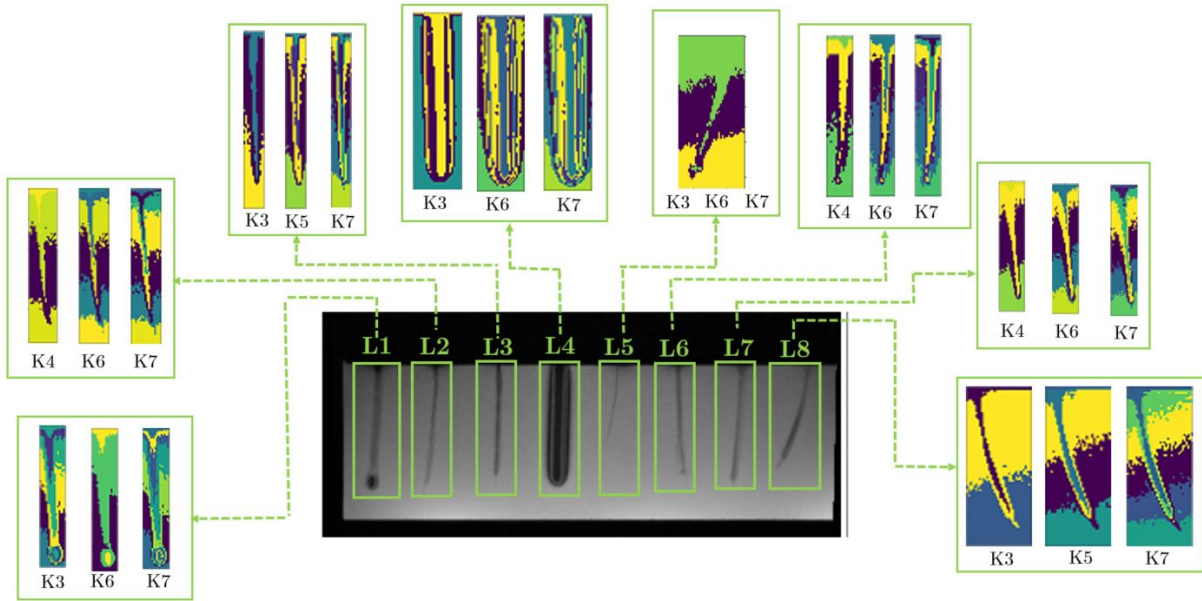


Figure 4.12: Clustered images for the 8 needles from MR images, non-metallic needles labeled as L1, L2, L3, L5, L6, L7, L8 while the NiTi needle labeled as L4 using cluster range from K3 to K7.

achieved values closest to the reference line at  $K=7$ , while for needle L3, cluster  $K=3$  yielded the best alignment. For needle L5, cluster  $K=6$  achieved optimal performance, and for needle L8, cluster  $K=3$  yielded the best results. Furthermore, the dimensions of the clustered images were evaluated for different numbers of clusters, and the achieved values were found to be close to the reference line. For needle L2 the highest degree of similarity between the reference line and the dimension in the MRI was observed for the highest number of clusters with  $K=7$ , whereas for needle L3 the closest match was observed for the lowest investigated cluster number  $K=3$ . This indicates that there was no unique  $K$ -value that achieved optimal performance in all of the investigated needles. It's important to mention that the new proposed needle L1 recorded high susceptibility artifacts due to the NiTi structure attached as a tip to the needle shaft. However, as expected, needle L4 which represents the standard NiTi needle, showed the highest artifacts in the width direction in both quantification approaches compared to the proposed non-metallic needles.

#### 4.2.5.2 Artifacts quantification: Needles length

This section presents the results of artifact length quantification for the eight needles in the MRI image presented in Fig. 3.15 using the same artifact detection approaches that were used in quantifying the needle width. Fig. 4.14 displays the results of quantifying the length of the artifact for MRI needles from L1 to L8. It involves an uncertainty assessment of the eight needles, determined through the calculation of the average and its corresponding standard deviation after applying the cluster values obtained from the

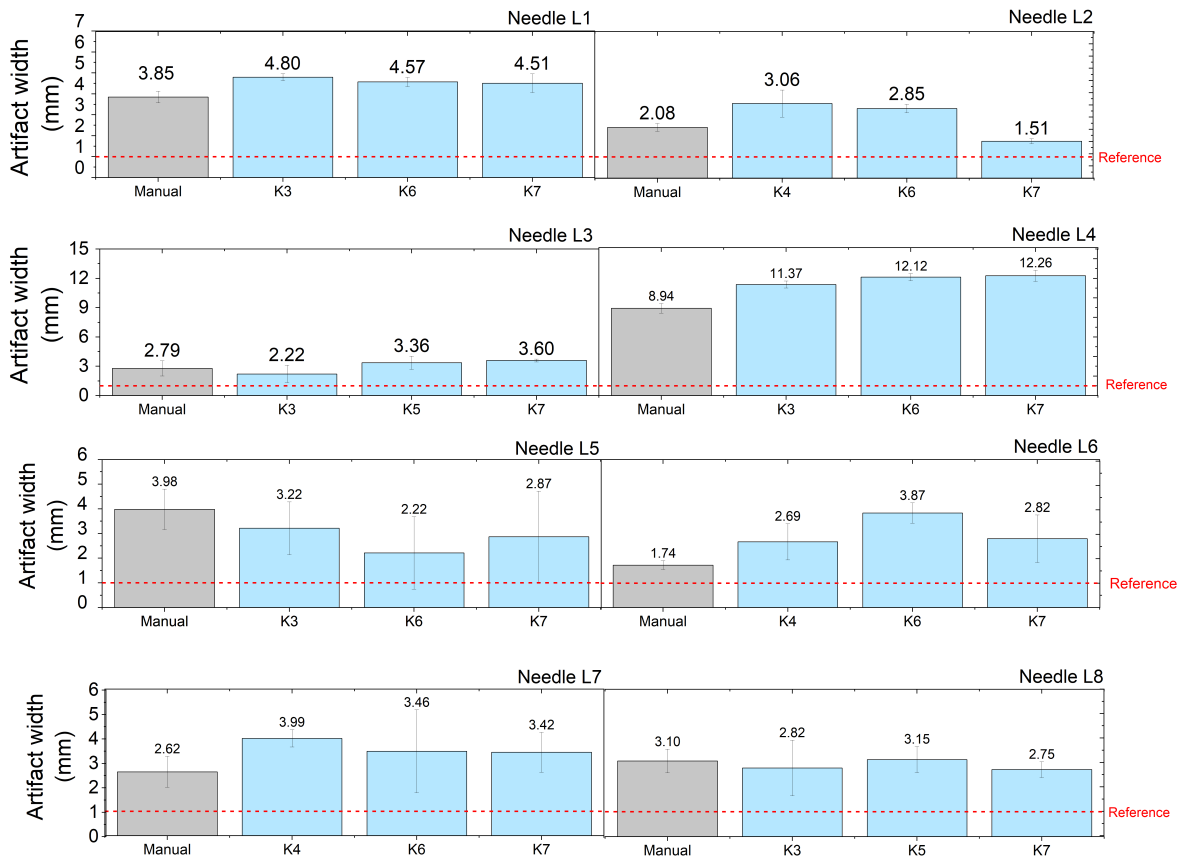


Figure 4.13: Results of comparison the width of the artifact in (mm) between manual quantification and K-means quantification, the manual quantification is represented as the gray color bar from L1 to L8. While K-means cluster quantification represents light blue bars. The x-axis represents the manual and the K-means cluster that has been applied to the needles. The y-axis signifies artifact width values in (mm) for each respective needle. The reference line indicates the standard needle width used as the established ground truth, measuring 50 mm.

K-means algorithm. In these measurements, the K-means approach achieves promising results close to the reference line, as shown in Fig. 4.14. The results revealed notable alignment between cluster K=7 and the reference line for needles L2, L5, L6, and L7. However, an interesting observation was made concerning the quantification of the needle labeled as L8. Specifically, for cluster numbers K=5 and K=7, the quantification results were found to be lower than the ground truth. This divergence can be attributed to the alignment and bending characteristics of the needle within the gelatin phantom.

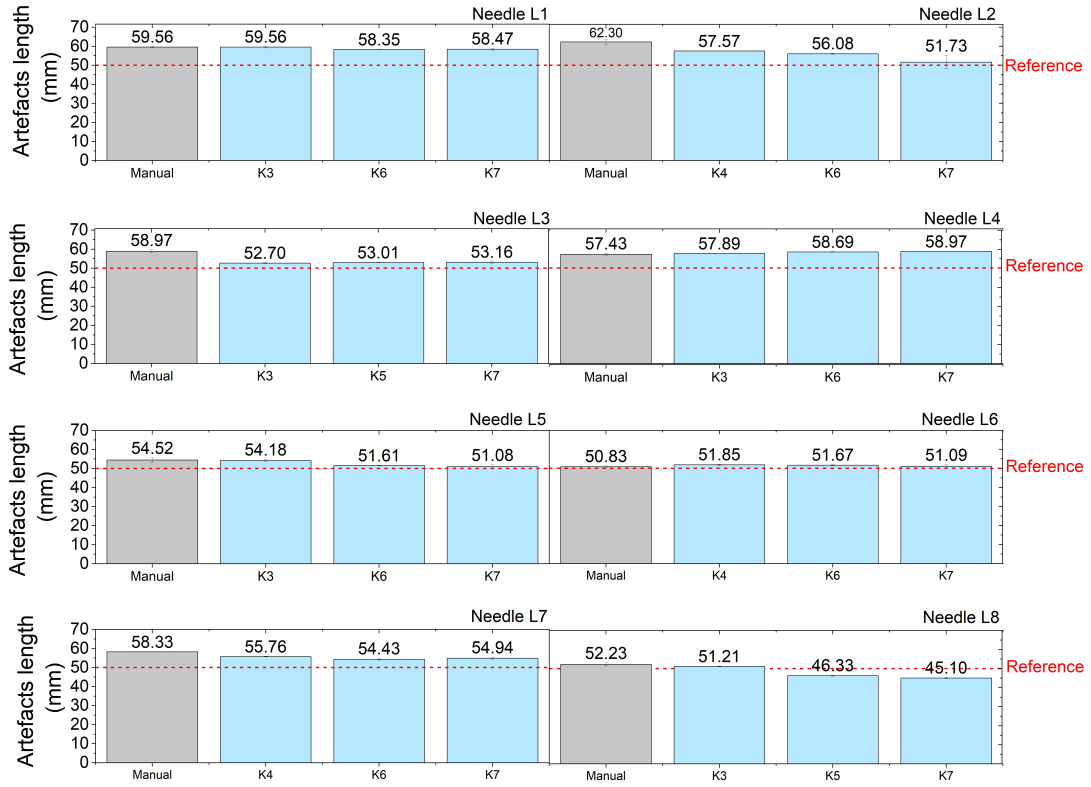


Figure 4.14: Results of comparison of the length of the artifact in (mm) between manual quantification and K-means cluster quantification, the manual quantification represents in the gray color bar from L1 to L8. While K-means cluster quantification represents a light blue bar. The x-axis represents the manual and the K-means clusters that have been applied to the needles. Meanwhile, the y-axis corresponds to the values of artifacts for the length measurements in (mm). The reference line mapped to the standard needle length used as ground truth which corresponds to 50 mm.

#### 4.2.5.3 Cluster validation: Silhouette score

In this study, the Silhouette coefficient was employed to assess the quality of the clustering technique. The Silhouette coefficient serves as a metric to evaluate the performance of cluster measurements and it can point out which needles under the cluster were placed well within their group or well-matched and similar to the others. Like refers to the positioning

of data points or elements (in our case, needles) within their respective clusters or groups in a way that indicates a high level of similarity or cohesion among the data points within each cluster and which were performing as an outlier refers to a data point, in this case, a needle, that is significantly different from the other data points within its cluster. An outlier is an observation that lies an abnormal distance away from other values in a dataset. In the context of clustering, an outlier is a data point that doesn't match to the general patterns or characteristics of its assigned cluster [185], [186]. In this work, the Silhouette score function from the scikit-learn library is used to calculate the average Silhouette score for each clustered image across all of its clusters. A Silhouette score closer to 1 indicates a high-quality cluster, while scores toward -1 indicate incorrect assignment of pixels to clusters. In our dataset, I observed that the majority of Silhouette scores lie in the range of 0.52 to 0.72, illustrating a good cluster quality as shown in the boxplot in Fig. 4.15. This demonstrates that the clustering algorithm was successful and able to detect the needle boundaries in the MR images.

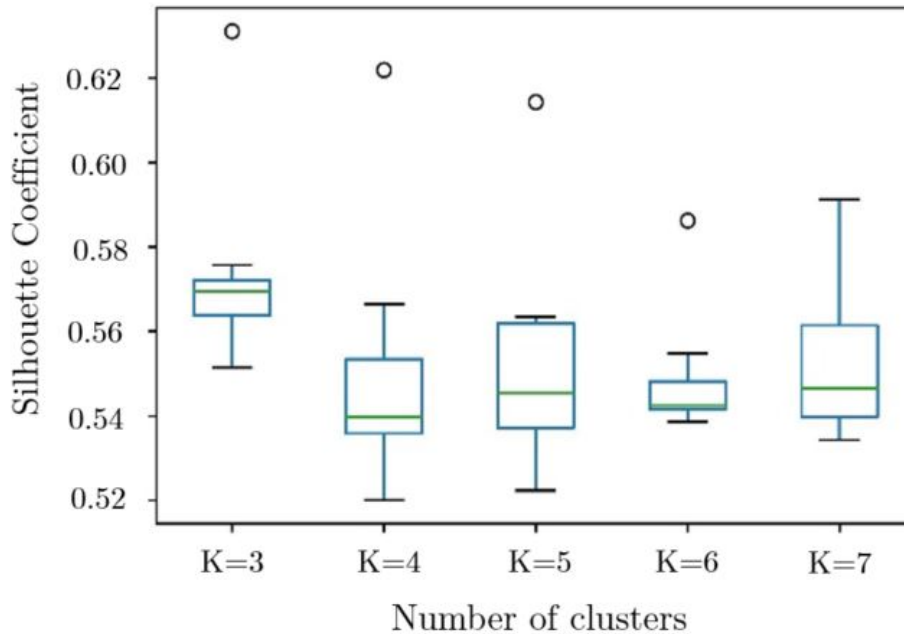


Figure 4.15: Boxplot showing the Silhouette coefficient according to K-means clusters that have been applied for the needles in the MR image. The green line represents the median of data, and the circles are the outliers.

### 4.3 Assessing mechanical properties of non-metallic biopsy needles

This section details the mechanical findings of the proposed biopsy needles, which were obtained through a comprehensive two-stage process as described earlier in Chapter 3. The process involved a combination of experimental testing and simulation utilizing

finite element analysis (FEA), The results presented herein demonstrate the mechanical performance of the biopsy needles under various loading conditions.

#### 4.3.1 Results from the experimental setup using Zwick Roell machine

The results of the mechanical bending test were presented for seven non-metallic PBNs and the NiTi needle using the Zwick Roell machine in Fig. 4.16. The reference NiTi needle exhibited significantly greater stiffness in this test compared to all of the proposed needles. Needles numbered 3 and 5 displayed notably low stiffness and showed minimal variation between each other. Conversely, needles numbered 2, 4, 6, and 7, which featured varying wall thicknesses, demonstrated higher stiffness values. Needle number 1, constructed using PEEK material as an outer sheet, displayed an enhanced supporting effect for the needle structure, achieving the highest stiffness force among the seven non-metallic needles. Although it was still less stiff than the NiTi needle. Building upon the findings from the experimental setup, additional tests were essential to improve the performance of the non-metallic needles. As a result, a finite element analysis was executed using ANSYS, and the outcomes of the simulation are detailed in the following section.

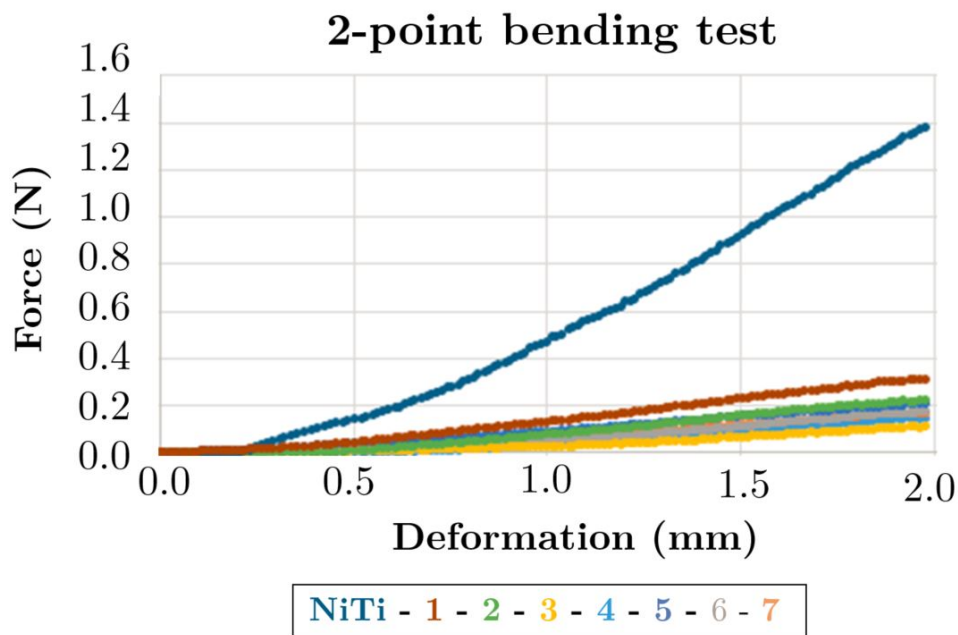


Figure 4.16: 2-point bending test results from the Zwick Roell machine for the non-metallic PBNs (1-7) and the standard biopsy needle (NiTi), representing the average of three repetitive measurements. Standard Deviation (SD) is not shown in the graph due to the sensitivity of the test measurements. The standard deviation, a measure of the variability in a set of data points, has not been displayed on the graph because the measurements taken during the test are highly sensitive and subject to slight variations that could potentially obscure the visual representation [17].

### 4.3.2 Results from the modeling using FEA

This section presents the simulation results obtained through the FEA modeling technique. The results are presented in two distinct stages. The first stage describes the outcomes of Design I, which involved the design and testing of core needles. The second stage presents the findings related to the optimal structure and design of biopsy needles in Design II.

#### *Design I*

The results for simulation by FEA for Design I introduced the following tests sequence:

#### **- Force reaction vs. displacement**

This test is utilized to conduct a 2-point bending simulation in ANSYS, employing static structural analysis. The obtained results are based on a spectrum of values assigned to the mechanical properties of the materials, as detailed in Table 3.6. This section presents and examines these results, with a specific focus on the correlation between observed deformation and applied loading. Additionally, the acquired data is compared and analyzed against a standard NiTi needle. Fig. 4.17(a) illustrates the force values in Newtons (N) in relation to the pusher displacement of 2 mm, corresponding to the minimum values of Young's modulus, Bulk modulus, and Shear modulus as extracted from Table 3.6.

The pusher displacement was initiated at 0.1 mm and incremented in 0.1 mm until reaching a maximum displacement of 2 mm. Throughout the displacement process, force reaction readings were recorded, providing data on the mechanical response of the core needle under this test. A pusher displacement of 2 mm was applied to the standard inner core (SIC) and the corresponding force required to achieve this displacement was measured, resulting in a value of 0.35 N. Simultaneously, the corresponding forces for the proposed inner cores referred to as PIC 1, PIC 2, PIC 3, and PIC 4, were found to be 0.06 N, 0.99 N, 4.79 N, and 14.37 N, respectively as presented in Fig. 4.17(a). Based on the observations, PIC 2 exhibited superior mechanical and logical performance compared to the other four core needles in Design I. Consequently, it was chosen as the optimal inner core for this experiment and found comparable to SIC. This determination arises from the force required to achieve a pusher displacement of 2 mm, which serves as a direct indicator of the mechanical efficiency and resistance of each inner core design. PIC 2's force of 0.99 N falls within a reasonable range, indicating a balance between stiffness and flexibility. This suggests that PIC 2 is able to withstand the applied force without excessive deformation, making it mechanically robust. The consistency of force-displacement behavior across the different inner core designs is an important consideration. While PIC 1 and PIC 3 show significantly lower and higher forces, respectively 0.06 N and 4.79 N, PIC 2's force of 0.99 N lies between these extremes. This suggests that PIC 2 maintains logical consistency with the expected behavior of an optimal inner core design. The force required to displace the SIC by 2 mm is measured as 0.35 N. PIC 2's force of 0.99 N is in closer proximity to the force exhibited by the SIC, indicating that it offers a balance between the desired performance



and the existing standard. This comparability ensures that PIC 2 is a suitable candidate for practical use. Notably, the measured diameter of PIC 2 was 0.49 mm, which exhibited minimal divergence from the diameter of the standard inner core, measured at 0.40 mm. This close alignment in diameter between PIC 2 and SIC is a crucial factor, indicating that PIC 2 can be seamlessly integrated into the existing framework without requiring substantial modifications. The 2-point bending test was repeated under conditions of maximum values for Young's modulus, Bulk modulus, and Shear modulus from Table 3.6, and the resulting force reactions versus pusher displacement are presented in the following Fig. 4.17(b). For a pusher displacement of 2 mm, the force reactions (N) for SIC, PIC 1, PIC 2, PIC 3, and PIC 4 were found to be 0.64 N, 0.10 N, 1.65 N, 7.99 N, and 23.96 N, respectively. Among the PIC variants, PIC 2 exhibited mechanical performance closer to that of SIC. While PIC 3 and PIC 4 displayed higher tensile strength, their diameters surpassed the acceptable range for an MRI biopsy needle, previously specified to be within 18-22 gauge (0.70 mm-1.27 mm). This made PIC 2 the optimal choice once again for this test. Hence, PIC 2, with a diameter of 0.49 mm from FG material, was selected as the final output core for Design I. PIC 2 will serve as the input for the second stage of Design II, contributing to the completion of the biopsy needle's design. To assess uncertainty using the maximum and minimum material properties, a sensitivity analysis can be conducted. This involves varying the material properties within their defined ranges (maximum and minimum values) and observing the resulting effects on the design outcomes. By performing simulations or calculations with different property combinations, the design's sensitivity to variations in material properties can be quantified. Such an analysis provides insights into how uncertainties in material properties might influence design performance, aiding in informed decisions regarding the design's robustness and reliability under varying conditions.

- **Stress vs. displacement:** The NiTi material exhibited an ultimate tensile strength of 1450 MPa when tested for the SIC, as reported in Table 3.6. The theoretical simulation requires the ultimate tensile strength to be surpassed to indicate material breakage, along with a safety factor indicator of less than 1 [187]. In Table 4.3 it was observed that the SIC had a loading of 528.17 MPa and a safety factor of 2.74 at 2 mm pusher displacement, which indicates that there is no breaking point in the material. Likewise, the best-performing PIC 2 from the force vs. displacement test exhibited an ultimate tensile strength of 2415 MPa for fiberglass (FG) material. The stress and safety factors at 2 mm pusher displacement for the best PIC were 707.45 MPa, and the safety factor was 3.41, indicating no breaking point in the material as well as stability. The interval safety factor for the maximum values of Young's modulus, Bulk modulus, and Shear modulus is presented in Table 4.4. The data show that the stress values for 2 mm pusher displacement are well below the ultimate tensile strength limit. This robustly suggests that the materials have not reached their breaking point under the current loading conditions. However,

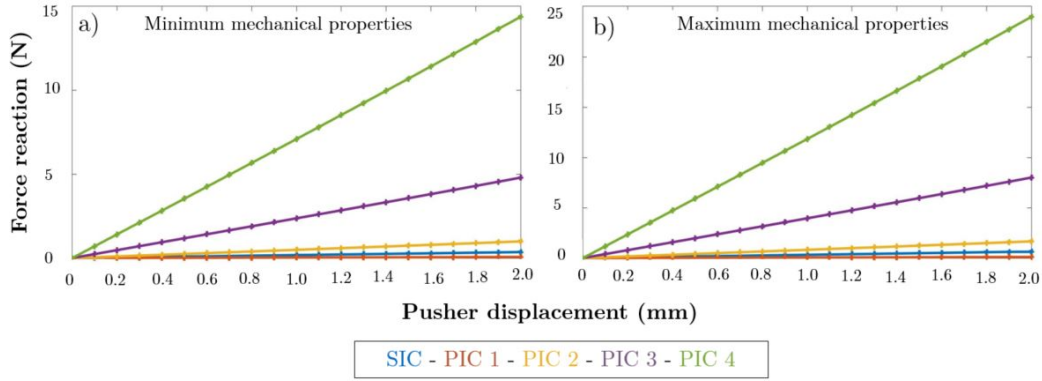


Figure 4.17: Simulation plot depicting force reactions in response to 2 mm pusher displacement for the standard inner core (SIC) and proposed inner cores (PICs): a) under conditions of minimized mechanical properties of Young's modulus, Bulk modulus, and Shear modulus for both NiTi and FG materials. Meanwhile, b) illustrating the response of core needles under conditions of maximized mechanical properties of Young's modulus, Bulk modulus, and Shear modulus for both NiTi and FG constituents.

to fully characterize the mechanical behavior of the SIC and PIC, it is recommended to increase the pusher displacement until the breaking point is reached. This will allow for a comprehensive understanding of the materials' strength and failure properties, which is crucial for ensuring their safe and reliable use in the intended application.

**- Breaking point (safety factor vs. displacement):** As outlined in Chapter 3 within the FEA part, the pusher displacement was incrementally increased up to 10 mm to identify the point of failure in the SIC and determine the optimal PIC. This assessment was conducted for mechanical properties at both the minimum and maximum ranges of mechanical properties, including Young's modulus, Bulk modulus, and Shear modulus. In this context, 10 mm displacement was applied to the SIC using the ultimate tensile strength for the range values of Young's modulus, Bulk modulus, and Shear modulus. The results of this test are shown in Table 4.5. It is observed that the stress and safety factor of the SIC indicates breaking of the material between 5.0 mm and 5.5 mm for a 10 mm pusher displacement because the value of safety facts was 0.94, less than 1. Similarly, the optimal PIC exhibits a safety factor of less than 1, signifying failure occurring at a displacement range between 6 mm and 6.5 mm. Table 4.6 presents the breaking point performance for both SIC and PIC materials at the maximum value of their Young's modulus, Bulk modulus, and Shear modulus mechanical properties. The results indicate that the breaking point occurred for the SIC when the displacement was between 2.5 mm to 3 mm. Simultaneously the PIC 2 breaking takes place displacement between 7 to 7.5 mm. Based on these findings and considering all the mechanical properties tested, it can be concluded that the PIC 2 has a higher breaking point than the SIC, as a larger pusher displacement is needed to reach failure.

Table 4.3: The stress and safety factor for the SIC and the best PIC were obtained through simulation testing of Design I. The test was conducted at a 2mm pusher displacement, using the minimum range values for Young's modulus, Bulk modulus, and shear modulus.

Time (s)	Displacement Pusher (mm)	Safety factor		Stress (MPa)	
		SIC	Best PIC 2	SIC	Best PIC 2
0.1	0.1	15	15	26.26	35.15
0.2	0.2	15	15	52.53	70.30
0.3	0.3	15	15	78.79	105.47
0.4	0.4	13.8	15	105.07	140.63
0.5	0.5	11.04	13.73	131.35	175.81
0.6	0.6	9.19	11.44	157.63	211
0.7	0.7	7.88	9.80	183.93	246.21
0.8	0.8	6.89	8.58	210.24	281.44
0.9	0.9	6.12	7.62	236.57	316.7
1.0	1.0	5.51	6.861	262.92	351.99
1.1	1.1	5.01	6.23	289.29	387.31
1.2	1.2	4.59	5.71	315.69	422.67
1.3	1.3	4.23	5.27	342.12	458.07
1.4	1.4	3.93	4.89	368.58	493.51
1.5	1.5	3.67	4.56	395.07	529.01
1.6	1.6	3.43	4.27	421.60	564.57
1.7	1.7	3.23	4.02	448.17	600.18
1.8	1.8	3.05	3.79	474.79	635.87
1.9	1.9	2.89	3.59	501.46	671.62
2.0	2.0	2.74	3.41	528.17	707.45

### *Design II*

The second stage of the FEA simulation involved presenting the mechanical characteristics of the complete biopsy needle, which includes the outer sheet and inner core. In order to obtain the necessary data, the mechanical material properties from Table 3.9 were applied.

**- Force reaction vs. displacement:** The simulation results of force versus displacement for Design II, utilizing materials with minimum mechanical properties for Young's modulus, Bulk modulus, and Shear modulus, are presented in Fig. 4.18(a) depicting the relationship between the force values, measured in Newtons (N), and the pusher displacement of 2 mm for the biopsy needles at the minimum range of Young's modulus, Bulk modulus, and Shear modulus. Similarly, Fig. 4.18(b) illustrates the force reaction behavior of the needles when the mechanical properties of Young's modulus, Bulk modulus, and Shear modulus are set to their maximum range. Based on the mechanical material properties analysis, the PBN 1 design is selected as the optimal biopsy needle. This is due to the use of a hollow outer sheet made of PEEK material with a diameter of 1.15 mm. The superior

Table 4.4: Simulation test results for the stress and safety factor for standard and best proposed inner core for 2 mm pusher displacement when the mechanical properties of the materials are at maximum range in Design I.

Time (s)	Displacement Pusher (mm)	Safety factor		Stress (MPa)	
		SIC	Best PIC	SIC	Best PIC
0.1	0.1	15	15	47.37	58.54
0.2	0.2	15	15	94.75	117.09
0.3	0.3	10.20	15	142.14	175.64
0.4	0.4	7.65	15	189.52	234.21
0.5	0.5	6.12	15	236.91	292.79
0.6	0.6	5.09	13.91	284.32	351.4
0.7	0.7	4.37	11.92	331.75	410.03
0.8	0.8	3.82	10.4	379.21	468.7
0.9	0.9	3.39	9.27	426.7	527.41
1.0	1.0	3.05	8.34	474.22	586.19
1.1	1.1	2.77	7.58	521.78	645.02
1.2	1.2	2.54	6.94	569.4	703.94
1.3	1.3	2.34	6.40	617.07	762.92
1.4	1.4	2.18	5.94	664.81	822
1.5	1.5	2.03	5.54	712.62	881.16
1.6	1.6	1.90	5.19	760.5	940.42
1.7	1.7	1.79	4.8	808.46	999.79
1.8	1.8	1.69	4.61	856.51	1059.3
1.9	1.9	1.60	4.37	904.64	1118.8
2.0	2.0	1.52	4.14	952.87	1178.6

mechanical performance of PBN 1 becomes evident when considering the biomechanical behavior under conditions of minimum material properties. The inclusion of a hollow outer sheet made of PEEK material introduces increased structural integrity and stability. This design feature enhances the needle's ability to withstand applied bending forces without experiencing detrimental deformation. Furthermore, the larger diameter 1.15 mm of the PBN 1's hollow outer sheet provides enhanced resistance to bending and buckling, particularly when compared to the SBN as shown in Fig. 4.18(b). This resistance translates to improved structural robustness and reduced vulnerability to mechanical failure, even when subjected to conditions of minimum Young's modulus, Bulk modulus, and Shear modulus. The PBN 1 design is seen as the optimal biopsy needle design, with a diameter of 1.15 mm.

- **Stress vs. displacement:** In the second phase of our design process, Design II, additional test analyses aimed at comparing and evaluating the stress and safety factors of the new PBNs in comparison to the SBN. Utilizing a 2 mm pusher displacement for the mechanical bending setup, I present the details of the simulation results at both the

Table 4.5: Breaking point simulation test in Design I for the SIC and PIC at 10 mm pusher displacement, when mechanical properties are at a minimum, rang.

Time (s)	Displacement Pusher (mm)	Safety factor		Stress (MPa)	
		SIC	Best PIC	SIC	Best PIC
0.1	0.5	11.03	13.735	131.36	175.83
0.2	1.0	5.514	6.86	262.95	352.04
0.3	1.5	3.66	4.56	395.12	529.07
0.4	2.0	2.74	3.41	528.24	707.53
0.5	2.5	2.18	2.71	662.76	887.9
0.6	3.0	1.81	2.25	799.07	1070.7
0.7	3.5	1.54	1.92	937.93	1257.4
0.8	4.0	1.34	1.66	1080.7	1448.5
0.9	4.5	1.18	1.46	1227.9	1644.3
1.0	5.0	1.05	1.30	1379.9	1845.7
1.1	5.5	0.94	1.17	1537.3	2053.7
1.2	6.0	0.85	1.06	1701.2	2269.3
1.3	6.5	0.77	0.96	1872.4	2493.9
1.4	7.0	0.70	0.88	2052.4	2729.3
1.5	7.5	0.64	0.81	2242.9	2977.5
1.6	8.0	0.59	0.74	2445.9	3241.3
1.7	8.5	0.54	0.68	2664.4	3524.1
1.8	9.0	0.49	0.63	2902	3830.5
1.9	9.5	0.45	0.57	3163.8	4166.7
2.0	10.0	0.41	0.53	3457.4	4541.5

minimum and maximum range for Young’s modulus, Bulk modulus, and Shear modulus in the Appendix, Table B.2 and Table B.3. The results conclusively demonstrate that, under a 2 mm pusher displacement for mechanical material properties, the stress values remain well within the ultimate tensile strength limit. This indicates that the material’s structural integrity remains intact, as the stress levels experienced do not surpass the maximum threshold for deformation or failure. The corresponding mechanical material properties are provided in the accompanying Table 3.9. For this reason, pusher displacement was increased to 10 mm, similar to the procedure for Design I, to find the breaking points in the standard and proposed inner cores.

Table 4.6: Breaking point simulation test for the SIC and best PIC at 10 mm pusher displacement for maximum values of material properties in Design I.

Time (s)	Displacement Pusher (mm)	Safety factor		Stress (MPa)	
		SIC	Best PIC	SIC	Best PIC
0.1	0.5	6.11	15	236.95	292.83
0.2	1.0	3.05	8.34	474.28	586.31
0.3	1.5	2.03	5.54	712.79	881.44
0.4	2.0	1.52	4.14	953.12	1179
0.5	2.5	1.21	3.30	1196	1479.6
0.6	3.0	1.00	2.74	1442	1784.4
0.7	3.5	0.85	2.33	1692.1	2094.3
0.8	4.0	0.74	2.02	1948.1	2411.2
0.9	4.5	0.65	1.78	2211.4	2736.1
1.0	5.0	0.58	1.59	2483.3	3070
1.1	5.5	0.52	1.43	2764.6	3414.5
1.2	6.0	0.47	1.29	3057	3771.6
1.3	6.5	0.43	1.18	3362.5	4143.4
1.4	7.0	0.39	1.07	3683.3	4532.8
1.5	7.5	0.36	0.98	4022.5	4943.2
1.6	8.0	0.33	0.90	4383.8	5378.9
1.7	8.5	0.30	0.83	4772.1	5845.7
1.8	9.0	0.27	0.76	5194.2	6350.9
1.9	9.5	0.25	0.70	5659.2	6904.8
2.0	10.0	0.23	0.65	6180.1	7521.4

- **Breaking point (safety factor vs. displacement):** After conducting an analysis, the pusher displacement was increased to 10 mm. The corresponding results are presented in Table 4.7, and they are cross-referenced with the minimum values of Young’s modulus, Bulk modulus, and Shear modulus found in the Table 3.9, it is evident that the safety factor falls below 1, and the stress exceeds the ultimate tensile strength for the NiTi inner core and outer sheet material used in the SBN. Specifically, when the pusher displacement is increased from 5.5 mm to 6.0 mm, the safety factor falls below 1, indicating that the SBN is highly likely to break under these loading conditions. While the performance of PBN 1 under pusher displacement revealed that the safety factor dropped below 1 when the pusher displacement was increased from 7.5 mm to 8.0 mm, indicating that the fiberglass core experienced a failure between these displacements and the stress values reached 2530.3 MPa. Subsequently, the mechanical properties of SBN were investigated, and at their peak, the material exhibited maximum values for Young’s modulus, Bulk modulus, and Shear modulus. The ultimate tensile strength of SBN was determined to be 1461.2 MPa, as illustrated in Table 4.8. However, when the pusher displacement was increased from 3.0 mm to 3.5 mm, the safety factor dropped below unity, indicating that

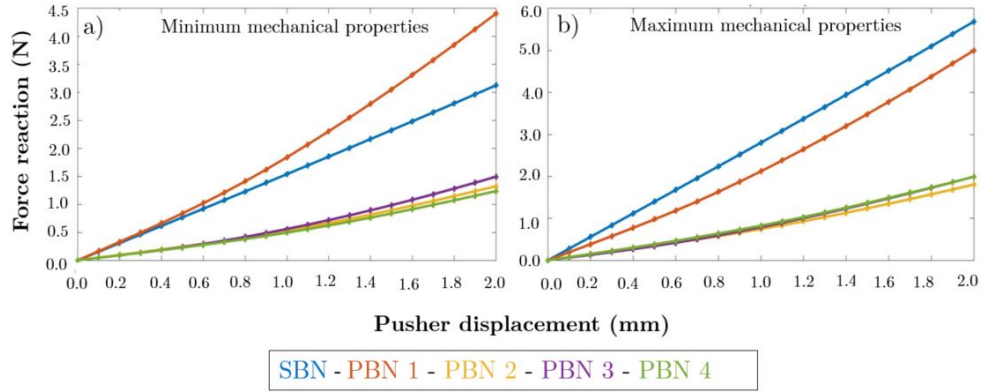


Figure 4.18: Simulation results depicting the force reaction versus pusher displacement at a 2 mm interval for both the SBN and PBNs. The analysis encompasses the minimum and maximum values of material properties of Young's modulus, Bulk modulus, and Shear modulus, as specified in Design II.

the material had failed between these displacement values. The cause of the failure was attributed to the applied stress exceeding the ultimate tensile strength of the material. In the case of PBN 1, the safety factor also dropped below unity when the pusher displacement increased from 9.0 mm to 9.5 mm, and the applied stress reached a level of 5188.1 MPa. This decrease in safety factor suggested the potential failure of the needle's inner core. This event could cause severe damage and have significant consequences.

Finally, it is important to note that the failure points for both SBN and PBN 1 were successfully identified, indicating an increased time to failure as pusher displacement increased under all the mechanical properties ranges. In comparison, SBN failed at a faster rate than PBN. These findings are significant in understanding the failure behavior of biopsy needles under varying conditions and can influence design and optimization efforts for improved structural performance. From the observations, several notable mechanical property features were achieved in PBN 1 in comparison to SBN. Firstly, PBN 1 exhibited a higher ultimate tensile strength, indicating its ability to withstand greater applied forces before reaching a point of failure. This increased strength is indicative of enhanced load-bearing capacity and structural robustness, suggesting potential improvements in biopsy needle durability. Secondly, PBN 1 demonstrated a more uniform stress distribution along its length under varying pusher displacements. This uniform stress distribution signifies a balanced load distribution and reduced localized stress concentrations, which can contribute to minimizing tissue damage during biopsy procedures. Additionally, PBN 1 exhibited a higher safety factor across different displacement ranges, highlighting its improved capacity to handle mechanical loads without compromising its integrity. These observed mechanical property features in PBN 1 underscore its potential for enhanced performance and safety in clinical applications compared to SBN. The outcome of the FEA model-generated design presented in Fig. 4.19, resulting in the proposed biopsy

Table 4.7: Simulation results for the breaking points of SBN and the top-performing PBN 1 were obtained for a 10 mm pusher displacement using the minimum values of Young's modulus, Bulk modulus, and Shear modulus.

Time (s)	Displacement Pusher (mm)	Safety factor		Stress (MPa)	
		Standard biopsy needle	Best proposed biopsy needle	Standard biopsy needle	Best proposed biopsy needle
		SBN	PBN 1	SBN	PBN 1
0.1	0.5	13.06	15	110.98	137.78
0.2	1.0	6.51	8.83	222.65	273.49
0.3	1.5	4.32	5.87	335.42	411.34
0.4	2.0	3.22	4.38	449.57	551.02
0.5	2.5	2.56	3.48	565.38	692.7
0.6	3.0	2.12	2.88	683.12	836.71
0.7	3.5	1.80	2.45	803.1	983.46
0.8	4.0	1.56	2.13	925.69	1133.4
0.9	4.5	1.37	1.87	1051.3	1287.1
1.0	5.0	1.22	1.67	1180.5	1445
1.1	5.5	1.10	1.50	1313.9	1608
1.2	6.0	0.99	1.35	1452.1	1776.6
1.3	6.5	0.90	1.23	1596	1952
1.4	7.0	0.83	1.13	1746.4	2135.1
1.5	7.5	0.76	1.03	1904.8	2327.4
1.6	8.0	0.69	0.95	2072.9	2530.3
1.7	8.5	0.64	0.87	2252.6	2745.4
1.8	9.0	0.59	0.81	2446.5	2974.9
1.9	9.5	0.54	0.74	2658.2	3222.4
2.0	10.0	0.50	0.69	2892.9	3491.4

needle PBN 1 with a diameter of 1.15 mm, holds significant importance due to its direct implications for optimizing the design of biopsy needles. By successfully tailoring the diameter to match the necessary mechanical performance of the standard biopsy needle (SBN), this achievement highlights the capability of the FEA modeling approach to guide and inform engineering solutions for medical applications. The selection of a 1.15 mm diameter for PBN 1, based on simulation-derived insights, demonstrates a rational and data-driven approach to enhancing the structural integrity and functional effectiveness of biopsy needles. This not only showcases the potential of computational tools in guiding design decisions but also underscores the feasibility of achieving improved performance while adhering to essential mechanical requirements. Therefore, this outcome provides a valuable precedent for utilizing advanced simulation techniques in the medical device design process, leading to more refined and optimized solutions that can contribute to enhanced patient care and procedural outcomes.



Table 4.8: Simulation breaking point test for the needles at 10 mm pusher displacement for maximum mechanical properties in Design II.

Time (s)	Pusher Displacement (mm)	Safety factor		Stress (MPa)	
		Standard biopsy needle	Best proposed biopsy needle	Standard biopsy needle	Best proposed biopsy needle
		SBN	PBN 1	SBN	PBN 1
0.1	0.5	7.175	15	202.09	225.53
0.2	1.0	3.57	10.91	405.5	447.83
0.3	1.5	2.37	7.26	610.87	673.16
0.4	2.0	1.77	5.42	818.58	902.22
0.5	2.5	1.40	4.30	1029.2	1134.7
0.6	3.0	1.16	3.56	1243.2	1371.1
0.7	3.5	0.99	3.03	1461.2	1611.5
0.8	4.0	0.86	2.63	1683.9	1856.6
0.9	4.5	0.75	2.32	1912.1	2107
1.0	5.0	0.67	2.06	2146.6	2363.6
1.1	5.5	0.60	1.86	2388.6	2627.3
1.2	6.0	0.54	1.68	2639.2	2899.3
1.3	6.5	0.50	1.53	2900	3180.8
1.4	7.0	0.45	1.40	3172.5	3473.2
1.5	7.5	0.76	1.29	3459.3	3778.7
1.6	8.0	0.69	1.19	3763.3	4099.8
1.7	8.5	0.64	1.10	4088.1	4439.1
1.8	9.0	0.59	1.01	4438.4	4800.6
1.9	9.5	0.54	0.94	4820.4	5188.1
2.0	10.0	0.50	0.87	5243.5	5607.1

### 4.3.3 Uncertainty analysis in FEA: Critical analysis

In this study, I aimed to assess uncertainties within ANSYS by analyzing variations in mesh element sizes. The mesh element sizes were adjusted between 7 mm and 10 mm, considering software limitations that prevent using smaller mesh sizes. As explained earlier in Chapter 3, the optimal mesh element size was identified as 6 mm through careful verification. The presented Table 4.9 at the minimum range values of Young's modulus, Bulk modulus, and shear modulus illustrates the impact of mesh element size variation on force reaction error for both the SBN and PBN with minimum Young's modulus, Bulk modulus, and Shear modulus values PBN 1. The analysis was conducted at a pusher displacement of 2 mm. It is evident from the data that the force error percentages exhibit distinct trends as the mesh element size is adjusted. Overall, the force error decreases with larger mesh element sizes for both needle types. This trend aligns with the expectations of numerical simulations, as larger mesh elements contribute to a coarser representation of the geometry, potentially leading to reduced precision in capturing intricate mechanical

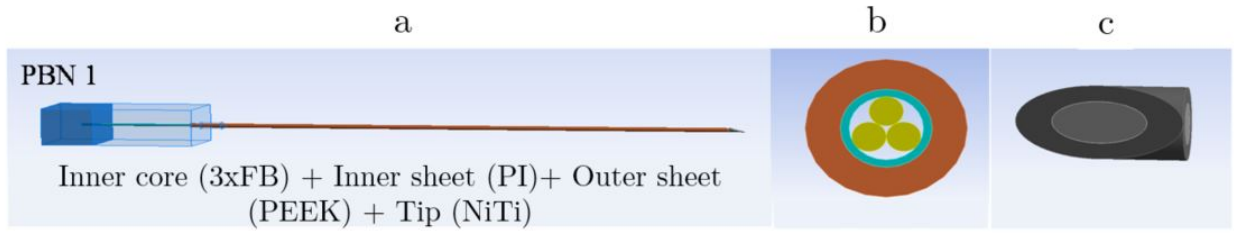


Figure 4.19: Final design of the best non-metallic proposed biopsy needle in 18.5-gauge standard. The figure includes a) materials utilized for needle fabrication, b) a cross-sectional view of the biopsy needles, c) biopsy needle Chiba tip.

interactions. For the SBN, the force error diminishes substantially as the mesh element size increases. The force error at a mesh element size of 10 mm is approximately 0.042%, down from 0.0983% at a size of 7 mm. This decrease suggests that a coarser mesh is more conducive to accurate force prediction for the standard needle. The same trend is observed for the proposed PBN 1, where the force error drops from 0.24125% at a mesh element size of 7 mm to 0.04744% at a size of 10 mm. While the data from Table 4.10 reveals distinct trends in force error percentages (%) as the mesh element size is altered. Overall, a consistent pattern emerges, whereby the force error tends to decrease with larger mesh element sizes for both needle types. This trend aligns with computational mechanics principles, where coarser meshing typically leads to reduced computational effort but may sacrifice accuracy. For the SBN, the force error demonstrates a noticeable reduction as the mesh element size increases. Specifically, the force error diminishes from 0.0756% at a mesh element size of 7 mm to 0.0479% at a size of 10 mm. Similarly, for the proposed PBN 1, the force error decreases from 0.2418% to 0.0484% over the same mesh element size range. It should be noted that mesh convergence is not solely dependent on the mesh size, but also on the element model. For instance, PBN 1 comprises multiple structures, which may have contributed to the higher error percentage observed compared to SBN. The observed reduction in force error with increasing mesh element size can be attributed to the trade-off between computational efficiency and accuracy. Coarser mesh elements result in fewer computational cells, leading to faster simulations. However, this advantage comes at the expense of spatial resolution and the ability to capture intricate mechanical behaviors accurately. The finer details of the geometry and stress distributions may be overlooked with larger mesh elements. The diminishing force error for both needle types demonstrates that a mesh element size of 10 mm provides a reasonable compromise between accuracy and computational efficiency for the given pusher displacement of 2 mm. This size offers a balance between adequately capturing mechanical interactions and maintaining a manageable computational load. It is important to note that the optimal mesh element size may vary depending on the specific application and the desired level of accuracy. Factors such as geometry complexity, material properties, and simulation objectives should be considered when selecting an appropriate mesh element size. In conclusion, this study

highlights the influence of mesh element size on force reaction error in the context of biopsy needle simulations. The presented data emphasize the importance of careful mesh sizing to achieve accurate and efficient numerical results. The observed trends underscore the need for sensitivity analyses and optimization studies to determine the most suitable mesh configuration for a given simulation scenario.

Table 4.9: Effect of mesh element size variation on force reaction error at a pusher displacement of 2 mm for SBN and best PBN 1 with minimum Young’s modulus, Bulk modulus, and Shear modulus values.

Pusher displacement (mm)	Mesh element size (mm)	Force error (%) for SBN	Force error (%) for best PBN 1
2	6	—	—
2	7	0.0984	0.24125
2	8	0.05623	0.14333
2	9	0.13214	0.16151
2	10	0.04217	0.04744

Table 4.10: Effect of mesh element size variation on force reaction error at a pusher displacement of 2 mm for SBN and best PBN 1 with maximum Young’s modulus, Bulk modulus, and Shear modulus values.

Pusher displacement (mm)	Mesh element size (mm)	Force error (%) for SBN	Force error (%) for best PBN 1
2	6	—	—
2	7	0.07575	0.24176
2	8	0.03710	0.15110
2	9	0.13295	0.15714
2	10	0.04792	0.04835

These results suggest that the choice of mesh element size has a significant impact on the accuracy of the numerical solution. Specifically, the error of the evaluated force is higher when the number of meshes is increased. Overall, our results showed that the proposed non-metallic needles successfully reduced susceptibility artifacts, which confirms our hypothesis. These findings provide valuable insights into the potential benefits of using non-metallic needles in medical procedures, especially those involving MRI scans.

## 5 Conclusions and future work

### 5.1 Conclusions

This section aims to address the research questions proposed in Chapter 1 section 1.2, which are listed in the following:

(1) Could the proposed non-metallic materials for the biopsy needle be able to reduce the artifacts during the MRI interventions? (2) Could the proposed design concept for the non-metallic biopsy needle fulfill the functionality criteria? (3) Could machine learning be a suitable approach for detecting needle artifacts? (4) Are the artifacts for the non-metallic biopsy needles different when a tissue-engineered phantom is applied during an MRI scan? (5) How does the use of Finite Element Analysis (FEA) enable the optimization of mechanical performance and facilitate the adjustment of final needle design specifications? Regarding the first research question, as explained in the introduction chapter, the biopsy needles produce massive artifacts in the MR image due to the material's interaction with the MRI field, which affects the visibility of the structures in the MR images. In this context, it becomes evident that unresolved MR image artifacts could introduce challenges and complexities for clinicians during a surgical procedure. As explained in the materials and method section, we have proposed a new approach for structuring the biopsy needle by combining non-metallic materials to investigate the reduction of MRI artifacts.

Based on the proposed methodology explained above, we investigate the effect of a new combination of non-metallic materials on the artifacts generated in MR images during intervention procedures. For this purpose, we have analyzed the biopsy needles in two types of phantoms with two MRI sequences. As a result, the behavior of the biopsy needle artifacts in MRI scans significantly differs between the non-metallic needles and standard needles, as explained in the results and discussion section. According to the obtained results, we conclude that it is possible to reduce the artifacts for biopsy needles in the MR image through non-metallic needles. The recommended needle for this work consists of an outer sheet made of polyether ether ketone (PEEK), an inner core composed of three layers of fluorinated ethylene propylene (3xFB) and polyimide sheet, and a tip made of either nickel-titanium (NiTi) or glass. Qualitative and quantitative analyses of the needle have demonstrated significant reductions in artifacts in both the width and length dimensions. Regarding the second research question, the mechanical attitude of conventional biopsy needles tends to kink during medical application. This limits the flexibility of biopsy needle efficiency during the procedures. For this reason, we proposed to study the mechanical

characteristics of the new proposed non-metallic materials. Mechanical tests were employed to evaluate the bending, stress, and breaking point for non-metallic needles and compare it with a standard needle. Based on that, two main steps were accomplished by practical bending setup and simulation in FEA. As presented in the results and discussion section, we first examined the proposed non-metallic needles in comparison with the standard needle in an experimental bending setup to evaluate the mechanical test. Then, by FEA simulation, a comprehensive analysis was done to optimize the dimensions for the biopsy needles in parallel with functionality, keeping in mind the standard needle gauge.

It is important to mention the FEA allowed for evaluating the prototyping for the biopsy needles across a range of mechanical material properties, including both minimum and maximum values of Young's modulus, bulk modulus, and shear modulus. Through modeling, four proposed biopsy needles of different materials and diameters were constructed and placed in the simulation mechanical bending test to verify mechanical performance. According to the tensile strength, the closest version to the SBN was in PBN 1 with a diameter of 1.15 mm (18.5 gauge), made of PEEK material hollow outer sheet with three fiberglass rods as inner core. It was chosen as the best-proposed biopsy needle. Further optimization was carried out to match the mechanical performance of SBN. Consequently, From the best achievement of PBN 1, the diameter for the hollow sheet was reduced to 0.95 mm (20 gauge) with a minimum range for mechanical properties. Then the hollow outer sheet diameter for the same PEEK materials was increased to 1.25 mm (18 gauge) at maximum material properties. With all simulation changes, PBN performed mechanically closer to SBN. The idea of this change was to provide a flexible range for the structure of the biopsy needle according to the medical needs, following a standard gauge. The breaking point analysis was carried out on PBN 1 and SBN 1, and it was found that PBN 1 could deflect higher than SBN 1 before breaking. As a result, we found that the proposed non-metallic concept achieved promising mechanical performance compared to the standard needle. Regarding the third research question, as explained in the materials and methods section, We have used a machine learning approach K-means algorithm for the MR images evaluation of the needle artifacts. The K-means algorithm showed remarkable results for detecting the artifacts for the width and length of each needle using the different clusters approach especially cluster  $K=7$ . This indicates that it can be used as an efficient qualitative and quantitative assessment method for MRI artifacts. In addition, it provides comprehensive clustering capabilities with non-overlapping image features. The silhouette coefficient showed the efficiency of the K-means cluster used. With respect to the fourth research question, I investigated the performance of the tissue-engineered phantom that we proposed for use in MRI scans, specifically focusing on its ability to reduce artifacts for biopsy needles that are embedded within the phantom. We conducted an evaluation of the artifacts produced by the biopsy needles and found that the use of non-metallic needles yielded promising results in terms of reducing these artifacts.

The last fifth research question, utilizing FEA proved to be a powerful and effective tool in optimizing the design of the proposed non-metallic PBNs. Through comprehensive evaluation of their mechanical behavior, FEA facilitated the enhancement of the performance PBNs. In summary, our proposed methodology is based on employing a new combination of non-metallic materials used for MRI biopsy needle fabrications. It has shown to be a promising approach for the two main requirements that need to be fulfilled by the needles: first, for the visibility of biopsy needles in the MR image without causing more significant artifacts. And second, to study and optimize the mechanical properties of the needles to be comparable to conventional needles typically used in MRI procedures. This revealed promising results for both artifact-reduced imaging of biopsy needles for more precise needle localization without kink. This allowed for a more comprehensive evaluation of the mechanical behavior of the biopsy needle as a whole, which is crucial for understanding its performance and optimizing its design. By utilizing FEA, it was possible to analyze the stress and strain distributions throughout the needle and identify any areas of potential failure, ultimately leading to the development of a more reliable and effective biopsy tool.

## **5.2 Future work**

Based on the qualitative and quantitative analysis of the results presented above, our findings suggest that the biopsy needle could be implemented in clinical practice after approval. However, further research and development in this field are needed, as our data could serve as a foundation for future investigations. It is possible to assemble an enhanced version of the best biopsy needle using the insights gained from our study. Thus, our study establishes a strong foundation that will support and guide future research and development in this specialized field. To ensure the suitability of the optimal biopsy needle for minimally invasive MRI-guided biopsies, its performance must be thoroughly assessed. This evaluation involves employing MRI scans in both 2D and 3D modes to examine the needle's behavior within this context. By analyzing the resulting images, we can identify potential artifacts that may affect MRI image quality and accuracy, stemming from the presence of the biopsy needle. Conducting this evaluation provides valuable insights into the biopsy needle's performance. If any issues or artifacts are detected that could potentially impact biopsy procedure accuracy or MRI image quality, necessary enhancements or adjustments can be implemented. This iterative process ensures the optimal functionality of the biopsy needle within the MRI environment, minimizing potential adverse effects on image quality and diagnostic accuracy. As a crucial component of evaluating the biopsy needle's performance, an insertion test is conducted using a gelatin phantom that simulates human tissue. This insertion test aims to verify the frictional forces exerted on the needle tip during tissue insertion, allowing a comparison with those of the standard biopsy needle. By replicating real biopsy conditions, this test further enables the assessment of the

interaction between the biopsy needle and the tissue. Notably, any artifacts observed in the MRI scans can be correlated with the insertion test results, thereby yielding a comprehensive understanding of the needle's behavior within a simulated human tissue environment. These integrated evaluations empower us to make informed adjustments and enhancements, ensuring the optimal functionality and precision of the biopsy needle for minimally invasive MRI-guided procedures. Once the results of this test are obtained, they can be used to approve the use of the needle in medical settings. Therefore, this investigation is an essential step toward validating the use of the best biopsy needle for minimally invasive procedures during MRI scans. The tissue-engineered phantom can be further developed into a 3D tumor model to enhance its experimental test strategies. Our findings suggest that extending the tissue-engineered tumor model to multiple layers, resulting in a thickness of several millimeters, could be a promising avenue for future research. Additionally, establishing a cell culture of tumor cells with primary cells could lead to higher complexity and more physiologically relevant tissue compositions, which could be used to investigate the effect of medical interventions in living biological test systems. This approach could provide valuable insights into the needle's performance during MRI-guided biopsies. By studying how the biopsy needle functions within a realistic tissue simulation, we gain essential information about its behavior and limitations. These insights can then be harnessed to inform the design of future biopsy needles. Understanding the factors that affect the needle's performance, such as frictional forces and interaction with tissue, enables us to refine and enhance the needle's design to optimize its functionality and precision. Consequently, this iterative process of evaluation and design refinement contributes to the continuous improvement of biopsy needle technology, ensuring safer and more effective minimally invasive MRI-guided biopsies. Therefore, the proposed future work could significantly advance the field of MRI-guided biopsies, leading to more accurate diagnoses and improved patient outcomes. FEA offers a comprehensive platform for evaluating the intricate mechanical behaviors of biopsy needles during tissue insertion can be analyzed in a virtual environment. Furthermore, FEA provides insight into dynamic phenomena like vibrations, heat distribution, and fluid dynamics that are pivotal in the context of minimally invasive biopsies. The parallel validation achieved through FEA measurements bolsters the robustness of our experimental findings while deepening our comprehension of the biomechanical details inherent in the needle-tissue interface. This strategic fusion of real-world measurements and computational simulations doesn't just help us learn more about how the needle works in different situations, it also opens up possibilities to keep improving its design over time. In essence, the strategic integration of FEA measurements stands as a promising pathway of future exploration, ready to expand the boundaries of our research, elevate precision, and drive the evolution of biopsy needle technology within minimally invasive medical procedures. Beyond the findings presented in this study, future investigations could consider exploring the potential of utilizing more

advanced machine learning algorithms, including deep learning, reinforcement learning, and unsupervised learning. These algorithms have shown promising results in enhancing the accuracy and performance of MRI image analysis and could aid in the detection of needle artifacts, improving the reliability of MRI-guided biopsies. By adopting this approach, there is potential for significant advancements in patient outcomes, ultimately improving the quality of healthcare.



## Bibliography

- [1] G. Adam, A. Bücker, C. Nolte-Ernsting, J. Tacke, and RW Günther. Interventional MR imaging: percutaneous abdominal and skeletal biopsies and drainages of the abdomen. *European Radiology*, 9(8):1471–1478, 1999.
- [2] J. Kariniemi, R. Blanco Sequeiros, R. Ojala, and O. Tervonen. MRI-guided abdominal biopsy in a 0.23-T open-configuration MRI system. *European radiology*, 15(6):1256–1262, 2005.
- [3] J. Tehranzadeh, C. Tao, and C. Browning. Percutaneous needle biopsy of the spine. *Acta Radiologica*, 48(8):860–868, 2007.
- [4] H. Elhawary, Z. Tsz Ho Tse, A. Hamed, M. Rea, B. Davies, and M. Lamperth. The case for MR-compatible robotics: a review of the state of the art. *The international journal of medical robotics and computer assisted surgery*, 4(2):105–113, 2008.
- [5] R. Lufkin, L. Teresi, and W. Hanafee. New needle for MR -guided aspiration cytology of the head and neck. *American Journal of Roentgenology*, 149(2):380–382, 1987.
- [6] J. Davis H. Demirel. Multiparametric magnetic resonance imaging: Overview of the technique, clinical applications in prostate biopsy and future directions. *Turkish Journal of Urology*, 44(2):93, 2018.
- [7] S. Lassche. MRI-guided biopsy as a tool for diagnosis and research of muscle disorders. *Journal of Neuromuscular Diseases*, 5(3):315–319, 2018.
- [8] H. Quick. MR-compatible instruments for interventional MRI. *Interventional Magnetic Resonance Imaging*, pages 35–51, 2011.
- [9] J. Genant, J. Vandevenne, A. Bergman, Ch. Beaulieu, S. Kee, A. Norbash, and Ph. Lang. Interventional musculoskeletal procedures performed by using MR imaging guidance with a vertically open MR unit: assessment of techniques and applicability. *Radiology*, 223(1):127–136, 2002.
- [10] J. Fischbach, F. Bunke, M. Thormann, G. Gaffke, K. Jungnickel, J. Smink, and J. Ricke. MR-guided freehand biopsy of liver lesions with fast continuous imaging using a 1.0-T open MRI scanner: experience in 50 patients. *Cardiovascular and interventional radiology*, 34(1):188–192, 2011.

- [11] P. Kerimaa, A. Marttila, P. Hyvönen, R. Ojala, E. Lappi-Blanco, O. Tervonen, and R. Sequeiros. MRI-guided biopsy and fine needle aspiration biopsy FNAB in the diagnosis of musculoskeletal lesions. *European Journal of Radiology*, 82(12):2328–2333, 2013.
- [12] J. Garnon, N. Ramamurthy, J. Caudrelier, G. Erceg, E. Breton, G. Tsoumakidou, P. Rao, A. Gangi, et al. MRI-guided percutaneous biopsy of mediastinal masses using a large bore magnet: technical feasibility. *Cardiovascular and interventional radiology*, 39(5):761–767, 2016.
- [13] ITP innotom company. <https://innotom.com/produkte>. (Accessed on 01/03/2022).
- [14] SOMATEX company. <https://www.somatex.com/en/biopsy/>. (Accessed on 01/03/2022).
- [15] M. Jushiddi, J. Mulvihill, D. Chovan, A. Mani, C. Shanahan, Ch. Silien, S. Tofail, and P. Tiernan. Simulation of biopsy bevel-tipped needle insertion into soft-gel. *Computers in biology and medicine*, 111:103337, 2019.
- [16] Mayo Foundation for Medical Education and Research. Biopsy: Types of biopsy procedures used to diagnose cancer. <https://www.mayoclinic.org/diseases-conditions/cancer/in-depth/biopsy/art-20043922>. (Accessed on 11/04/2021).
- [17] M. Al-Maatoq, A. Boese, H. Henke, and M. Friebe. Primary design concept for non-metallic needle for MRI guided spinal applications. In *2019 41st Annual International Conference of the IEEE Engineering in Medicine and Biology Society (EMBC)*, pages 1994–1997. IEEE, 2019.
- [18] D. Smith. Birmingham wire gauge. [https://www.engineeringtoolbox.com/BWG-wire-gage-d\\_508.html](https://www.engineeringtoolbox.com/BWG-wire-gage-d_508.html). (Accessed on 11/04/2022).
- [19] SeeDos. MRI compatible biopsy needles and breast localisation needles. [http://www.seedos.co.uk/mri\\_biopsy.htm](http://www.seedos.co.uk/mri_biopsy.htm). (Accessed on 11/04/2022).
- [20] W. Ahn, J. Bahk, Y. Lim, and Y. Kim. The effect of introducer gauge, design and bevel direction on the deflection of spinal needles. *Anaesthesia*, 57(10):1007–1011, 2002.
- [21] M. Kaiser, M. Detert, M. Rube, A. El-Tahir, O. Elle, A. Melzer, B. Schmidt, and G. Rose. Resonant marker design and fabrication techniques for device visualization during interventional magnetic resonance imaging. *Biomedical Engineering/Biomedizinische Technik*, 60(2):89–103, 2015.

- [22] X. He, M. Liu, Ch. Liu, J. Fang, Y. Xu, L. Wang, J. Xiang, R. Sequeiros, and Ch. Li. Real-time MR-guided brain biopsy using 1.0-T open MRI scanner. *European Radiology*, 29(1):85–92, 2019.
- [23] M. Liu, J. Huang, Y. Xu, X. He, L. Li, Y. Lü, Q. Liu, R. Sequeiros, and Ch. Li. MR-guided percutaneous biopsy of solitary pulmonary lesions using a 1.0-T open high-field MRI scanner with respiratory gating. *European radiology*, 27(4):1459–1466, 2017.
- [24] Y. Matsui, J. Sakurai, T. Hiraki, S. Okamoto, T. Iguchi, K. Tomita, M. Uka, H. Gohara, and S. Kanazawa. MRI-guided percutaneous needle biopsy with 1.2 T open MRI: study protocol for a prospective feasibility study (sciro-1701). *Nagoya journal of medical science*, 81(3):463, 2019.
- [25] M. Ladd, P. Erhart, J. Debatin, B. Romanowski, P. Boesiger, and G. Mckinnon. Biopsy needle susceptibility artifacts. *Magnetic resonance in medicine*, 36(4):646–651, 1996.
- [26] J. Lewin, J. Duerk, and J. Haaga. Needle localization in MR guided therapy: effect of field strength, sequence design, and magnetic field orientation. In *Proceedings of the SMR 3rd annual meeting, Nice*, volume 1155, 1995.
- [27] H. Gehl, C. Frahm, U. Melchert, and H. Weiss. Suitability of different MR-compatible needle and magnet designs for MR-guided punctures. In *Proceedings of the SMR 3rd annual meeting, Nice*, volume 1156, 1995.
- [28] G. Lenz and C. Dewey. Study of new titanium alloy needles for interventional MRI procedures. In *Proceedings of the SMR 3rd annual meeting, Nice*, volume 1159, 1995.
- [29] L. Mei, X. Long, Y. Diao, H. Yu, W. Yang, L. Standish, and B. Qiu. MRI evaluation of metal acupuncture needles. *Acupuncture in Medicine*, 31(4):404–408, 2013.
- [30] A. Krieger, I. Iordachita, S. Song, N. Cho, P. Guion, G. Fichtinger, and L. Whitcomb. Development and preliminary evaluation of an actuated MRI-compatible robotic device for MRI-guided prostate intervention. In *2010 IEEE International Conference on Robotics and Automation*, pages 1066–1073. IEEE, 2010.
- [31] Ken M., E. Kobayashi, Y. Masutani, M. Suzuki, T. Dohi, H. Iseki, and K. Takakura. Development of an MRI-compatible needle insertion manipulator for stereotactic neurosurgery. *Journal of image guided surgery*, 1(4):242–248, 1995.
- [32] S. Sengupta. Modeling of active shimming of metallic needles for interventional MRI. *Magnetic resonance in medicine*, 84(5):2858–2870, 2020.

- [33] Th. Martin, H. Wu, D. Wang, and K. Sung. Reducing needle induced image artifacts in interventional MRI while maintaining soft tissue contrast. In *Proc. Intl. Soc. Mag. Reson. Med*, volume 23, page 4157, 2015.
- [34] S. Sengupta, X. Yan, T. Hoyt, G. Drake, A. Gunderman, and Y. Chen. Minimal artifact actively shimmed metallic needles in MRI. *Magnetic resonance in medicine*, 87(1):541–550, 2022.
- [35] M. Al-Maatoq, M. Fachel, R. Rao, and Ch. Hoeschen. Artifacts’ detection for MRI non-metallic needles: Comparative analysis for artifact evaluation using k-means and manual quantification. *Magnetochemistry*, 9(3):79, 2023.
- [36] A. Laurent. Materials and biomaterials for interventional radiology. *Biomedicine & pharmacotherapy*, 52(2):76–88, 1998.
- [37] T. Penzkofer, N. Peykan, K. Schmidt, G. Krombach, and Ch. Kuhl. How MRI compatible is “MRI compatible”? a systematic comparison of artifacts caused by biopsy needles at 3.0 and 1.5 T. *Cardiovascular and interventional radiology*, 36(6):1646–1657, 2013.
- [38] S. Currie, N. Hoggard, I. Craven, M. Hadjivassiliou, and I. Wilkinson. Understanding MRI: basic MR physics for physicians. *Postgraduate medical journal*, 89(1050):209–223, 2013.
- [39] J. Ridgway. Cardiovascular magnetic resonance physics for clinicians: part i. *Journal of cardiovascular magnetic resonance*, 12(1):1–28, 2010.
- [40] C. Babiloni, V. Pizzella, C. Gratta, A. Ferretti, and G. Romani. Fundamentals of electroencefalography, magnetoencefalography, and functional magnetic resonance imaging. *International review of neurobiology*, 86:67–80, 2009.
- [41] M. Jacobs, T. Ibrahim, and R. Ouwerkerk. MR imaging: brief overview and emerging applications. *Radiographics*, 27(4):1213–1229, 2007.
- [42] Nature. The world’s strongest MRI machines are pushing human imaging to new limits. <https://www.nature.com/articles/d41586-018-07182-7>. (Accessed on 09/05/2023).
- [43] R. Kramme, K. Hoffmann, and R. Pozos. *Springer handbook of medical technology*. Springer Science & Business Media, 2011.
- [44] S. Forshult. Magnetic resonance imaging–MRI–an overview. 2007.

- [45] J. Caro, E. Trindade, and M. McGregor. The cost-effectiveness of replacing high-osmolality with low-osmolality contrast media. *AJR. American journal of roentgenology*, 159(4):869–874, 1992.
- [46] My-Ms. Basic plane mathematics of MRI. [https://my-ms.org/mri\\_planes.htm](https://my-ms.org/mri_planes.htm). (Accessed on 21/02/2022).
- [47] Planes. Basic plane mathematics of MRI. [https://my-ms.org/mri\\_planes.htm](https://my-ms.org/mri_planes.htm). (Accessed on 04/07/2022).
- [48] G. Lloyd-Jones. MRI signal production. [https://www.radiologymasterclass.co.uk/tutorials/mri/mri\\_signal](https://www.radiologymasterclass.co.uk/tutorials/mri/mri_signal). (Accessed on 29/03/2022).
- [49] H. Schild. MRI: Made easy (berlin: Schering ag). 1990.
- [50] B. Gruber, M. Froeling, T. Leiner, and D. Klomp. Rf coils: A practical guide for nonphysicists. *Journal of magnetic resonance imaging*, 48(3):590–604, 2018.
- [51] J. Cui. *Forced Current Excitation in Selectable Field of View Coils for 7T MRI and MRS*. PhD thesis, 2017.
- [52] A. Wolski. Theory of electromagnetic fields. *arXiv preprint arXiv:1111.4354*, 2011.
- [53] spins. MRI physics: Pulse sequences. <http://xrayphysics.com/sequences.html>. (Accessed on 13/05/2023).
- [54] G. Katti, S. Ara, and A. Shireen. Magnetic resonance imaging (MRI)—a review. *International journal of dental clinics*, 3(1):65–70, 2011.
- [55] S. Plein, J. Greenwood, and J. Ridgway. *Cardiovascular MR manual*. Springer, 2011.
- [56] Proton density. Proton density (pd) image characteristics. <https://mrimaster.com/characterise%20image%20pd.html>. (Accessed on 28/03/2022).
- [57] T1 v T2 images. MRI interpretation t1 v t2 images. [https://www.radiologymasterclass.co.uk/tutorials/mri/t1\\_and\\_t2\\_images](https://www.radiologymasterclass.co.uk/tutorials/mri/t1_and_t2_images). (Accessed on 28/03/2022).
- [58] M. Ivancevic, L. Geerts, W. Weadock, and Th. Chenevert. Technical principles of MR angiography methods. *Magnetic resonance imaging clinics of North America*, 17(1):1–11, 2009.
- [59] J. Morelli, V. Runge, F. Ai, U. Attenberger, L. Vu, S. Schmeets, W. Nitz, and J. Kirsch. An image-based approach to understanding the physics of MR artifacts. *Radiographics*, 31(3):849–866, 2011.

- [60] B. Dale, M. Brown, and R. Semelka. *MRI: basic principles and applications*. John Wiley & Sons, 2015.
- [61] D. Preston. Magnetic resonance imaging MRI of the brain and spine: Basics. <https://case.edu/med/neurology/NR/MRI%20Basics.htm>. (Accessed on 29/03/2022).
- [62] J. Jones. Echo time. <https://radiopaedia.org/articles/echo-time>. (Accessed on 29/03/2022).
- [63] R. Hendrick. Tr and te. <https://mriquestions.com/tr-and-te.html>. (Accessed on 29/03/2022).
- [64] J. Ridgway. The MRI environment. In *Cardiovascular MR Manual*, pages 11–15. Springer, 2015.
- [65] P. Kuchel, B. Chapman, W. Bubb, P. Hansen, C. Durrant, and M. Hertzberg. Magnetic susceptibility: Solutions, emulsions, and cells. *Concepts in Magnetic Resonance Part A: An Educational Journal*, 18(1):56–71, 2003.
- [66] F. Shellock. MR imaging of metallic implants and materials: a compilation of the literature. *American Journal of Roentgenology*, 151(4):811–814, 1988.
- [67] J. Schenck. The role of magnetic susceptibility in magnetic resonance imaging: MRI magnetic compatibility of the first and second kinds. *Medical physics*, 23(6):815–850, 1996.
- [68] B. Hargreaves, P. Worters, K. Pauly, J. Pauly, K. Koch, and G. Gold. Metal induced artifacts in MRI. *AJR. American Journal of roentgenology*, 197(3):547, 2011.
- [69] R. Blanco, R. Ojala, J. Kariniemi, J. Perälä, J. Niinimäki, and O. Tervonen. Interventional and intraoperative MRI at low field scanner—a review. *European journal of radiology*, 56(2):130–142, 2005.
- [70] Power. Relative field strength. <https://mriquestions.com/how-strong-is-30t.html>. (Accessed on 08/05/2023).
- [71] F. Shellock, T. Woods, and J. Crues III. MR labeling information for implants and devices: explanation of terminology, 2009.
- [72] T. Woods. Standards for medical devices in MRI: present and future. *Journal of Magnetic Resonance Imaging: An Official Journal of the International Society for Magnetic Resonance in Medicine*, 26(5):1186–1189, 2007.
- [73] P. Moftakhar, P. Lillaney, A. Losey, D. Cooke, A. Martin, B. Thorne, R. Arenson, M. Saeed, M. Wilson, and S. Hetts. New-generation laser-lithographed dual-axis

- magnetically assisted remote-controlled endovascular catheter for interventional MR imaging: In vitro multiplanar navigation at 1.5 T and 3 T versus x-ray fluoroscopy. *Radiology*, 277(3):842–852, 2015.
- [74] A. Eldirdiri, F. Courivaud, R. Palomar, P. Hol, and O. Elle. Catheter tip tracking for Mr-guided interventions using discrete kalman filter and mean shift localization. *International journal of computer assisted radiology and surgery*, 9(2):313–322, 2014.
- [75] H. Clogenson and J. van den Dobbelsteen. Catheters and guide wires for interventional MRI: are we there yet? *Journal of Imaging and Interventional Radiology*, 2016.
- [76] M. Grothoff, Ch. Piorkowski, Ch. Eitel, Th. Gaspar, L. Lehmkuhl, Ch. Lücke, J. Hoffmann, L. Hildebrand, S. Wedan, Th. Lloyd, et al. MR imaging-guided electrophysiological ablation studies in humans with passive catheter tracking: initial results. *Radiology*, 271(3):695–702, 2014.
- [77] W. Yao, T. Schaeffter, L. Seneviratne, and K. Althoefer. Developing a magnetic resonance-compatible catheter for cardiac catheterization. *Journal of Medical Devices*, 6(4):041002, 2012.
- [78] P. Nordbeck, W. Bauer, F. Fidler, M. Warmuth, K. Hiller, M. Nahrendorf, M. Maxfield, S. Wurtz, W. Geistert, J. Broscheit, et al. Feasibility of real-time MRI with a novel carbon catheter for interventional electrophysiologyclinical perspective. *Circulation: Arrhythmia and Electrophysiology*, 2(3):258–267, 2009.
- [79] R. Gassert, L. Dovat, O. Lamercy, Y. Ruffieux, D. Chapuis, G. Ganesh, Etienne B., and H. Bleuler. A 2-dof fMRI compatible haptic interface to investigate the neural control of arm movements. In *Proceedings 2006 IEEE International Conference on Robotics and Automation, 2006. ICRA 2006.*, pages 3825–3831. IEEE, 2006.
- [80] D. Stoianovici. Multi-imager compatible actuation principles in surgical robotics. *The International Journal of Medical Robotics and Computer Assisted Surgery*, 1(2):86–100, 2005.
- [81] J. Carey, A. Fahim, and M. Munro. Design of braided composite cardiovascular catheters based on required axial, flexural, and torsional rigidities. *Journal of Biomedical Materials Research Part B: Applied Biomaterials*, 70(1):73–81, 2004.
- [82] S. Song, N. Cho, I. Iordachita, P. Guion, G. Fichtinger, and L. Whitcomb. A study of needle image artifact localization in confirmation imaging of MRI-guided robotic prostate biopsy. In *2011 IEEE International Conference on Robotics and Automation*, pages 4834–4839. IEEE, 2011.

- [83] A. Illanes, J. Krug, H. Abadi, and M. Friebe. Distortion indicator algorithm for simple artifact assessment of passive MRI markers. In *2016 38th Annual International Conference of the IEEE Engineering in Medicine and Biology Society (EMBC)*, pages 1248–1251. IEEE, 2016.
- [84] S. Patil, O. Bieri, P. Jhooti, and K. Scheffler. Automatic slice positioning (asp) for passive real-time tracking of interventional devices using projection-reconstruction imaging with echo-dephasing (pride). *Magnetic Resonance in Medicine: An Official Journal of the International Society for Magnetic Resonance in Medicine*, 62(4):935–942, 2009.
- [85] A. Heinrich and F. Guettler. Software-based automated measurement of susceptibility artifacts on magnetic resonance images. *Search in*.
- [86] R. Kalin and M. Stanton. Current clinical issues for MRI scanning of pacemaker and defibrillator patients. *Pacing and clinical electrophysiology*, 28(4):326–328, 2005.
- [87] ASTM Standard. F2119-07. standard test method for evaluation of MR image artifacts from passive implants. *ASTM International, West Conshohocken, Pa, USA*, 2006.
- [88] Ch. Thomas, H. Wojtczyk, H. Rempp, S. Clasen, M. Horger, Ch. Von Laßberg, J. Fritz, C. Claussen, and Ph. Pereira. Carbon fibre and nitinol needles for MRI-guided interventions: first in vitro and in vivo application. *European Journal of radiology*, 79(3):353–358, 2011.
- [89] M. Al-Maatoq, J. Krug, and M. Friebe. The tip is the key-rfa needle modification using PEEK for reduced susceptibility artifact in MRI. 2015.
- [90] Th. Bartnitzek, T. Thelemann, S. Apel, and K. Suphan. Advantages and limitations of ceramic packaging technologies in harsh applications. In *International Symposium on Microelectronics*, volume 2016, pages 000581–000585. International Microelectronics Assembly and Packaging Society, 2016.
- [91] Radimed Needle Bachum, <https://radimed.de/kontakt/>, Accessed: 2019-01-5,.
- [92] P. Mueller, D. Stark, J. Simeone, S. Saini, R. Butch, R. Edelman, J. Wittenberg, and J. Ferrucci. MR-guided aspiration biopsy: needle design and clinical trials. *Radiology*, 161(3):605–609, 1986.
- [93] AngioDynamics. StarBurst Radiofrequency ablation needle, <https://www.angiodynamics.com/product/starburst-xl-semi-flex-rfa-devices/>, Accessed: 2022-07-28,.



- [94] D. Elgort, C. Hillenbrand, Sh. Zhang, E. Wong, Sh. Rafie, J. Lewin, and J. Duerk. Image-guided and-monitored renal artery stenting using only MRI. *Journal of Magnetic Resonance Imaging*, 23(5):619–627, 2006.
- [95] E. Spuentrup, A. Ruebben, T. Schaeffter, W. Manning, R. Günther, and A. Buecker. Magnetic resonance-guided coronary artery stent placement in a swine model. *Circulation*, 105(7):874–879, 2002.
- [96] A. Buecker, E. Spuentrup, Th. Schmitz-Rode, S. Kinzel, J. Pfeffer, Ch. Hohl, J. van Vaals, and R. Günther. Use of a nonmetallic guide wire for magnetic resonance-guided coronary artery catheterization. *Investigative Radiology*, 39(11):656–660, 2004.
- [97] R. Mekle, E. Hofmann, K. Scheffler, and D. Bilecen. A polymer-based MR-compatible guidewire: A study to explore new prospects for interventional peripheral magnetic resonance angiography (ipmra). *Journal of Magnetic Resonance Imaging*, 23(2):145–155, 2006.
- [98] H. Clogenson, J. Dankelman, and J. van den Dobbelsteen. Steerable guidewire for magnetic resonance-guided endovascular interventions. *Journal of Medical Devices*, 8(2):021002, 2014.
- [99] S. Kos, R. Huegli, E. Hofmann, H. Quick, H. Kuehl, S. Aker, G. Kaiser, P. Borm, A. Jacob, and D. Bilecen. Feasibility of real-time magnetic resonance-guided angioplasty and stenting of renal arteries in vitro and in swine, using a new polyetheretherketone-based magnetic resonance-compatible guidewire. *Investigative radiology*, 44(4):234–241, 2009.
- [100] S. Krueger, S. Schmitz, S. Weiss, D. Wirtz, M. Linssen, H. Schade, N. Kraemer, E. Spuentrup, G. Krombach, and A. Buecker. An MR guidewire based on micropultruded fiber-reinforced material. *Magnetic resonance in medicine*, 60(5):1190–1196, 2008.
- [101] A. Tzifa, G. Krombach, N. Krämer, S. Krüger, A. Schütte, M. von Walter, T. Schaeffter, Sh. Qureshi, Th. Krasemann, E. Rosenthal, et al. Magnetic resonance-guided cardiac interventions using magnetic resonance-compatible devicesclinical perspective. *Circulation: Cardiovascular Interventions*, 3(6):585–592, 2010.
- [102] J. Kettenbach, D. Kacher, S. Koskinen, S. Silverman, A. Nabavi, D. Gering, C. Tempny, R. Schwartz, R. Kikinis, P. Black, et al. Interventional and intraoperative magnetic resonance imaging. *Annual review of biomedical engineering*, 2(1):661–690, 2000.

- [103] G. Schaefers and A. Melzer. Devices and materials in MRI. In *Springer Handbook of Medical Technology*, pages 503–521. Springer, 2011.
- [104] Interventional Cannulas for MRI-guided minimal invasive procedures. MRI-guided, <https://innotom.com/wp-content/uploads/2017/04/Prospekt-KIM-engl.-7-2021-V-2.1E.pdf>, Accessed: 2022-07-28,.
- [105] A. White. Western medical acupuncture: a definition. *Acupuncture in Medicine*, 27(1):33–35, 2009.
- [106] M. Cruvinel and A. Andrade. Needle fracture during spinal puncture: case report. *Revista Brasileira de Anestesiologia*, 54(6):794–798, 2004.
- [107] Quincke Spinal needle. BD Quincke Spinal NRFit Needles, <https://www.bd.com/en-eu/offerings/capabilities/anaesthesia-delivery/regional-anaesthesia/nrfit-connection/quincke-spinal-nrfit-needles>, Accessed: 2022-07-27,.
- [108] F. Jolesz, P. Morrison, S. Koran, R. Kelley, S. Hushek, R. Newman, M. Fried, A. Melzer, R. Seibel, and H. Jalahej. Compatible instrumentation for intraoperative MRI: expanding resources. *Journal of Magnetic Resonance Imaging*, 8(1):8–11, 1998.
- [109] P. Stradiotti, A. Curti, G. Castellazzi, and A. Zerbi. Metal-related artifacts in instrumented spine. techniques for reducing artifacts in ct and MRI: state of the art. *European Spine Journal*, 18(1):102–108, 2009.
- [110] F. Liu, R. Kijowski, G. Fakhri, and Li Feng. Magnetic resonance parameter mapping using model-guided self-supervised deep learning. *Magnetic resonance in medicine*, 85(6):3211–3226, 2021.
- [111] D. Lee, J. Lee, J. Ko, J. Yoon, K. Ryu, and Y. Nam. Deep learning in MR image processing. *Investigative Magnetic Resonance Imaging*, 23(2):81–99, 2019.
- [112] H. Alamooti, Y. Ganji, F. Farimani, and M. Rostami. Primary design of MRI compatible needle for the purpose of soft tissue insertion. In *2010 17th Iranian Conference of Biomedical Engineering (ICBME)*, pages 1–4. IEEE, 2010.
- [113] A. Mehrtash, M. Ghafoorian, G. Pernelle, A. Ziaei, F. Heslinga, K. Tuncali, A. Fedorov, R. Kikinis, C. Tempany, W. Wells, et al. Automatic needle segmentation and localization in MRI with 3-D convolutional neural networks: application to MRI-targeted prostate biopsy. *IEEE transactions on medical imaging*, 38(4):1026–1036, 2018.

- [114] I. Fantini, L. Rittner, C. Yasuda, and R. Lotufo. Automatic detection of motion artifacts on MRI using deep cnn. In *2018 International Workshop on Pattern Recognition in Neuroimaging (PRNI)*, pages 1–4. IEEE, 2018.
- [115] W. Liao, Th. Deserno, and K. Spitzer. Evaluation of free non-diagnostic DICOM software tools. In *Medical Imaging 2008: PACS and Imaging Informatics*, volume 6919, pages 11–22. SPIE, 2008.
- [116] A. Illanes, J. W Krug, and M. Friebe. Assessing MRI susceptibility artefact through an indicator of image distortion. *Current Directions in Biomedical Engineering*, 2(1):427–431, 2016.
- [117] A. Pourtaherian. Robust needle detection and visualization for 3D ultrasound image-guided interventions. 2018.
- [118] S. Song, N. Cho, I. Iordachita, P. Guion, G. Fichtinger, A. Kaushal, K. Camphausen, and L. Whitcomb. Biopsy needle artifact localization in MRI-guided robotic transrectal prostate intervention. *IEEE transactions on biomedical engineering*, 59(7):1902–1911, 2012.
- [119] S. Dhankhar, S. Tyagi, and T. Prasad. Brain MRI segmentation using K-means algorithm. In *National Conference on Advances in Knowledge Management*, pages 1–5, 2010.
- [120] Z. Chen, H. Yu, and H. Chen. Research on K-means clustering segmentation method for MRI brain image based on selecting multi-peaks in gray histogram. *Journal of Biomedical Engineering*, 30(6):1164–1170, 2013.
- [121] S. Lee, J. Kim, K. Kim, S. Park, and W. Moon. K-means clustering approach for kinetic pattern analysis of dynamic contrast enhancement breast MRI. *APAMI 2006*, page 336, 2006.
- [122] A. Derek, A. Reiter, and M. Lediju Bell. A machine learning method to identify and remove reflection artifacts in photoacoustic channel data. In *2017 IEEE International Ultrasonics Symposium (IUS)*, pages 1–4. IEEE, 2017.
- [123] A. Eatemadi, H. Daraee, H. Karimkhanloo, M. Kouhi, N. Zarghami, A. Akbarzadeh, M. Abasi, Y. Hanifehpour, and S. Joo. Carbon nanotubes: properties, synthesis, purification, and medical applications. *Nanoscale research letters*, 9(1):1–13, 2014.
- [124] M. Ahmad, M. Wahit, M. Abdul Kadir, Kh. Dahlan, and M. Jawaid. Thermal and mechanical properties of ultrahigh molecular weight polyethylene/high-density polyethylene/polyethylene glycol blends. *Journal of Polymer Engineering*, 33(7):599–614, 2013.

- [125] M. Al-Maatoq, P. Fuentealba, M. Fachel, R. Glüge, S. Ali, and Ch. Hoeschen. Carbon nanotube-based reinforced polymers for medical applications: Improving impact strength of polymer-polymer composites. *Journal of Nanomaterials*, 2022, 2022.
- [126] P. Dadras. Stress-strain behavior in bending. *Materials Park, OH: ASM International, 2000.*, pages 109–114, 2000.
- [127] Yield. Yield strengthyield point. <https://www.nuclear-power.com/nuclear-engineering/materials-science/material-properties/strength/stress-strain-curve-stress-strain-diagram/yield-strength-yield-point/>. (Accessed on 01/06/2023).
- [128] J. Yoon, J. Kim, J. Jung, D. Lee, H. Jeong, M. Shahbaz, S. Lee, and H. Kim. Obtaining reliable true plastic stress-strain curves in a wide range of strains using digital image correlation in tensile testing. *Korean J Met Mater*, 54:231–236, 2016.
- [129] S. Panyukov. Theory of flexible polymer networks: Elasticity and heterogeneities. *Polymers*, 12(4):767, 2020.
- [130] J. Jachowicz and R. McMullen. Mechanical analysis of elasticity and flexibility of virgin and polymer-treated hair fiber assemblies. *Journal of cosmetic science*, 53(6):345–361, 2002.
- [131] G. Srinivas, H. Gupta, A. Pininti, A. Tewari, and D. Gupta. Highly elastic polymer substrates with tunable mechanical properties for stretchable electronic applications. *RSC advances*, 6(109):107793–107799, 2016.
- [132] R. Chulist, L. Straka, H. Seiner, A. Sozinov, N. Schell, and T. Tokarski. Branching of 110 twin boundaries in five-layered Ni-Mn-Ga bent single crystals. *Materials & Design*, 171:107703, 2019.
- [133] Test Resources. Bend test introduction. <https://www.testresources.net/applications/test-types/bend-test/>. (Accessed on 11/04/2021).
- [134] M. Scutaru, C. Itu, M. Marin, and H. Grif. Bending tests used to determine the mechanical properties of the components of a composite sandwich used in civil engineering. *Procedia Manufacturing*, 32:259–267, 2019.
- [135] Z. Yang. *Finite element analysis for biomedical engineering applications*. CRC Press, 2019.
- [136] A. Madison. *Contributions to biomechanical finite element analysis for 3D medical images with open-source software*. PhD thesis, University of Georgia, 2013.

- [137] M. Schill. Biomechanical soft tissue modeling-techniques, implementation and application. 2001.
- [138] S. Parashar and J. Sharma. A review on application of finite element modelling in bone biomechanics. *Perspectives in Science*, 8:696–698, 2016.
- [139] J. Wall. *Simulation-driven design of complex mechanical and mechatronic systems*. PhD thesis, Blekinge Institute of Technology, 2007.
- [140] M. Terzano, D. Dini, F. Baena, A. Spagnoli, and M. Oldfield. An adaptive finite element model for steerable needles. *Biomechanics and Modeling in Mechanobiology*, 19(5):1809–1825, 2020.
- [141] R. Král and J. Náprstek. Theoretical background and implementation of the finite element method for multi-dimensional fokker–planck equation analysis. *Advances in Engineering Software*, 113:54–75, 2017.
- [142] Theoretical Manual Straus. Theoretical background for straus7 finite element analysis systems, g+ d computing, 2004.
- [143] G. Schaefers. Testing MR safety and compatibility. *IEEE Engineering in medicine and biology magazine*, 27(3):23–27, 2008.
- [144] Needles. Iso 7864:2016 sterile hypodermic needles for single use — requirements and test methods. <https://www.iso.org/standard/60481.html>. (Accessed on 14/04/2022).
- [145] M. Al-Maatoq, A. Boese, and M. Friebe. Concept of a multi-layer biopsy needle for magnetic resonance imaging interventions. *Book of abstracts 51st annual conference of the German Society for Biomedical Engineering*, 62:S349–S355, 2017.
- [146] M. Al-Maatoq, A. Boese, and M. Friebe. Flexible polymeric puncture needle for a nonlinear intervention path. *International Journal of Computer Assisted Radiology and Surgery*, 13:198–199, 2018.
- [147] A. Morozov, N. Kalinin, A. Androsov, A. Gazimiev, Y. Lerner, J. Rivas, B. Somani, D. Enikeev, and M. Gazimiev. A novel and less traumatic needle for kidney puncture: development and preclinical study results. *Journal of Endourology*, 37(1):93–98, 2023.
- [148] A. Farrer, H. Odéen, J. de Bever, B. Coats, D. Parker, A. Payne, and D. Christensen. Characterization and evaluation of tissue-mimicking gelatin phantoms for use with mrgfus. *Journal of therapeutic ultrasound*, 3(1):1–11, 2015.

- [149] Ch. Damianou et al. The role of phantoms in magnetic resonance imaging-guided focused ultrasound surgery. *Digital Medicine*, 5(2):52, 2019.
- [150] L. McGarry, C. and Grattan, A. Ivory, F. Leek, G. Liney, Y. Liu, P. Miloro, R. Rai, A. Robinson, A. Shih, et al. Tissue mimicking materials for imaging and therapy phantoms: a review. *Physics in Medicine & Biology*, 2020.
- [151] J. Cook, R. Bouchard, and S. Emelianov. Tissue-mimicking phantoms for photoacoustic and ultrasonic imaging. *Biomedical optics express*, 2(11):3193–3206, 2011.
- [152] K. Wang, Ch. Ho, Ch. Zhang, and B. Wang. A review on the 3D printing of functional structures for medical phantoms and regenerated tissue and organ applications. *Engineering*, 3(5):653–662, 2017.
- [153] N. Stein, Th. Saathoff, S. Antoni, and A. Schlaefer. Creating 3D gelatin phantoms for experimental evaluation in biomedicine. *Current Directions in Biomedical Engineering*, 1(1):331–334, 2015.
- [154] S. Nietzer, F. Baur, S. Sieber, J. Hansmann, Th. Schwarz, C. Stoffer, H. Häfner, Martin G., A. Waaga-Gasser, H. Walles, et al. Mimicking metastases including tumor stroma: a new technique to generate a three-dimensional colorectal cancer model based on a biological decellularized intestinal scaffold. *Tissue Engineering Part C: Methods*, 22(7):621–635, 2016.
- [155] Skyra. Magnetom skyra spitzenleistung mit 3T. <https://www.siemens-healthineers.com/de/magnetic-resonance-imaging/3t-mri-scanner/magnetom-skyra>. (Accessed on 22/02/2022).
- [156] D. Saloner An introduction to MR angiography. 2D vs 3D MRI. <https://mriquestions.com/2d-vs-3d-mra.html>. (Accessed on 01/09/2022).
- [157] E. Küçükkulahli, P. Erdoğmuş, and K. Polat. Brain MRI segmentation based on different clustering algorithms. *International Journal of Computer Applications*, 155(3):37–40, 2016.
- [158] I. Davidson. Understanding k-means non-hierarchical clustering. *Computer Science Department of State University of New York (SUNY), Albany*, 2002.
- [159] K-means. <https://towardsdatascience.com/understanding-k-means-clustering-in-machi>. (Accessed on 26/02/2022).
- [160] N. Calthorpe. The history of spinal needles: getting to the point. *Anaesthesia*, 59(12):1231–1241, 2004.

- [161] Bending test. <https://www.iso.org/obp/ui/#iso:std:iso:9626:ed-2:v1:en>. (Accessed on 28/02/2022).
- [162] T. Sathishkumar, S. Satheeshkumar, and J. Naveen. Glass fiber-reinforced polymer composites—a review. *Journal of reinforced plastics and composites*, 33(13):1258–1275, 2014.
- [163] Matweb. Density and poisson’s ratio of nitinol material (datasheet). [http://www.matweb.com/search/datasheet\\_print.aspx?matguid=de9dd08433714f698d513766dccea437](http://www.matweb.com/search/datasheet_print.aspx?matguid=de9dd08433714f698d513766dccea437). (Accessed on 10/04/2021).
- [164] Matweb. Ultimate tensile strength of nitinol material (datasheet). <http://www.matweb.com/search/datasheet.aspx?MatGUID=7bf10705e0494dfbbc07626e82729b04>. (Accessed on 11/04/2021).
- [165] Confluent medical. Young’s modulus and density of nitinol material (datasheet). <https://confluentmedical.com/wp-content/uploads/2016/01/Material-Data-Sheet-Superelastic.pdf>. (Accessed on 10/04/2021).
- [166] I. Aliseda. Material properties of structural steel (datasheet). <https://ab-div-op-iso-rfqcb.web.cern.ch/Drawings/Reports/Cover/English/Cover.htm>, 2003. (Accessed on 11/04/2021).
- [167] O. Zienkiewicz, R. Taylor, and J. Zhu. *The finite element method: its basis and fundamentals*. Elsevier, 2005.
- [168] A. Velling. Ultimate tensile strength. <https://fractory.com/ultimate-tensile-strength/>, 2020. (Accessed on 10/04/2021).
- [169] K. Sri Vidhya. Fatigue life, fatigue damage, fatigue factor of safety, fatigue sensitivity, biaxiality indication and equivalent stress of a radial connecting rod. *International Research Journal of Engineering and Technology (IRJET)*, 2020.
- [170] Ansys Learning Forum. Safety factor in ansys. <https://forum.ansys.com/discussion/10218/what-does-the-difference-between-safety-factor>, 2019. (Accessed on 11/04/2021).
- [171] Mechead. Fatigue analysis using safety factor. <https://www.mechead.com/ansys-workbench-fatigue-module/>, 2020. (Accessed on 11/04/2021).
- [172] J. Fischer. Structural response analysis of a composite multirotor airframe. Master’s thesis, University of Stavanger, Norway, 2019.

- [173] H. Patil and P. Jeyakarthyayan. Mesh convergence study and estimation of discretization error of hub in clutch disc with integration of ansys. In *IOP Conference Series: Materials Science and Engineering*, volume 402, page 012065. IOP Publishing, 2018.
- [174] Y. Liu and Gary G. Effects of mesh density on finite element analysis 2013-01-1375. 2013.
- [175] A. Dutt. Effect of mesh size on finite element analysis of beam. *International Journal of Mechanical Engineering*, 2(12):8–10, 2015.
- [176] Azom materials. Peek material properties (datasheet). <https://www.azom.com/properties.aspx?ArticleID=1882>. (Accessed on 11/04/2021).
- [177] Mit.edu. Polyimide material properties (datasheet). <https://www.mit.edu/~6.777/matprops/polyimide.htm>. (Accessed on 11/04/2021).
- [178] Matweb. Fep young’s modulus (datasheet). <http://www.matweb.com/search/datasheet.aspx?matguid=c782af4519d949349d7c771ff6953314&n=1>. (Accessed on 11/04/2021).
- [179] Matweb. Ptfе poisson’s ratio (datasheet). [http://www.matweb.com/search/datasheet\\_print.aspx?matguid=4e0b2e88eeba4aaeb18e8820f1444cdb](http://www.matweb.com/search/datasheet_print.aspx?matguid=4e0b2e88eeba4aaeb18e8820f1444cdb). (Accessed on 11/04/2021).
- [180] Matweb. Fep poisson’s ratio (datasheet). [http://www.matweb.com/search/datasheet\\_print.aspx?matguid=3dbaaa8dbb114c57996acd6738a7efc1&n=1](http://www.matweb.com/search/datasheet_print.aspx?matguid=3dbaaa8dbb114c57996acd6738a7efc1&n=1). (Accessed on 11/04/2021).
- [181] Dielectric Manufacturing. Ptfе young’s modulus (datasheet). <https://dielectricmfg.com/knowledge-base/teflon/>, 2020. (Accessed on 11/04/2021).
- [182] A. Dutt. Effect of mesh size on finite element analysis of beam. *International Journal of Mechanical Engineering*, 2(12):8–10, 2015.
- [183] Y. Liu and Gary Glass. Effects of mesh density on finite element analysis. Technical report, SAE Technical Paper, 2013.
- [184] K. Krupa and M. Bekiesińska-Figatowska. Artifacts in magnetic resonance imaging. *Polish journal of radiology*, 80:93, 2015.
- [185] F. Wang, H. Franco-Penya, J. Kelleher, J. Pugh, and R. Ross. An analysis of the application of simplified silhouette to the evaluation of k-means clustering validity. In *International Conference on Machine Learning and Data Mining in Pattern Recognition*, pages 291–305. Springer, 2017.



- [186] A. Mamat, F. Mohamed, M. Mohamed, N. Rawi, and M. Awang. Silhouette index for determining optimal k-means clustering on images in different color models. *Int. J. Eng. Technol*, 7(2):105–109, 2018.
- [187] M . Vidhya and K. Christina. Fatigue life, fatigue damage, fatigue factor of safety, fatigue sensitivity, biaxiality indication and equivalent stress of a radial connecting rod. *International Research Journal of Engineering and Technology*, 7(9):1499–1502, 2020.

## A Appendix

### A.1 Testing the flexibility of polymeric needles in angular setup

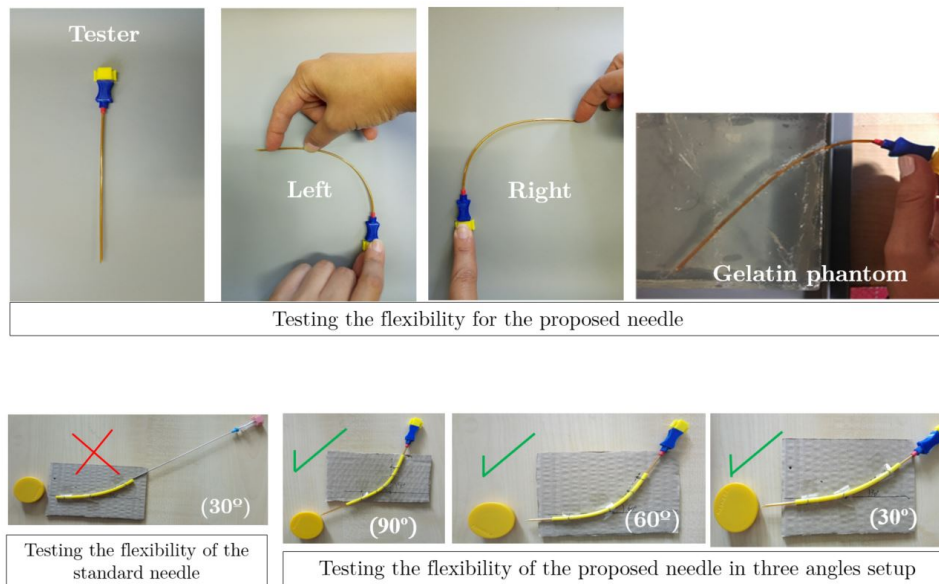


Figure A.1: Evaluate the flexibility of multi-layer polymeric biopsy needles and compare them with a standard needle in three angular setups (30°, 60°, 90°).

### A.2 MRI scanning of 2 biopsy needles in 4 rotation angle

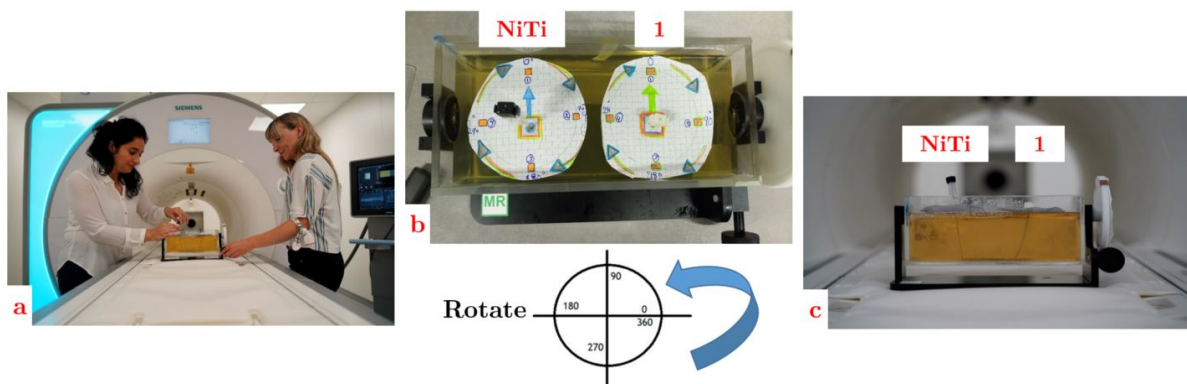


Figure A.2: MRI scan for rotational biopsy needles setup: a) fix two needles in gelatin phantom, b) apply two angle indicators for each needle, c) NiTi needle and non-metallic needle numbered as 1 inside the MRI scan.

### A.3 Measuring the dimensions for the experimental setup of the Zwick Roell machine

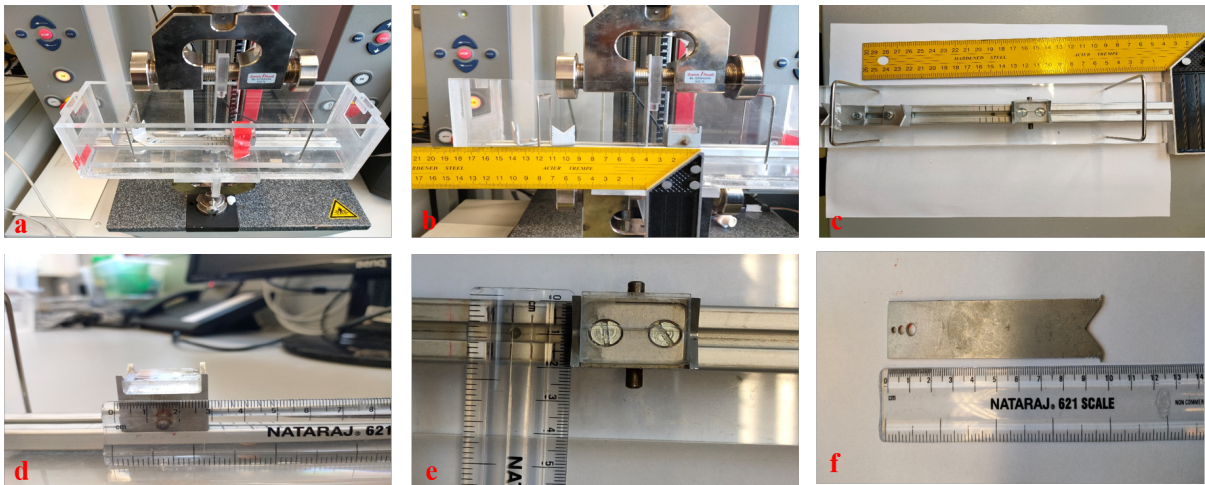


Figure A.3: Experimental setup parts for the 2-point bending test for the Zwick Roell machine.

## B Simulation FEA

### B.1 Design II: materials assignment for PBNs

Table B.1: Materials assignment in the mechanical setup for proposed biopsy needles

Components	Proposed Biopsy Needles			
	PBN 1	PBN 2	PBN 3	PBN 4
Inner core needle	FG	FG	FG	FG
Inner core holder	SS	SS	SS	SS
Inner core tip	NiTi	NiTi	NiTi	NiTi
Fixation	SS	SS	SS	SS
Pusher	SS	SS	SS	SS
Hollow inner sheet needle	PI	PI	PI	PI
Hollow outer sheet needle	PEEK	PTFE	PTFE	FEP
Outer sheet holder	SS	SS	SS	SS
Hollow outer sheet tip	NiTi	NiTi	NiTi	NiTi

## B.2 Setting the analysis parameters for Design I and Design II

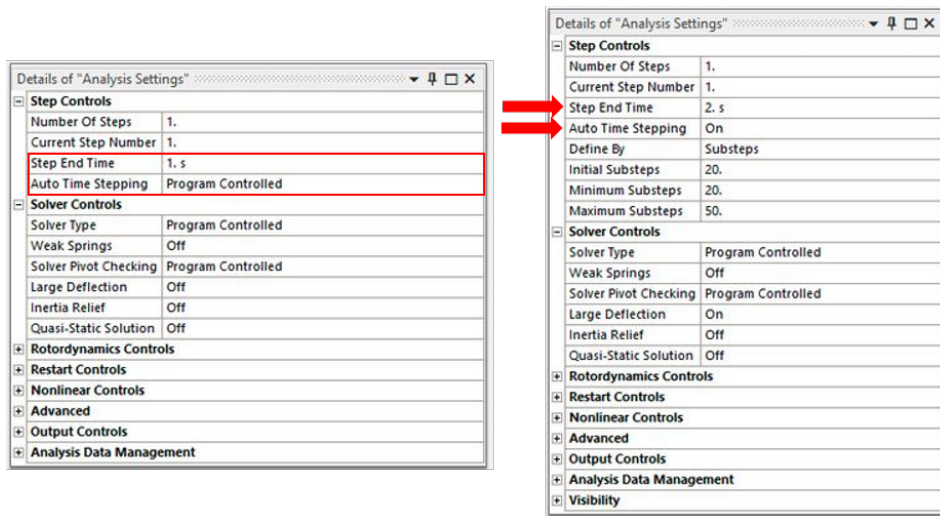


Figure B.1: Default analysis settings parameters for FEA simulation.

### B.3 Static structural analysis in FEA for Design II

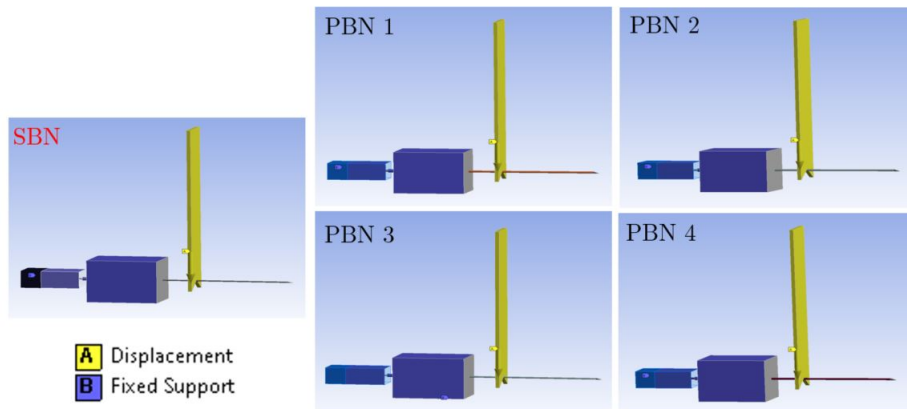


Figure B.2: Static structural analysis in FEA for Design II presents the biopsy needle's fixed support (13 faces) and displacement (7 faces).

## B.4 Bending status in FEA for the non-metallic and standard needles

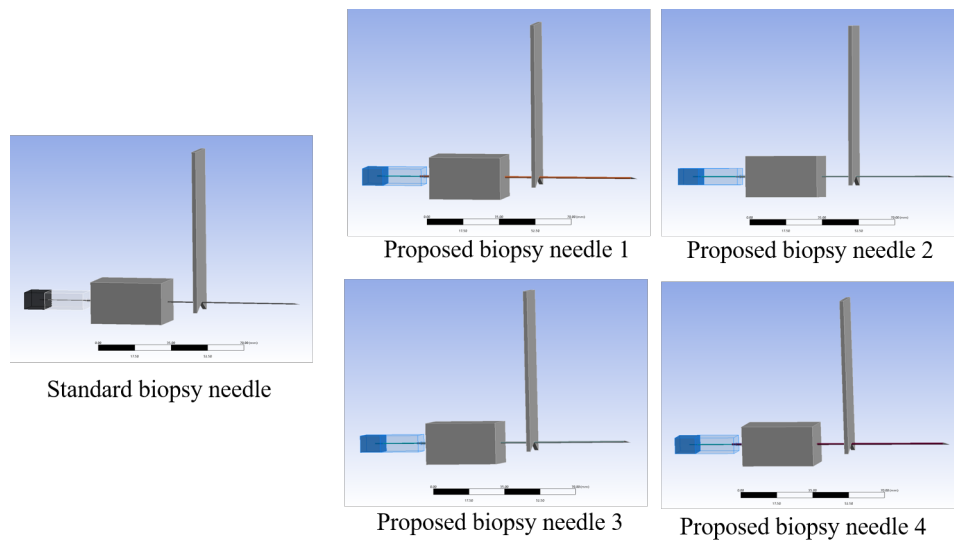


Figure B.3: Mechanical bending setups in FEA for the standard biopsy needle and proposed needles.

## B.5 Applying the meshing step for the Design II

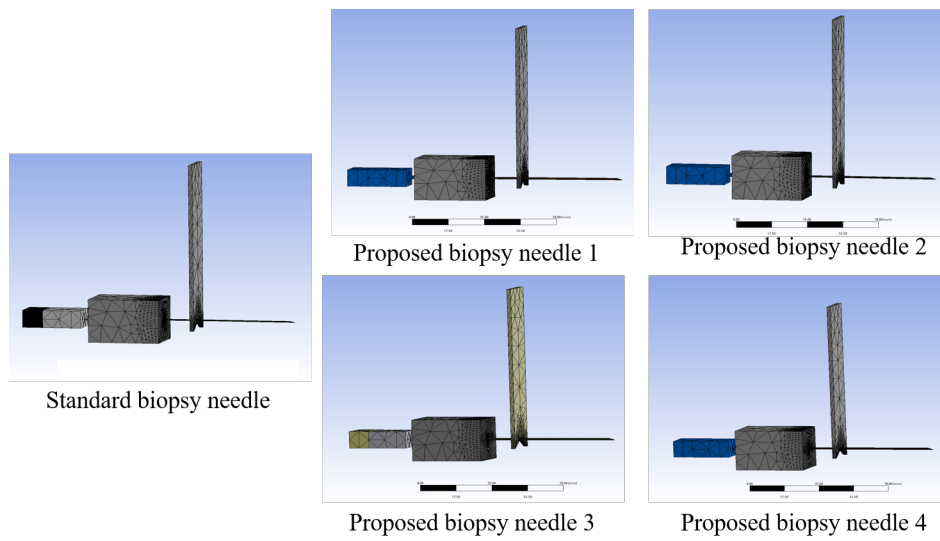


Figure B.4: Meshing for the standard biopsy needle and proposed needles.



## B.6 Stress and safety factor for standard and best-proposed biopsy needle with 2 mm

Table B.2: Stress and safety factor for standard and best-proposed biopsy needle with 2 mm pusher displacement at minimum material properties values in Design II.

Time (s)	Displacement Pusher (mm)	Safety factor		Stress (MPa)	
		SBN	Best	SBN	Best PBN
		SBN	PBN 1	SBN	PBN 1
0.1	0.1	15	15	22.15	27.73
0.2	0.2	15	15	44.33	55.47
0.3	0.3	15	15	66.52	83.24
0.4	0.4	15	15	88.73	111.11
0.5	0.5	13.06	15	110.96	138.95
0.6	0.6	10.88	14.48	133.21	166.71
0.7	0.7	9.32	12.41	155.48	194.47
0.8	0.8	8.15	10.86	177.79	222.25
0.9	0.9	7.24	9.65	200.15	250.06
1.0	1.0	6.51	8.68	222.55	277.92
1.1	1.1	5.91	7.89	245.01	305.81
1.2	1.2	5.42	7.23	267.52	333.73
1.3	1.3	4.99	6.67	290.08	361.66
1.4	1.4	4.63	6.19	312.69	389.6
1.5	1.5	4.32	5.78	335.36	417.56
1.6	1.6	4.04	5.42	358.09	445.54
1.7	1.7	3.80	5.09	380.88	473.57
1.8	1.8	3.59	4.81	403.73	501.61
1.9	1.9	3.39	4.55	426.64	529.68
2.0	2.0	3.22	4.32	449.61	557.79

**B.7 Simulation test results in Design II for the stress and safety factor for the needles at 2 mm pusher displacement for maximum mechanical properties**

Table B.3: Simulation test results in Design II for the stress and safety factor for the needles at 2 mm pusher displacement for maximum mechanical properties.

Time (s)	Pusher Displacement (mm)	Safety factor		Stress (MPa)	
		Standard biopsy needle	Best proposed biopsy needle	Standard biopsy needle	Best proposed biopsy needle
		SBN	PBN 1	SBN	PBN 1
0.1	0.1	15	15	40.35	45.51
0.2	0.2	15	15	80.74	91.04
0.3	0.3	11.96	15	121.15	136.6
0.4	0.4	8.97	15	161.59	182.18
0.5	0.5	7.17	15	202.07	227.65
0.6	0.6	5.97	15	242.58	272.96
0.7	0.7	5.12	14.61	283.14	318.22
0.8	0.8	4.47	12.74	323.76	363.5
0.9	0.9	3.97	11.28	364.46	408.93
1.0	1.0	3.57	10.12	405.24	454.5
1.1	1.1	3.25	9.16	446.11	500.14
1.2	1.2	2.97	8.37	487.06	545.81
1.3	1.3	2.74	7.70	528.11	591.55
1.4	1.4	2.54	7.13	569.25	637.33
1.5	1.5	2.37	6.63	610.5	683.15
1.6	1.6	2.22	6.202	651.84	729.02
1.7	1.7	2.09	5.82	693.28	774.93
1.8	1.8	1.97	5.48	734.84	820.89
1.9	1.9	1.86	5.18	776.5	866.93
2.0	2.0	1.77	4.90	818.27	913.05